

Adsorption of Iron and Copper with Crab Biochar

A Thesis Submitted to the School of Graduate Studies in partial fulfillment of the requirements
of the degree of

Master of Engineering, Process Engineering

Faculty of Engineering & Applied Science

Memorial University of Newfoundland

by Shantelle Mercer

February 14, 2023

Abstract

The growing human population causes increasing environmental issues from seafood waste. Biochar production through pyrolysis can reduce waste and provide a neutralizing adsorbent to treat acid mine drainage. This study aimed to determine if slow versus fast pyrolysis alters the char's characteristics and if adding iron to copper containing solution affects copper's adsorption rate. Snow crab (*Chionoecetes Opilio*) underwent slow pyrolysis at 500°C producing a porous char with a 55 wt% yield, a specific surface area of 14.73m²/g, and an average pore size of 21.5nm. Elemental analysis indicated a carbon content of 22.69 wt%, 1.24 wt% hydrogen, and 2.72 wt% nitrogen in the char, while proximate analysis determined 12 wt% volatiles, 57 wt% ash, and approximately 27 wt% calcium carbonate. XRD suggested amorphous calcium carbonate and calcite. Slow pyrolysis char contained 1.8 times more volatiles than fast pyrolysis. Batch adsorption experiments included a dosage of 5g/L with iron (II) sulphate and copper (II) sulphate as separate solutions and as mixtures with initial concentrations ranging from 25 to 150mg/L. Copper and iron had 100% removal from separate and mixed solutions. The char's alkalinity resulted in a pH of 8 and the precipitation of iron hydroxides, reducing iron's adsorption capacity to 18.4mg/g, while copper was 20mg/g. Separately, iron and copper reached equilibrium within 0.5hr and 2.0hr, respectively. As a mixture, copper's adsorption rate increased, reaching equilibrium within 0.5h until iron reached 150mg/L due to the solubility limit of Fe(OH)₂. The Pseudo Second-Order Model fitted the adsorption of the metal mixtures, and XPS suggested that metals bind directly to oxygen-bearing groups and hydroxide groups on the char's surface.

Co-Authorship Statement

The primary author of this thesis is Shantelle Mercer, and all chapters were reviewed and edited by the co-authors Dr. Kelly Hawboldt and Dr. Stephanie MacQuarrie. Shantelle Mercer conducted all adsorption experiments with technical guidance from Dr. Hawboldt and Dr. MacQuarrie.

Acknowledgments

Completing my master's during the Covid pandemic as a solo parent would not have been possible without the support and funding, I received from my supervisors Dr. Kelly Hawboldt and Dr. Stephanie MacQuarrie. In addition, I am very grateful for the motivational support from CBU's Dr. Katherine Jones, Judy MacInnis, Loree D'Orsay, and Chantelle Cormier. Many thanks also go out to David Hopkins for answering my many questions about his work. Finally, during my research, I am also truly thankful for the maintenance and troubleshooting completed by Judy MacInnis and Dr. Raj Kalia with the Flame Atomic Adsorption Spectrophotometer.

Lastly, I would like to thank my children, Penny, and Holly, for their love and patience with mommy while she spent so much time on her computer over the past two years.

Table of Contents

Abstract	ii
Co-Authorship Statement.....	iii
Acknowledgments.....	iii
List of Tables	vii
List of Figures	viii
Abbreviations.....	x
Chapter 1: Introduction and Overview.....	1
1.1 Scope and Objectives	4
1.2 Thesis Organization.....	5
Chapter 2: Literature Review	6
2.1 Introduction	6
2.2 Crustacean Feedstocks	9
2.3 Biochar Characteristics	12
2.4 Crustacean Biochar Adsorption Studies.....	19
2.5 Oxidation and Hydrolysis of Metals	32
Chapter 3: Materials and Methodology.....	34
3.1 Biochar Production.....	34
3.2 Thermal Gravimetric Analysis (TGA)	34
3.3 Surface Morphology.....	35
3.4 Brunauer-Emmett-Teller (BET) Surface Analysis.....	35
3.5 Elemental Analysis.....	35
3.6 Fourier-Transform Infrared Spectroscopy (FTIR)	36
3.7 Solid State Nuclear Magnetic Resonance (NMR).....	36
3.8 Zeta Potential Analysis	36
3.9 X-Ray powder Diffraction (XRD)	36
3.10 Batch Adsorption Experiments	37
3.11 Dosage Experiments.....	38
3.12 pH Experiments.....	38
3.13 Temperature Experiments	39
3.14 The Effect of Initial Concentration	39

3.15 Adsorption Kinetics.....	40
3.16 Char Wash.....	41
3.17 Percent (%) Difference.....	41
3.18 X-ray Photoelectron Spectroscopy (XPS).....	42
3.19 Iron Precipitation.....	42
Chapter 4: Results and Discussion.....	43
4.1 Slow and Fast Pyrolysis Crab Char.....	43
4.1.1 Thermal Gravimetric Analysis (TGA)	43
4.1.2 Surface Morphology	47
4.1.3 Surface Area	49
4.1.4 Elemental Analysis.....	50
4.1.5 Fourier-Transform Infrared Spectroscopy	52
4.1.6 Solid-State Nuclear Magnetic Resonance (NMR).....	55
4.1.7 Zeta Potential Analysis.....	57
4.1.8 X-Ray powder Diffraction (XRD).....	59
4.2 Removal of Iron and Copper from Solution using Fast Pyrolysis Crab Biochar	61
4.2.1 Iron Pourbaix (Eh-pH) Diagrams	62
4.2.2 Initial Concentrations	63
4.2.3 Iron as a Single Metal.....	64
The Effect of Dosage	64
The Effect of Initial Fe (II) Concentration	65
The Effect of Initial pH.....	67
The Effect of Temperature.....	69
4.2.4 Copper as a Single Metal.....	71
4.2.5 Adsorption Kinetics.....	73
Iron as a Single Metal	73
Single Metal Comparison	76
4.2.6 Copper and Iron Mixtures.....	78
The Effect of Dosage	78
The Effect of Initial pH.....	82
The Effect of Temperature.....	84
Adsorption Kinetics	85

4.2.7 Adsorption Kinetic Models for Copper	88
4.2.8 Post-Adsorption Analysis	96
X-ray Photoelectron Spectroscopy (XPS)	96
X-ray Diffraction (XRD)	104
Fourier Transform Infrared Spectroscopy (FTIR)	105
Surface Area.....	106
Transmission Electron Microscope (TEM)	107
4.2.9 Adsorption Mechanism.....	109
Chapter 5: Conclusions and Recommendations.....	111
5.1 Conclusions	111
5.2 Future Research.....	114
References.....	116
Appendix.....	126

List of Tables

Table 2.2 Comparing Crustacean Biochar from Fast (FP) and Slow Pyrolysis (SP)	17
Table 2.3 Crab Biochar Studies	19
Table 2.4 Crayfish Biochar Studies	24
Table 2.5 Shrimp Biochar Studies	27
Table 2.6 Metal Adsorption Studies	31
Table 2.7 Solubility Values.....	33
Table 4.1 Proximate Analysis	46
Table 4.2 Physical Properties.....	49
Table 4.3 Elemental Analysis	51
Table 4.4 Adsorption Kinetic Model Parameters for 100mg/L of iron	74
Table 4.5 Adsorption kinetic parameters for copper from metal mixtures.....	93
Table 4.6 Element content analysis from XPS wide scan	97
Table 4.7 Surface area of pre and post adsorption crab char	106

List of Figures

Figure 4.1 TGA data from fast and slow pyrolysis.....	45
Figure 4.2 SEM Images of A-SP char and B-FP char	47
Figure 4.3. TEM images of A-fast pyrolysis char and B-slow pyrolysis char.....	48
Figure 4.4. FTIR spectra comparing slow and fast pyrolysis crab char	54
Figure 4.5. Solid-state NMR, ^{13}C (H) spectra comparing fast(pink) and slow(blue) pyrolysis ..	56
Figure 4.6. Zeta potential of SP and FP crab char	58
Figure 4.8 Iron pourbaix diagram based on this study's conditions.....	62
Figure 4.9 Validating AA results for comparison to a previous copper study	63
Figure 4.10 Removal of iron with a dosage of 5g/L	64
Figure 4.11 Effect of initial concentration on adsorption capacity of iron	66
Figure 4.12 Effect of initial pH on iron adsorption	67
Figure 4.13 Effect of temperature on iron adsorption.....	69
Figure 4.14 Comparing the effect of initial concentration on copper and iron as single metals .	72
Figure 4.15 Adsorption of iron over time as a single metal.....	73
Figure 4.16 Kinetic models for iron adsorption with crab char	75
Figure 4.17 Comparing the adsorption of copper and iron as single metals over time	77
Figure 4.18 Removal of iron and copper from a mixture (25mg/L of iron + 100mg/L of copper) with increasing dosage	79
Figure 4.19 Removal of iron and copper from a mixture (50mg/L of iron + 100mg/L of copper) with increasing dosage	80
Figure 4.20 Removal of iron and copper from a mixture (150mg/L of iron + 100mg/L of copper) with increasing dosage	81
Figure 4.21 Effect of initial pH on the removal of iron and copper from a mixture (150mg/L of iron + 100mg/L of copper).....	83
Figure 4.22 Effect of temperature on the removal of iron and copper from a mixture (75mg/L of iron + 100mg/L of copper).....	84
Figure 4.23 Adsorption capacity for copper as iron concentration increases	85
Figure 4.24 Adsorption capacity of iron in metal mixtures over time	87
Figure 4.25 Kinetic models for copper adsorption form a mixture (25mg/L of iron + 100mg/L of copper)	88
Figure 4.26 Kinetic models for copper adsorption from a mixture (50mg/L of iron + 100mg/L of copper)	89
Figure 4.27 Kinetic models for copper adsorption from a mixture (75mg/L of iron + 100mg/L of copper)	90
Figure 4.28 Kinetic models for copper adsorption from a mixture (150mg/L of iron + 100mg/L of copper).....	91
Figure 4.29 XPS spectra of crab char after adsorption of copper	98
Figure 4.30 XPS spectra of crab char after adsorption of iron	99
Figure 4.31 XPS high-resolution spectra of crab char before adsorption	100
Figure 4.32 XPS high-resolution spectra of crab chat after iron adsorption	101
Figure 4.33 XPS high-resolution spectra of crab after copper adsorption.....	102

Figure 4.34 XPS high-resolution spectra of crab char after mixture (75mg/L of iron + 100mg/L of copper)	103
Figure 4.35 XRD spectra of pre and post adsorption crab char from a mixture (75mg/L of iron + 100mg/L of copper)	104
Figure 4.36 Comparison of pre and post adsorption crab char from a mixture (75mg/L of iron + 100mg/L of copper)	105
Figure 4.37 TEM images of crab char before adsorption (A), after iron adsorption (B), after copper adsorption (C), and after mixture adsorption (75mg/L of iron + 100mg/L of copper)...	108

Abbreviations

AA Flame Atomic Adsorption Spectroscopy

AMD Acid mine drainage

BET Brunauer-Emmett-Teller

CCME The Canadian Counsel of Ministers for the Environment

CTC Chlortetracycline

CHN Carbon Hydrogen Nitrogen analysis

Cu Copper

Fe Iron

FP Fast pyrolysis

FT-IR Fourier Transform-Infrared Spectroscopy

ICP-OES Ion-coupled plasma optical emission spectroscopy

PFO Pseudo-first order model

PSO Pseudo-second order model

RMSE Random mean square error

SEM Scanning electron microscopy

SP Slow pyrolysis

SSA Specific surface area

TGA Thermal gravimetric analysis

XPS X-Ray photoelectron spectroscopy

XRD X-ray diffraction

Chapter 1: Introduction and Overview

Two environmental issues are addressed by using marine crustacean biochar to remove metals from water, marine food waste, and acid mine drainage. Marine crustacean waste is generated as a by-product of seafood processing, such as canneries and the separation of body parts such as crab legs for market sales, resulting in approximately 1.3 billion tonnes of seafood waste annually ¹. Marine crustacean waste is generally disposed of in landfills which produce greenhouse gases through decomposition and involve high costs in handling and disposal, such as fuel and labour. Marine waste is also dumped into the ocean, adversely affecting the ecosystem, species distribution, and possibly tourism due to odours and scavenger populations. Due to the limited capacity for dumping, finding alternative uses for this food processing waste is crucial. Acid mine drainage (AMD) is an environmental and drinking water hazard worldwide. Pyrite, also known as Fool's gold, is the most common source of AMD ^{2 3 4}. Mining opens the rock and exposes it to air and water, producing iron sulphates and weak sulphuric acid, mobilizing heavy metals such as zinc, copper, manganese, and nickel. High sulphate concentrations (1000 to 130,000 mg/L) and dissolved ferrous metals (14 to 29800mg/L) are typical of AMD ^{2 3 4}. The Canadian Mine Environment Neutral Drainage Program estimated that the total environmental liability costs due to AMD at mine sites could be approximately 2 to 5 billion dollars ⁵. Discharging untreated mining effluent into natural water bodies reduces the pH and dissolved oxygen, in addition to the dissolution of metals from the bottom sediment, negatively impacting the aquatic ecosystem. The water often becomes unsuitable for domestic, agricultural, and industrial uses ³. Criteria from The Canadian Council of Ministers for the Environment (CCME) require that mining effluent not be acutely toxic, the pH must be greater than 6 and less than 9.5, and the concentration of copper must

be less than 0.30mg/L⁶. The health effects of excess copper include anemia and liver and kidney damage⁴. AMD is commonly treated with lime (Ca (OH)₂) because it is abundant, cheap, low toxicity, and technically simple. Lime removes dissolved metals through increasing pH to cause metal precipitation and has been used for over 50 years⁷. The disadvantages of this treatment method include high volumes of solid wastes that require transportation and storage with equipment scaling that requires shutdowns for maintenance⁸.

Given that crustacean biochar is relatively new to research and is globally available as food waste, further research on the pyrolysis conditions, chemical characteristics, and potential applications is essential to determine alternative methods to dumping crustacean shells and neutralization of AMD with lime.

Pyrolysis is the thermal degradation of biomass in an oxygen-free environment. The free radical reactions caused by covalent bond breaking are the chemical mechanism of pyrolysis. Slow pyrolysis typically has a heating rate below 10 °C/min, a final temperature between 300-500°C, and most importantly, a retention time of tens of minutes to hours⁹. The fast pyrolysis method has a heating rate greater than 10 °C/min, a final temperature between 300-600 °C, and a holding time of seconds to a few minutes. A literature review determined that slow pyrolysis was used in most crustacean studies^{10 11 12 13 14 15 16}. Of the slow pyrolysis studies, the final temperatures and heating rates varied, some above the typical conditions for slow pyrolysis. However, the holding times were all in the slow pyrolysis range. This study also compares the physical and chemical characteristics of crab char from fast and slow pyrolysis through lab-scale experiments.

Comparing slow and fast pyrolysis of a common feedstock provides valuable information on production rates, yield quality, the thermal stability of the feedstock, and potential profitability⁹. Although there is significant literature comparing slow and fast pyrolysis on plant-based

feedstocks to the best of our knowledge, a comparison of slow and fast pyrolysis of snow crab waste has not been completed^{17 18 19 20}. Generally, slow pyrolysis is preferred when solid biochar is the desired product, and fast pyrolysis is when liquid oil is the preferred product. From lignocellulose studies, slow pyrolysis produces approximately 30-45% char and 20--30% liquids⁹, while fast pyrolysis produces 60 – 75% oil and 15-25% char²¹. Yuan et al., (2019) showed that the fast pyrolysis of walnut shells is more conducive to releasing volatiles and that slow pyrolysis is more favourable for biochar production²². Crab shells, however, are composed of calcium and contain no cellulose or lignin. Therefore, the general trends from lignocellulose research on yields and porosity for fast and slow pyrolysis do not apply to crab biomass pyrolysis.

1.1 Scope and Objectives

Marine crustacean biochar is a recent topic in adsorbent research, and there are few studies on crustacean biochar as an adsorbent for aqueous metal mixtures. A study using small-scale, fast pyrolysis of Snow Crab focussed on copper removal. The next sequential step is a larger-scale pyrolysis unit and adding another AMD metal and iron is the standard issue between various types of AMD. However, no studies were found on treating a copper–iron solution with crab biochar. Therefore, this study investigated the potential of crab biochar as an adsorbent to treat a solution of copper and iron.

Main objectives:

1. The investigation of previous adsorption studies using marine crustacean biochar, particularly metals, through a comprehensive literature review
2. The production of slow pyrolysis crab char.
3. Compare the chemical, physical, and structural characterization of fast and slow pyrolysis crab biochar.
4. Conducting batch equilibrium adsorption tests using iron and copper and varying different parameters (initial pH, adsorbent dose, temperature, and initial metal concentration)
5. Determine the adsorption capacities of iron and copper to understand the nature and extent of adsorption
6. Adsorption kinetic modelling to investigate the effect that adding iron has on copper's adsorption rate.

1.2 Thesis Organization

The thesis is written in the Traditional format and is organized into several chapters. Chapter one includes background information to validate this research topic, its scope, and objectives, and how the thesis was organized. Chapter two is a literature review of related research. Chapter three describes the methodology used. Chapter four compares the characteristics of slow pyrolysis and fast pyrolysis crab char. Chapter five presents the experimental results and discussion, and chapter six summarizes the conclusions and recommendations for future research.

Chapter 2: Literature Review

2.1 Introduction

Over the past few years, marine biomass as a renewable resource has attracted increased attention because of the volume of waste and associated environmental impacts generated by the seafood industry. Humans produce approximately 1.3 billion tonnes of seafood waste annually, with shrimp, crab, and lobster contributing 6 – 8 million tons of waste per year^{1 23}. Current methods of handling this waste include manufacturing fish feed, pet food additives, fertilizer, and fish oil^{1 23 24}. Although the waste is considered compostable, landfilling marine waste produces greenhouse gases such as carbon dioxide and methane during decomposition²⁵. An alternative to landfills for marine waste is ocean dumping. Ocean dumping reduces the dissolved oxygen through the decomposition of organic matter and reduces sunlight penetration to the seafloor because of the materials suspended in the water. Subsequently, this decreases the biodiversity within that area, particularly photosynthetic species²⁶. Concentrated nutrients from ocean dumping result in a rapid increase in algae, called an algal bloom²⁷. In addition, scavenger species such as seagulls and crabs congregate near the waste discharge impacting the natural distribution and ecosystem balance within the dumping area. It also creates unpleasant odours and water conditions, which affect tourism²⁸.

Converting biomass via thermochemical conversion into other products such as biochar, fuels, and chemical building blocks diverts the waste from landfills and oceans. Thermochemical conversion processes include pyrolysis, liquefaction, and gasification. These methods vary by operating parameters and design (temperature, pressure, residence time, reactor design/configuration, and reaction atmosphere) and produce various products²⁹. Deciding which process to use, depends on the application and market value²⁹.

Pyrolysis involves heating biomass in an oxygen-limited environment to a target temperature, under a specific heating rate, for a particular amount of time. It can include catalysts and pressure variations. Pyrolysis produces three main products solid char, liquid, and gas ³⁰. Pyrolysis conditions determine the amount of product. There are several types of pyrolysis, including slow, intermediate, fast, flash, microwave, and hydrothermal pyrolysis.

Slow pyrolysis occurs at temperatures ranging from 300-500 °C with a temperature ramp below 10 °C/minute and a furnace residence time of hours. Slow pyrolysis produces approximately 35 wt% char, 30 wt% liquids, and 35 wt% non-condensable gases ⁹. Slow pyrolysis is often used when biochar production is favoured. Comparatively, fast pyrolysis is performed at temperatures from 300 – 600 °C, a heat ramp between 10-200°C/minute ²¹, with a very short vapour residence time from seconds to minutes ²⁹. Fast pyrolysis produces 60 – 75 wt% oil, 15-25 wt% char, and 10-20 wt% non-condensable gases ²¹. Flash pyrolysis also produces a similar product yield as fast pyrolysis but has a shorter residence time and greater heating rates of over 1000 °C/s ³¹. The pyrolysis conditions selected depend on the type of biomass.

Waste from seafood processing often contains calcium from fish bones and shells, proteins, pigments, and lipids, including fatty acids ^{32 33 34 35}. Calcium is typically in the form of calcium carbonate and is an important mineral used extensively in agriculture as a soil additive for neutralization and as a component in animal feed. For industrial processes, calcium carbonate is used for paper production, in the mortar for bonding bricks and rubber compounds, and as a filler in paint and plastics ³⁶. Calcium carbonate is also thermally converted into calcium oxide, used for glass and steel production ³⁶. The majority of calcium carbonate used for the industry is produced naturally from the sedimentation and fossilization of shelled organisms, forming rocks such as marble and limestone ³⁶. However, there is a limited supply because rock formation does

not occur on an industrial timescale. Obtaining calcium carbonate requires quarries or mining, making this process both non-renewable and energy intensive. This process is not sustainable, and like our reliance on fossil fuels, we must also consider alternative sources of calcium carbonate.

This review will summarize research on slow and fast pyrolysis of marine biochar from crustaceans (crab, crayfish, shrimp), focusing on biochar characteristics and metal adsorption.

2.2 Crustacean Feedstocks

Every year, 1.5 million tons of crabs are consumed annually, generating about 0.5 million tons of crab shells as waste³⁷. Thirty percent of this mass is wasted during food processing, where the shoulders and legs are considered the valuable food component. The remaining mass is dumped into landfills or used as fertilizer or animal/fish feed^{1 23 38}. Table 2.1 provides the composition of the crustacean feedstocks. Snow crab is commercially fished with significant economic value, while the blue and green crab are invasive species, affecting local fishery and ecosystem balances. Lage-Yusty et al., 2011 determined that snow crab was composed of water (72 wt%), proteins (34.2 wt%), lipids (17.1 wt%), and ash (28.5 wt%)³⁹, while Beaulieu et al., 2009 found that snow crab contained 16.2 wt% chitin⁴⁰. Naczka et al., (2004) showed that green crabs from the North Atlantic were primarily composed of water (72 wt%), protein (5.6 wt%), chitin (4.41 wt%), and lipids (0.51 wt%). Hamdi et al., (2020) determined that the composition of blue crab was water (55.6 wt%), chitin (27 wt%), protein (11.25 wt%), lipids (1.07 wt%), and ash (59.11 wt%)⁴¹. In blue crab, the ash included calcium carbonate, silica, and phosphates³⁸.

In 2019, 2 089 000 tons of crayfish were produced through global aquaculture. Only the tail is eaten, and 80 wt% of the crayfish are wasted⁴². Conventional treatment of crayfish waste includes conversion to fertilizer, animal feed, and disposal into landfills. Park et al., (2018) studied the shell composition of crayfish and found that it contained silica (58.5 wt%), iron (36.2 wt%), aluminum (28.4 wt%), carbon (27.9 wt%), and calcium (17 wt%)⁴². Crayfish contained approximately 28.2 wt% ash and had a pH of 8.7, due to the calcium content of the shell⁴². Crayfish waste is an optimal feedstock for biochar because of its volume and widespread distribution.

Kalayda et al., (2019) completed a chemical analysis on narrow-toed crayfish (*Pontastacus leptodactylus Esch.*) to determine the nutrient composition of the consumer product. The moisture content of the crayfish wt%raw shell was 59.2 wt%. In addition, the raw shell had 36.4 wt% organic content wt% and the calcium content was 376,282 g/kg⁴³.

Globally, 3.4 million tons of shrimp are harvested¹⁰. In shrimp processing, 60 wt% of the shrimp are wasted because the shell and head are removed⁴⁴. Shrimp live in fresh and saltwater and are a food source for fish, crabs, sea urchins, whales, dolphins, and humans⁴⁵. The most common source of calcium supplements is dried shrimp³³. The raw shell has calcium in the form of calcium carbonate and calcium polyhydroxy phosphate. Table 2.1 below contains the composition of raw shrimp waste^{46 47 48}. Huang et al., (2021) used Mantis shrimp (*Oratosquilla oratoria*) to produce biochar⁴⁷, Shahidi et al., (1991) investigated the nutritional composition of Cold-water shrimp waste (*Pandalus borealis*)⁴⁸, and Kannan et al., (2017) used a mixture of Pink, Brown and Tiger shrimp to make biochar⁴⁶. The shrimp shells contained mainly chitin (17%)⁴⁸ and carbon (27.44 wt%) with a lesser elemental composition of nitrogen (4.61 wt%), hydrogen (4.38 wt%), and sulphur (1.01 wt%).

Table 2.1 Composition of Marine Crustaceans

Feedstock	Moisture (%w/w)	% Volatiles	% Minerals	% Chitin	% Lipids	% Proteins	Ash (wt%)	C (wt%)	H (wt%)	N (wt%)	Reference
Snow Crab	72	--	--	16.2	17.1	34.2	28.5	--	--	--	Lage-Yusty et al., 2011 ³⁹ Beaulieu et al., 2009 ⁴⁰
Blue Crab	55.6	--	--	27.53	1.07	11.25	59.11	--	--	--	Hamdi et al., 2020 ⁴¹
Green Crab	--	--	--	4.41	0.51	5.6	--	--	--	--	Naczk et al., 2004 ⁴⁹
Narrow-toed crayfish	59.2	36.4	4.38	--	--	--	--	--	--	--	Kalayday et al., 2019 ⁴³
Raw shell											
Crawfish, Louisiana, U.S.A	--	--	--	--	--	--	28.2	27.9	--	5.5	Park et al., 2018 ⁴²
Mantis shrimp	--	--	--	--	--	--	--	27.44	4.38	4.61	Huang et al., 2021 ⁴⁷
Coldwater Shrimp	--	--	--	17.01	--	41.90	--	--	--	--	Shahidi et al., 1991 ⁴⁸
Mixed Shrimp (Pink, Brown, and Tiger)	--	--	--	--	--	--	--	43.09	6.91	11.47	Kannan et al., 2017 ⁴⁶

2.3 Biochar Characteristics

Table 2.2 provides the physiochemical characteristics of crustacean biochar from fast (FP) and slow (SP) pyrolysis.

Hopkins et al., (2022) generated fast pyrolysis crab char with a pyrolysis temperature of 500°C for five minutes with a 52.7 wt% char yield and an ash content of 57.32 wt%. The char showed a surface area of 20.71 m²/g and contained a carbon content of 20.16 wt%, a hydrogen content of 0.40 wt%, and a nitrogen content of 2.27 wt%⁵⁰.

Chen et al., (2020) used slow pyrolysis at 500°C for one and a half hours on crab and produced char with a carbon content of 16.78 wt%, a hydrogen content of 2.21 wt%, an oxygen content of 1.06 wt%, and an ash content of 47 wt%. The char showed a surface area of 37.17 m²/g, a total volume of 0.14cm³/g, and a pore diameter of 7.87nm¹¹.

Dai et al., (2017) produced a slow pyrolysis crab with pyrolysis temperatures ranging from 300°C to 900°C for two hours. At 500°C, char yield was 58 wt% with an ash content of 65 wt% and a surface area of 52.13 m²/g. The elemental composition included a carbon content of 18.2 wt%, a hydrogen content of 0.28 wt%, and a nitrogen content of 2.01 wt%. At 600°C, the char contained calcite, and at 900°C the char contained lime. The yield decreased with temperature and the ash content increased with temperature¹⁰.

Xu et al., (2020) generated slow pyrolysis crab char with a pyrolysis temperature of 800°C for two hours with a surface area of 81.57 m²/g and carbon content of 11.19 wt%, hydrogen content of 1.62 wt%, and nitrogen content of 65.4 wt%¹².

Sebastyen et al., (2020) studied the thermal degradation of crab shells to determine the extent to which nitrogen would remain in the fast pyrolysis char as a potential nitrogen-containing adsorbent

and identify compounds lost during heating. The shell sample was pyrolyzed at 320 and 500 °C for 20 s in a helium atmosphere using a Pyroprobe 2000 pyrolyzer interfaced with an Agilent 6890A/5973 GC/MS. The crab shell was composed of 0.3 wt% ash, which included hydroxylapatite, $\text{Ca}_5(\text{PO}_4)_3\text{OH}$. At 500°C, 50 % of nitrogen remained in the fast pyrolysis biochar, and they identified at least 40 volatiles during pyrolysis. Sun et al., (2021) used crayfish with pyrolysis temperatures of 300°C, 500°C, and 700°C. At 500°C, the yield was 54.66 wt% with an ash content of 79.26 wt%, a surface area of 29.64 m²/g, a carbon content of 18.35 wt%, and a hydrogen content of 0.51 wt%, and nitrogen content of 0.77 wt%³⁸.

Park et al., (2018) produced crayfish biochar with pyrolysis temperatures of 200°C, 400°C, 600°C, and 800°C with a 48.6 wt% char yield, a surface area of 50.1 m²/g, the carbon content of 19.5 wt%, the nitrogen content of 2.1 wt% and calcium content of 32.5 wt%⁴².

Huang et al., (2021) used Mantis shrimp shells to prepare nitrogen and sulphur co-doped hierarchical porous biochar for research into use as supercapacitors. Shrimp was pyrolyzed at a heating rate of 5 °C/min for the temperatures of 700, 750, 800, 850, and 900 °C for 1.5 h. After slow pyrolysis, the char was dissolved in nitric acid. The result was high nitrogen (8.2 wt%) and sulphur content (1.16 wt%) biochar with nitrogen and sulphur heteroatoms located on the carbon frameworks. The highest specific capacitance was 201 F/g at a current density of 1 A/g. The authors concluded that this was a promising electrode material. At 700°C, the surface area was 270 m²/g, with a carbon content of 48.52 wt%, a hydrogen content of 2.25 wt%, and a nitrogen content of 7.72 wt%. At 900°C, the surface area was 176 m²/g, with a carbon content of 48.52 wt%, a hydrogen content of 0.98 wt%, and a nitrogen content of 3.18 wt%⁴⁷.

Zhang et al., (2019) compared the fast and slow pyrolysis of shrimp at 600°C. The holding time was the same for fast and slow pyrolysis, 20 minutes; however, the fast pyrolysis had instant

exposure to 600°C, while slow pyrolysis ramped at 15°C/min, comparing the effect of heat ramping. The slow and fast pyrolysis char had a yield of 35 and 32 wt%, respectively. The nitrogen content was 5.37 and 4.81 wt%, respectively ⁵¹.

Yu et al., (2020) studied shrimp biochar for 2,4-Dichlorophenol(2,4-DCP), removal to use the biochar as a catalyst for the persulfate-induced advanced oxidation process. Shrimp biochar pretreated with hydrochloric acid (HCl) was compared to plain shrimp biochar. The activation mechanism was studied via quenching experiments, ESR detection, and electrochemical characterization. Shrimp pre-treated with HCl and pyrolyzed at 800°C had the highest removal (54%) and the best catalytic activity due to increased porosity, with a total volume of 0.93 cc/g and a surface area of 594 m²/g ¹⁵.

Kannan et al. (2018) used hydrothermal carbonization (HTC) of shrimp waste to compare the results of their 2017 study using microwave hydrothermal conversion (MHTC) of shrimp waste. The shrimp waste was pre-treated with enzymes to maximize the hydrolysis of the waste to produce glucose, as well as to reduce the amount of energy required to make biochar. The optimal conditions for HTC of shrimp required a holding temperature of 184°C and a holding time of 112 minutes, resulting in a char yield of 29 wt%. The optimal conditions for MHTC required a holding temperature of 186°C, and a holding time of 120 minutes, resulting in a yield of 42 wt%. The carbon content was slightly higher with HTC than MHTC at 50.36 wt% versus 45.73 wt%, respectively. Nitrogen content was also higher with HTC than MHTC at 6.03 wt% versus 4.91 wt%, respectively. However, for oxygen and hydrogen content, the values were higher with MHTC, with 43.19 wt% versus 37.47 wt%, and 6.06 wt% versus 5.64 wt%, respectively. The volatile matter content was also higher with MHTC with 65.51 wt% versus 38.99 wt%, respectively. Both methods had similar results for ash content ranging from 21.25 to 21.98 wt%.

Overall, the HTC of shrimp had a higher carbon and moisture content and a lower volatile matter content than MHTC⁵². Crustacean chars from 500°C indicated differences between fast and slow pyrolysis. Fast pyrolysis (FP) crab yield was less than slow pyrolysis (SP) crab and crayfish, with 52.7 wt%⁵⁰ versus 58 wt%¹⁰ and 54.66 wt%, respectively. Fast pyrolysis produced a smaller surface area, with 20.71 m²/g versus 37.17 m²/g¹¹ and 52.13 m²/g¹⁰ for crab and 29.64 wt%¹³ for crayfish. SP crab above 500°C and FP crab were compared and found that SP surface area increased with temperature. The surface area of SP Crayfish at 700°C, 53.01 m²/g, was very similar to FP crab at 500°C. Ash content of FP crab char was higher than SP crab, with 57.32 wt% versus 47 wt%¹¹ and 55 wt%¹⁰, respectively, whereas SP crayfish's ash content was much higher at 79.26 wt%. Potentially due to different species. FP crab char's carbon content was higher than all of the SP char at 20.16 wt% versus 16.78-18.35 wt%, respectively^{10 13}. The hydrogen content of FP crab was significantly less than the SP char with 0.4wt% versus 2.17-2.21 wt%. Nitrogen content of FP crab was slightly higher than Dai et al., (2017)¹⁰ with 2.27 wt% versus 2.01 wt% respectively, however, the content of Chen et al., (2020)¹¹ was 0.589 wt% and SP crayfish was 0.77 wt%, making comparison difficult. FP crab's calcium content based on TGA was 33.77 wt%, slightly higher than SP crab and marginally lower than SP crayfish with 27.35 wt% and 34.98 wt%, respectively. Zhang et al., (2019) compared the fast and slow pyrolysis of shrimp based on fast pyrolysis having no heat ramp and both fast and slow pyrolysis having the same holding time. FP shrimp from Zhang et al (2019) was compared to SP crayfish from Park et al., at 600°C⁴² since the shrimp was held for 20 minutes and the crayfish held for two hours. The yield of FP shrimp was less than the SP crayfish at 32 wt% and 48.6 wt% respectively, however the surface area of the FP shrimp was higher than the SP crayfish with 63.70 m²/g and 29.64 m²/g respectively. FP shrimp had a higher ash content than SP crayfish at 73.54 wt% versus 50.1 wt% respectively and

a higher calcium content, 68.86 wt% versus 32.5 wt%. respectively. Zhang et al., (2019) found that having no heat ramp produced a slightly higher ash and calcium carbonate content ⁵¹. SP crab had a slightly higher pore diameter than FP crab with 7.87nm versus 5nm. SP crayfish at 700°C had very similar pore diameter to FP crab with 5.64nm.

SP crab above 500°C and FP crab were compared, and found that yield decreased for SP with increasing temperature, changing the yield of SP crab at 900°C to be below SP crab at 600°C.

Zhang et al., (2019) compared the fast and slow pyrolysis of shrimp based on fast having no heat ramp and both fast and slow having the same holding time. The yield of FP shrimp was 32 wt%, and they found that no heat ramp produced slightly higher ash and calcium carbonate content. Overall, fast pyrolysis crustacean char had a similar surface area, and pore diameter, with a higher carbon content than slow pyrolysis crustacean char.

Table 2.2 Comparing Crustacean Biochar from Fast (FP) and Slow Pyrolysis (SP)

Feedstock & Treatment	Pyrolysis Conditions	Ramp (°C/min)	Yield (wt%)	pHpzc	S _{BET} (m ² /g)	V _{tot} (cm ³ /g)	Dp (nm)	pH	C (wt%)	H (wt%)	O (wt%)	N(wt %) (wt%)	Ca	Ash (wt%)	Reference.
Crab FP	500°C 5 min	No ramp	52.7	7.1	20.71	--	5	11.75	20.16	0.40	--	2.27	33.77	57.32	Hopkins et al., 2022 ⁵⁰
Crab SP	500 °C 1hr. Char Char + NPs	8	--	--	37.17	0.14	7.87	--	16.78	2.215 0.94	1.065 2.2	0.586	420 mg/g	47	Chen et al., 2020 ¹¹
Crab SP	300°C 500°C 900°C 2h	10	64.3 58 38.74	--	3.52 14.9 48.44	0.012 0.023 0.048mg/L	--	11.25, 11.714	25.21, 20.68	2.21, 0.97	--	3.26 2.38 <1.00	22.91 26.36 36.14	46.6, 55, 67	Dai et al., 2017 ¹⁰
Crab SP	800°C 2h	10	--	--	81.57	0.086	2-50	12.36	11.29	1.62	--	1.62	36.14	--	Xu et al, 2019 ¹²
Crayfish SP	300, 500, 700 °C 2h	15	70.98 54.66 53.01	9.76 9.72 11.44	11.9 29.64 21.75	0.04 0.11 0.13	13.08 15.38 13.41	10.57 10.78 13.41	27.15 18.35 16.85	2.17 0.51 0.34	0.49 1.11 2.17	2.36 0.77 0.63	34.55 34.98 35.77	67.82 79.26 80.02	Sun et al.,2021 ¹³
Crayfish SP	200 400 600 800 2h	No Ramp	83.1 56.5 48.6 35.3	--	30.6 43.8 50.1 67.3	--	--	9.2 9.4 9.8 12.1	30.5 24 19.5 9.4	--	--	6.4 3.2 2.1 0.3	17.1 27.5 32.5 41.2	30.6 43.8 50.1 67.3	Park et al., 2018 ⁴²
Crayfish SP	300 450 600 2h	No Ramp	42 40 16	--	32.67 25.46 63.79	--	--	--	23.45 20.63 21.17	0.92 0.31 0.22	--	1.85 1.28 1.26	20.47 22.56 16.08	--	Xiao et al., 2017 ⁵³
Crayfish	400 600 800 2 h				33 376 59	0.042 0.33 0.20	2.56 4.0 6.7								Yu et al., 2020 ¹⁵
Shrimp FP	600°C, 20 min.	No Ramp	32	--	63.70 ⁵⁴	--	--	--	--	--	--	4.81	--	73.54	Zhang et al., 2019

Feedstock & Treatment	Pyrolysis Conditions	Ramp (°C/min)	Yield (wt%)	pHpzc	S _{BET} (m ² /g)	V _{tot} (cm ³ /g)	Dp (nm)	pH	C (wt%)	H (wt%)	O (wt%)	N(wt % (wt%)	Ca	Ash (wt%)	Reference.
Shrimp SP	600°C, 20 min.	15°C/min	35	--	--	--	--	--	--	--	--	5.37	--	70.25	Zhang et al., 2019 ¹¹
Shrimp SP	700	5	--	--	270	0.31	5.64	--	64.28	2.25	--	7.72	--	--	Huang et al., 2021 ⁴⁷
Pre-treated	750				401	0.62	6.97		69.02	1.97		8.20			
HN0 ₃	800				334	0.63	7.92		68.31	1.65		7.45			
	850, 1.5h				355	0.77	8.70		61.56	1.42		6.27			
Shrimp SP	400 °C, 600 °C 800 °C 2 h.	5	--	Negative values	33 29 59	0.042 0.07 0.2	5.12 9.6 13.4	--	78.41	--	9.76	--	--	--	Yu et al., 2020 ¹⁵
Shrimp HTC	184 °C, 2h	No Ramp	29	--	--	--	--	--	29	5.64	37.47	6.03	--	21.25	Kannan et al., 2017 ⁴⁶
Shrimp Microwave HTC	184 °C, 2h	No Ramp	42	--	--	--	--	--	42	6.06	43.19	4.91	--	21.98	Kannan et al., 2017 ⁵²

2.4 Crustacean Biochar Adsorption Studies

Research concerning crab-based biochar is still in its infancy. However, several studies using crab biochar have been conducted. Table 2.3 contains a recent list of these studies^{37 50 11 10 12 51 55 56 57 58 59}.

Table 2.3 Crab Biochar Studies

Title	Reference
Removal of copper from sulphate solutions using biochar derived from crab processing by-product	Hopkins et al., 2022 ⁵⁰
Ultimate Resourcization of waste: crab shell derived biochar for antimony removal and sequential utilization as an anode for a Li-ion battery	Zhang et al., 2021 ⁵⁹
Facile Preparation (Hydrothermal) of a Porous Biochar Derived from Waste Crab Shell with High Removal Performance for Diesel	Han et al., 2020 ⁵⁵
Highly Efficient Adsorption of P-Xylene from Aqueous Solutions by Hierarchical Nanoporous Biochar Derived from Crab Shell	Chen et al., 2020a ⁵⁶
Synthesis and Characterization of a Novel Magnetic Calcium-Rich Nanocomposite and Its Remediation Behaviour for As(III) and Pb(II) Co-Contamination in Aqueous Systems	Chen et al., 2020b ¹¹
Effective Adsorption of Diesel Oil by Crab-Shell-Derived Biochar Nanomaterials	Cai et al., 2019 ⁵⁷
Interaction between Chlortetracycline and Calcium-Rich Biochar: Enhanced Removal by Adsorption Coupled with Flocculation	Xu et al., 2019 ¹²
Calcium-Rich Biochar from Crab Shell: An Unexpected Super Adsorbent for Dye Removal.	Dai et al., 2018 ¹⁶
Preparation, Characterization, and Environmental/Electrochemical Energy Storage Testing of Low-Cost Biochar from Natural Chitin Obtained via Pyrolysis at Mild Conditions.	Magnacca et al., 2018 ⁵⁸
Calcium-rich biochar from the pyrolysis of crab shell for phosphorus removal	Dai et al., 2017
Crab Shells as Sustainable Templates from Nature for Nanostructured Battery Electrodes	Yao et al., 2013

Hopkins et al., (2022) used fast pyrolysis to produce crab biochar and tested for absorbance of copper in a sulphate-rich solution. The maximum adsorption capacity was 184.8 mg/g for Cu^{2+} and was fit by the Pseudo-Second Order (PSO) model. The pseudo-second-order kinetic model assumes that the rate-limiting step is chemisorption, and the adsorption rate is dependent on adsorption capacity. The author indicated that precipitation was the adsorption mechanism and that this method had potential as a treatment method for acid mine drainage ⁵⁰.

Zhang et al., (2021) prepared Fe-La-doped crab biochar for adsorbing Sb(III) and Sb(V). The crab was pretreated at 350 °C for 3 h, immersed in EDTA-2Na, doped with iron and lanthanum oxides, and finally heated to 900°C for 2h. At 40 °C, it had a maximum capacity of 498 and 337 mg/g and fit with the pseudo-second-order kinetic model, and fit by the Langmuir model, indicating that the adsorbate adsorption is limited to one molecular layer. After adsorbing the antimony, the char was heated at 600°C and tested as an anode material for a Lithium-ion battery. The crab biochar had a reversible specific capacity of 833.8 mAh/g after 500 cycles, and the authors concluded good performance for anode material and antimony absorbance ⁵⁹.

Han et al., (2020) used pre-treatment and hydrothermal carbonization to prepare biochar for diesel adsorption. The crab was soaked in hydrochloric acid, then in sodium hydroxide, and dried before mixing with acetic acid. The pretreated crab was placed at 180°C for 10 h in an oven. Adsorption was fitted by the Langmuir isotherm model, indicating mono-layer adsorption, and the kinetic pseudo-second-order model, indicating chemisorption. The equilibrium adsorption capacity for diesel was 480.6mg/g with a removal rate of 80.1wt%, making this a promising adsorbent for diesel spills ⁵⁵.

Chen et al., (2020a) studied the adsorption of P-xylene with activated crab biochar. Pre-treatment included immersion in hydrochloric acid before being carbonized under nitrogen flow at 700°C for 2 hours. The highest adsorption capacity (393 mg/g) occurred under neutral conditions due to the interactions of negatively charged oxygen-bearing functional groups on crab biochar, and positively charged π electrons of ring structures could cause strong electrostatic interactions, increasing the adsorption capacity. The removal rate of P-xylene reached 97.5%, making this biochar a potential adsorbent for P-xylene ⁵⁶.

Chen et al. (2020b) made magnetic crab biochar by modifying the crab with Fe₃O₄ nanoparticles to retrieve the biochar from wastewater and tested the biochar's adsorption for arsenic and lead. The study included testing arsenic and lead separately and as a mixture to mimic real industrial effluent. Maximum removal capacities for arsenic and lead were 15.8mg/g and 62.4 mg/g, respectively, at a pH of 6, and there were competitive and synergistic effects between arsenic and lead. Since these removal rates are less than 20% for the As-Pb mixture, this biochar was not an optimum adsorbent for mixture ¹¹.

Cai et al., (2019) investigated the adsorption of diesel oil with crab biochar and crab biochar augmented with potassium hydroxide. Pyrolysis conditions included a heat ramp of 10 °C/min to 700 °C for two hours under a nitrogen flow. The potassium hydroxide increased the biochar surface area from 307 to 2441 m²/g, and the increased surface area was due to the separation of biochar layers and cracks caused by the KOH activation. The maximum adsorption capacity (93.9 mg/g) from the KOH biochar required a pH of 7 ⁵⁷.

Xu et al. (2020) studied crab biochar and the removal of chlortetracycline (CTC), which is an antibiotic found in wastewaters. The removal efficiency reached approximately 90% within 20

minutes due to the interaction between the calcium hydroxide and the calcite on the surface of biochar with the CTC. In addition, the CTC molecule had an aromatic structure that can act as an electron donor so that the π - π electron donor-acceptor interaction can form between the biochar and the CTC molecule. Adsorption was still optimum after 5 cycles of reusability tests. To mimic wastewater in a natural environment, crab biochar was tested with the CTC mixed with humic acids obtained from natural organic matter. A slight increase in the humic acid concentration inhibited the removal efficiency of CTC. Therefore, crab biochar may be a viable application for point source remediation of CTC ¹².

Dai et al. (2018) used crab biochar to test the adsorption of industrial dyes, cationic malachite green and anionic congo red. Maximum adsorption occurred with biochar formed at 800°C, a neutral pH for malachite green (12,502 mg/g) and a pH of 4 with congo red (20,317 mg/g) due to the electrostatic attraction as the source of adsorption for both dyes. Reusability testing indicated a limited lifespan for crab biochar when applied to dye removal ¹⁶.

Magnacca et al, (2018) used commercial chitin derived from Snow Crab to make biochar for testing electrochemical storage, carbon dioxide, and dye adsorption (cationic methylene blue and anionic methyl orange). Chitin was pyrolyzed with a heating ramp of 10 °C min/min, followed by isothermal steps for 1 h. Target temperatures were 294 °C (initial temperature of chitin degradation), 440 °C, and 540 °C. Chitin biochar (440°C) adsorbed half the carbon dioxide that the commercial carbon (Carboxen 1033) removed. The chitin biochar with the highest adsorption for methylene blue(26.7mg/g) was pyrolyzed at 440°C. The chitin biochar with the highest adsorption for methyl orange (16.0 mg/g) was pyrolyzed at 540°C. The increased adsorption was linked to the larger biochar surface areas. The reusability tests resulted in decreased dye removal with each cycle. To be tested as cathode material in Li-S batteries, the chars were augmented with

sulphur. Results from chitin biochar (294°C) included high polarization and initial stable discharge capacity. This crab chitin biochar had potential applications for energy and adsorbent applications ⁵⁸.

Yao et al., (2013) studied carbon nanofibers for nanostructured battery electrode structure. The porous carbon nanofibers were formed with a polyacrylonitrile/dimethylformamide solution infusion method. The fibres were used to hold sulphur and silicon to form electrodes for Li-ion batteries. The resulting specific capacities were 1230mAh/g for sulphur and 3060 mAh/g for silicon and 200 cycles with 60 wt% (sulphur) and 95 wt% (silicon) capacity retention, indicating that this crab biomass was a low-cost, sustainable option for electrical nanomaterials ³⁷.

A list of recent adsorption studies on crayfish biochar is in Table 2.4^{53 60 61 42 51 13 62}.

Table 2.4 Crayfish Biochar Studies

Title	Reference
Sorption of Heavy Metal Ions onto Crayfish Shell Biochar: Effect of Pyrolysis Temperature, PH and Ionic Strength.	Xiao et al., 2017 ⁵³
Synthesis, Characterization, and Mechanism Analysis of Modified Crayfish Shell Biochar Possessed ZnO Nanoparticles to Remove Trichloroacetic Acid.	Long et al., 2017 ⁶⁰
Adsorptive removal of As(V) by crayfish shell biochar: batch and column tests	Yan et al., 2018 ⁶¹
Effect of Pyrolysis Temperature on Phosphate Adsorption Characteristics and Mechanisms of Crayfish	Park et al., 2018 ⁴²
Desorption of Calcium-Rich Crayfish Shell Biochar for the Removal of Lead from Aqueous Solutions.	Zhang et al., 2019 ⁶³
Crayfish shell biochar for the mitigation of Pb contaminated water and soil: Characteristics, mechanisms, and applications	Sun et al., 2021 ¹³
Enhanced adsorption for the removal of tetracycline hydrochloride (TC) using ball-milled biochar derived from crayfish shell	Zhang et al., 2021b ⁶²

Xiao et al., (2017) used slow pyrolysis with temperatures of 300, 450, and 600°C for the adsorption of lead, arsenic, and copper. Increased pyrolysis temperature increased the surface area from 32.67 to 63.79 m²/g and decreased the content of carbon, hydrogen, nitrogen, and sulphur. There was a decrease in functional groups between 300 and 400°C, in O–H stretching, C=O stretching and C–H bending vibrations. Lead outcompeted other metals studied, with an adsorption capacity of 5 mg/g, versus 3.57mg/g and 2.03mg/g for Cu (II) and As (III), respectively. In single metal solutions, the lead had maximum adsorption of 190.7mg/g and depended on pH and ionic strength⁵³.

Long et al., (2017) used zinc oxide (ZnO) modified, slow pyrolysis biochar to adsorb Trichloroacetic acid (TCAA). TCAA is a by-product generated by the reaction between chlorine and natural organic matter (NOM) and is a carcinogen. SEM indicated ZnO nanoparticles on the surface, increased surface area, and strengthened the positive charge. Functional groups on the

plain crayfish biochar included C-H, O-H, and C-O groups. Modified biochar had C=C stretching and calcium carbonate (CaCO_3) and zinc oxide (ZnO) crystal structures. The modified biochar produced at 600°C had the highest adsorption, 17.8 mg/g , due to increased surface area from 63.79 to $236.93 \text{ m}^2/\text{g}$ and surface charge, making ZnO crayfish biochar a potential remediation tool ⁶⁰.

Yan et al., (2018) used slow pyrolysis crayfish modified with ZnO to adsorb As(V) . The modified crayfish biochar had a higher specific surface area than unmodified char, with $134.2 \text{ m}^2/\text{g}$ and $28.3 \text{ m}^2/\text{g}$, respectively, and smaller pore size with 31.3 nm and 120.5 nm , respectively. The higher adsorption capacity from the modified char of 14.87 mg/g was attributed to the ZnO nanoparticles increasing the positive surface charge ⁶¹.

Park et al., (2018) studied the effect of pyrolysis temperature on phosphate adsorption with crayfish biochar. Biochar was produced using slow pyrolysis at 200 , 400 , 600 , and 800°C and held for two hours with char yield decreased from 83.1 wt\% at 200°C to 35.3 wt\% at 800°C and higher temperatures increased mineral content and decreased carbon content. Pyrolysis temperature increased adsorption capacity from 9.5 mg/g at 200°C to 70.9 mg/g at 600°C . The Pseudo second-order model predicted the rate of adsorption, indicating a combination of physisorption and chemisorption. The ion exchange with the char surface and H_2PO_4^- and HPO_4^{2-} , as well as precipitation between calcium and phosphate, were indicated as the main contributors to phosphate adsorption ⁴².

Zhang et al., (2021b) tested the adsorption of tetracycline hydrochloride with ball-milled crayfish biochar. The feedstock was directly placed in the furnace for 2 hours at 800°C . The ball milling increased the surface area from 127.9 to $289.7 \text{ m}^2/\text{g}$, the pore volume from 0.046 to $0.087 \text{ cm}^3/\text{g}$ and decreased the pore size from 3.47 to 2.08 nm . The adsorption capacity also increased from 39.1 to 60.7 mg/g . The ball-milled and regular crayfish char fit the pseudo-second-order rate model

and Freundlich isotherm, indicating adsorption was heterogeneous, multi-layered physisorption with potential chemisorption. Ball milling was a worthwhile additional step since it increased tetracycline hydrochloride removal⁶².

Sun et al., (2021) tested crayfish biochar for lead remediation in water and soil. The crayfish shell was pyrolyzed with a ramp of 15°C /min up to 300, 500, and 700 °C for 2h. Exchangeable lead (Pb) was 27.49% in the acidic soil control, and adding char from 300°C, 500, and 700 °C reduced the exchangeable Pb to 0.54% -9.52%, 1.71%-9.16%, and 0.54% -7.33%, respectively. The Fe-Mn bound fraction of Pb in the acidic soil control was 28.06%, and the addition of char from 300°C, 500, and 700 °C increased the Fe-Mn bound fraction of Pb by 16.38%-17.81%, 11.30%-12.42%, and 10.65%- 12.08%, respectively. Lead removal from water biochar at 300, 500, and 700 °C, had adsorption capacities of 599.70 mg/g, 1114.53 mg/g, and 1166.44 mg/g, respectively, and was fit by the pseudo-second-order kinetic model and the Intraparticle Diffusion model which indicated that intraparticle diffusion occurred in a chemisorption-controlled process. This biochar had the potential for mitigating Pb in soil and water¹³.

Zhang et al., (2019) studied the desorption of lead-loaded crayfish biochar using HCl, HNO₃, H₂SO₄, NaOH, EDTA, and EDTA-2NaCa for desorption. The biochar was produced at a ramp of 15°C/min to 600°C and held for 2h. After adsorption, the char surface area decreased from 31 to 24 m²/g. Zang et al (year) attributed this to the formation of lead crystals on the carbon surface within the biochar pores. The biochar surface area and volume increased after desorption by the acids ranging from 84 m²/g with H₂SO₄ to 220 m²/g with HCl, because of the acid dissolving the CaCO₃ mineral on their surface and resulted in decreased adsorption capacity as compared to EDTA-2NaCa with 0mg/g for H₂SO₄, HNO₃, and HCl, respectively. The EDTA increased the

surface area slightly from 31 to 40 m²/g, while NaOH and EDTA-2NaCa decreased the surface area to 19 m²/g and 5 m²/g, respectively.

A list of recent shrimp biochar studies on plant growth and adsorption is in Table 2.5^{54 64}.

Table 2.5 Shrimp Biochar Studies

Title	Reference
Effect of Shrimp Waste–Derived Biochar and Arbuscular Mycorrhizal Fungus on Yield, Antioxidant Enzymes, and Chemical Composition of Corn Under Salinity Stress	Kazemi et al., 2019 ⁵⁴
Evaluation of Removal Efficiency of Ni(II) and 2,4-DCP Using in Situ Nitrogen-Doped Biochar Modified with Aquatic Animal Waste	Yin et al., 2019 ⁶⁴

Kazemi et al., (2019) studied the effect shrimp waste biochar and arbuscular mycorrhizal fungi (*Funneliformis mosseae*) had on corn growth and soil properties. Pyrolysis occurred at a rate of 15 °C per min and was held for 4 h at 300 °C. The char was added to the soil and compared to adding raw shrimp waste to the soil. The biochar increased phosphorus and nitrogen content in the soil. The addition of shrimp waste killed new plant growth after 20 days, and the addition of shrimp biochar did not kill the new plants. Other benefits of adding biochar to the soil included reduced salt content and electrical conductivity⁵⁴.

Yin et al., (2019) used crab or shrimp combined with aquatic plant (*Trapa natan*) husks as feedstock for biochar for remediating 2,4-Dichlorophenol(2,4-DCP) and nickel. Pyrolysis included a heating rate of 5 °C/min (400 °C, 600 °C, and 800 °C), for 2 h. The removal efficiency of 2,4-DCP decreased with increasing pH as 2,4-DCP is water-soluble, and at high pH, the biochar becomes negatively charged. The adsorption capacity of shrimp with husk biochar was 863.24mg/g, and the crab and husk biochar adsorption capacity of 728.69 mg/g. Adding the crab

and shrimp to the plant feedstock increased the removal of 2,4-DCP. For a nickel, the shrimp with husk biochar had an adsorption capacity of 44.78mg/g, crab with husk was 39.40mg/g. The amino group from this char may increase the removal of 2,4-DCP ⁶⁴.

Multi-metal adsorption studies involving crustacean biochar are reviewed and compared to other adsorbents. ⁵³ A list of multi-metal adsorption studies is provided in Table 6 ^{11 53 65 66 67 68}. Multi-metal adsorption studies are essential models for how adsorbents, such as biochar, could be applied to actual industrial effluents and remediation projects. Sources of metal mixtures include acid mine drainage, energy production, electronics, and paint manufacturing ^{63 69 70}.

Metals vary in size, charge, and reactivity. A mixture of metals may lead to competition for adsorption sites on the char, making the adsorption behavior of the metals differ from those in a single metal system. Chen et al., (2020) used an SP crab biochar modified with magnetite to adsorb a mixture of lead and arsenic. The adsorption results from single metals of Pb (III) and As (III) were compared to metal mixtures ranging from 60, 30, and 10 mg/L for Pb (III) and 20, 10, and 5 mg/L for As(III). Both single metals and the mixtures were fit by the single metal Langmuir isotherm indicating a homogenous monolayer on the surface. The maximum adsorption capacity for Pb (III) was 62.36mg/g, with a K_L of 0.0113. The maximum adsorption capacity of As (III) was 15.84mg/g with a K_L of 0.14889. The metal mixture used 60mg/L of Pb (III) and 30mg/L of As(III). It was fitted again by the Langmuir isotherm with Pb (III) and As(III) having adsorption capacities of 68.35 and 13.03mg/g, and K_L values of 0.0125 and 0.1386, respectively. For Pb (III), the addition of As(III) increased the adsorption capacity by approximately 10%, and the adsorption capacity of As(III) was reduced by 18 wt%. The single metals and mixtures were fitted by the pseudo-second-order kinetic model indicating a combination of physisorption and chemisorption. Individually, Pb (III) and As(III) reached equilibrium within 12 hours and 24 hours

with adsorption capacities of 45.84mg/g and 17.27mg/g and K_2 values of 0.063 and 0.3308, respectively. The metal mixture of Pb (III) and As(III) reached equilibrium at 2 and 24 hours and had adsorption capacities of 25.65 and 16.37mg/g, and adsorption rates of 0.2843 and 0.6673, respectively. The addition of As increased the adsorption capacity and reduced the equilibrium time for Pb. Xiao et al. (2017) used SP crayfish char to adsorb a mixture of lead, arsenic, and copper in a column. Single metal adsorption results for Pb (II) showed maximum adsorption of 190.1mg/g. A metal mixture of Pb (II), Cu(II), and As(III) with initial concentrations of 50mg/L, reached maximum adsorption capacities of 7.5mg/g, 3.57mg/g and 2.03mg/g within one hour. The competition reduced Pb's adsorption, and the relative magnitude of the metals' hydraulic radius, electronegativity, and pKh (negative log of hydrolysis constant) attributed to their order of affinity for adsorption. Moreno et al., (2016) used slow pyrolysis (800°C) cow bone char to adsorb a mixture of Mn, Fe, Cu, and Ni and found it fit the pseudo second order kinetic model for every metal. Adsorption isotherms used plots of C_e/q vs C_e and fit the Langmuir Isotherm model for every metal. Copper had the highest adsorption capacity, 60 mg/g, and the order of adsorption $Cu > Ni > Fe > Mn$ was the reverse of ion size, with copper being the smallest. Adsorption of Cu was attributed to ion exchange with calcium phosphate(hydroxyapatite) and ion size. Ni et al., (2019) used biochar from anaerobically digested wastewater sludge to adsorb a mixture of Pb and Cd. Individual metal isotherms were compared to isotherms from the metal mixture. The highest adsorption capacities for Pb and Cd were approximately 0.6 mmol/g and 0.27 mmol/g, respectively. The addition of Pb reduced the adsorption capacity of Cd, and the metal mix was fit by the Competitive Langmuir Isotherm model, which also indicated metal competition attributed Pb's higher adsorption was attributed to Pb's higher electronegativity, and smaller hydrated radius and pKh than Cd.

Several single metal studies involving carbon sorbents were also reviewed for background on adsorption capacity. Rusova et al., (2018) used coal-based activated carbon to adsorb a mixture of Cu(II), Fe(II), Fe(III), and Mo(IV) and found that the maximum capacities were 11.3, 8.8, 16.83, and 7.17 mg/g respectively and occurred within the optimal pH of 8-8.5 for Cu(II), 6-6.5 for Fe(III), 5-5.5 for Fe(II), 7-8 for Mo(IV) ⁶⁶. A flow Fe concentration of 10 mg/L produced a fluctuating adsorption pattern that was not present with 250 mg/L of Fe. They attributed the fluctuation in adsorption to the fluctuation in the concentrations of the iron ions in the solution phase and the sorbate phase, resulting in a change in the number of carboxyl groups in the carbon structure. Runtti et al., (2014) used commercial activated carbon as a reference to carbon residue from biomass gasification to adsorb Fe, Cu, and Ni as single metals. The highest adsorption capacities for Fe, Cu, and Ni were 13.9, 2.1, and 2.1 mg/g, respectively. The optimum pH required for maximum adsorption was 4, 5, and 8 for iron, copper, and nickel, respectively. The adsorption data from activated carbon for Fe was fit by the Freundlich isotherm indicating a multi-molecular layer on the carbon surface. In contrast, Cu and Ni were fit by the Langmuir isotherm indicating a mono-molecular layer. All three metals were fit by the pseudo-second-order model, suggesting a mixture of physisorption and chemisorption ⁶⁷.

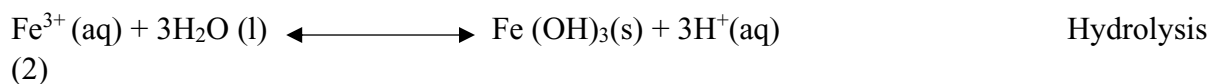
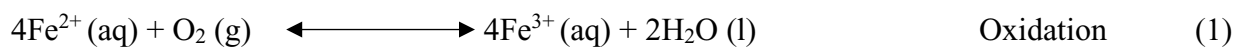
Table 2.6 Metal Adsorption Studies

Feedstock	Metals	Qmax(mg/g)/	Et(h)	Isotherm Fit	Kinetics Fit	Reference
Crab	Pb (III)	68.35	2	Langmuir	PSO *	Chen et al., 2020 ¹¹
	As (III)	13.03	24			
Crab	Mixture			NA	NA	Xiao et al.,2017 ⁵³
	Pb (II)	7.5	1			
	Cu (II)	3.57				
	As (III)	2.03				
Cow bone	Mixture			Langmuir	PSO	Moreno et al., 2016 ⁶⁵
	Cu (II), Fe (II)	60 32	0.3			
Anaerobic wastewater sludge	Pb,	0.6	NA	Competitive Langmuir	NA	Ni et al., 2019 ⁶⁸
	Cd	0.27 mmol/g				
AC-Coal	Mixture			NA	NA	Rusova et al., 2018 ⁶⁶
	Fe, (II),	11.31	2			
	Fe (III)	8.8	2			
	Cu (II)	16.83	2			
AC	Mo (IV)	7.17	4	Fe-Freundlich Cu, Ni - Langmuir	PSO	Runtti et al., 2014 ⁶⁷
	Fe	13.9	2			
	Cu,	5.1				
	Ni	2.1				

AC – activated carbon *Pseudo second-order kinetic model

2.5 Oxidation and Hydrolysis of Metals

Iron sulphates can form solid iron hydroxides through the oxidation of Fe^{2+} followed by hydrolysis ⁷¹.



The oxidation rate increases 100 times with every unit increase of pH and 10 times with every 15°C increase in temperature ⁷¹. As a result, the amount of precipitate formed increases with pH.

The size of the $\text{Fe}(\text{OH})_3$ particles is affected by pH; at low pH, the particles are smaller. Precipitation at low pH begins with the formation of nuclei, approximately 3 to 5nm, and then particles aggregate. The particle size increases between pH 6.0 and pH 10.0 due to base-induced coagulation of the precursor polynuclear species. At pH 8, the particle size may peak at 459nm ⁷¹.

The presence of ferrihydrite solids can increase the oxidation rate, while the presence of sulphate ions, SO_4^{2-} can decrease it. The transformation of iron into more complex species and the conversion between Fe^{2+} and Fe^{3+} can also reduce the oxidation rate ⁷¹.

The hydrolysis of metals can be affected by the concentrations in the solution. Higher concentrations reduce hydrolysis by lowering the pH ⁷². The pH of the solution also affects the form of the metal hydroxides present, with $[\text{Fe}(\text{H}_2\text{O})_6]^{2+}$ being the major form when the pH is less than 8. Copper ion concentrations can vary over two orders of magnitude in the pH range of 6-8. At a pH of 8, the main forms of copper are $\text{Cu}(\text{OH})^+$ and $\text{Cu}(\text{OH})_2$ in solution if the concentrations are below the solubility limit ^{72 73}.

The product solubility values for the copper and iron concentrations used in this study are listed in Table 2.7. Based on a solubility product of 8×10^{-16} and a final pH of 8, the molar solubility for $\text{Fe}(\text{OH})_2$ from Fe150+Cu100 was 1.34×10^{-15} , surpassing the solubility limit⁷⁴. Therefore, precipitates of iron hydroxides will form as a single metal or as a mixture with 150mg/L of iron.

Table 2.7 Solubility Values

Ionic Compound	Ksp ⁷⁴
Cu (OH) ₂	2.2×10^{-20}
Fe (OH) ₂	8.0×10^{-16}
Fe (OH) ₃	2.0×10^{-38}

Chapter 3: Materials and Methodology

3.1 Biochar Production

The biomass for slow (SP) and fast pyrolysis (FP) was sourced from the waste bodies of Snow crab (*Chionoecetes opilio*) from Louisbourg Seafoods Limited, of Louisbourg, Nova Scotia, Canada. The methodology for fast pyrolysis can be found in Hopkins et al., 2022.⁵⁰

For slow pyrolysis, the crab bodies were dried at 100°C for 12 hours to remove water content, then crushed and screened through a 6mm mesh. Dried crab (250g) was placed in a Thermocraft furnace. Oxygen was removed from the sample by a nitrogen flow before and during pyrolysis (1L/min). For slow pyrolysis, the furnace temperature was increased from 6°C/min up to 500°C and held for 3.5h. For fast pyrolysis, the dried crab (5g) was placed into the furnace at 500°C for 5 minutes. Cooled biochar was stored in air-tight containers.

3.2 Thermal Gravimetric Analysis (TGA)

For slow pyrolysis, the TGA was carried out using a TA Instruments Q500. The TGA started under a flow of nitrogen at 50 mL/min, and the temperature increased at a rate of 15 °C/min until 1000 °C. Following the procedure from ASTM E1131-08, the Standard Test Method for Compositional Analysis by Thermogravimetry, the sample moisture content was determined as the mass percent lost from room temperature to 105 °C, and the volatile matter was defined as the mass percent lost from 105 °C to 600 °C. The ash percentage was the total mass remaining. Finally, the decarboxylation of calcium carbonate (CaCO_3) was determined by subtracting the sum of moisture, volatiles, and ash from 100.

3.3 Surface Morphology

Surface Morphology was analyzed using a Scanning Electron Microscopy (SEM), FEI MLA 650 FEG instrument, and Energy Dispersive X-Ray (EDX) spectroscopy coupled to the device and completed in Memorial University of Newfoundland's Micro Analysis lab. SEM was used to analyze the microscopic structure of the CSB. The Transmission Electron Microscope (TEM) images were obtained using a Hitachi HT7700 Transmission Electron Microscope in high contrast mode, equipped with a Lab6 filament in Cape Breton University. Sample preparation included grinding the char and dispersing each sample in approximately 1 mL of ethanol. The samples were transferred to microcentrifuge tubes and sonicated for 10 – 15 mins, and then 1 μ L was placed onto the surface of a 200-mesh copper grid. The samples were left to air dry before analysis.

3.4 Brunauer-Emmett-Teller (BET) Surface Analysis

Brunauer-Emmett-Teller (BET) surface analysis was conducted with a Micromeritics ASAP 2020 Surface Area and Porosity Analyzer at Cape Breton University.

3.5 Elemental Analysis

Elemental analysis was obtained using a Perkin Elmer 2400 Series II CHNS analyzer.

3.6 Fourier-Transform Infrared Spectroscopy (FTIR)

Infrared analysis was performed on a Thermo Nicolet 6700 FT-IR Spectrometer (64 scans, 4cm resolution) at Cape Breton University. Sample preparation consisted of making potassium bromide pellet(s) with a Carver Hydraulic Press and biochar as the analyte.

3.7 Solid State Nuclear Magnetic Resonance (NMR)

Solid-state NMR was conducted with $^{13}\text{C}(1\text{H})$ CPAS at 20kHz, 298K with an AS HCN(D) probe. The samples were finely ground and analyzed for 24 hours at the Memorial University of Newfoundland.

3.8 Zeta Potential Analysis

To determine the zeta potential, 0.1 grams of biochar was added to an Erlenmeyer flask with 100 mL of deionized water. Using a calibrated pH meter, the pH is adjusted to the desired value using 0.1 M HCl or 0.1 M NaOH. The mixtures are put on a shaking table for 24 hours to achieve equilibrium. Equilibrium pH is then analyzed before measuring zeta potential on a Malvern Zetasizer Nano ZS at the Memorial University of Newfoundland.

3.9 X-Ray powder Diffraction (XRD)

X-ray powder diffraction (XRD) was used to identify crystalline structures within the biochar. X-ray powder diffraction (XRD) was conducted with a Bruker D8 Advance instrument with a diffractometer with a copper $\text{K}\alpha$ radiation source in the Verschuren Centre. Samples were ground

into a very fine powder before analysis. Samples were scanned from 10-90° with a step size of 0.05° and a step time of 1 second.

3.10 Batch Adsorption Experiments

To analyze the effects on adsorption with crab char, when iron (II) is added to a solution of copper (II) a series of batch adsorption experiments were conducted on iron as a single metal, copper (II) as a single metal, and a mixture of copper and iron. Varied parameters included initial metal concentration, adsorbent dose, initial pH, and temperature, which resulted in the determination of percent removal, and adsorption capacities.

Single metal adsorption was completed by mixing 100ml of the metal solution with 0.5g of crab char in a beaker with a magnetic stirrer. The concentration of iron or copper was analyzed by the AA based on a calibration curve from fresh standard solutions. Standards were made by dilution with pipettes, Erlenmeyer flasks, and nanopore water. The resulting concentrations were used to calculate the adsorption capacity, q_e (mg/g), and the percent removal (%). The equation for calculating the adsorption capacity is below.

$$q_e = \frac{(C_o - C_f) * v}{m} \quad (3)$$

Where: q_e is the adsorption capacity (mg/g)

C_o is the initial concentration of the metal(mg/L)

C_f is the final concentration of the metal(mg/L)

v is the volume of the solution(L)

m is the mass of crab char(g)

The equation for percentage (%) removal is shown below.

$$\% \text{ Removal} = \frac{(C_o - C_f)}{C_o} * 100 \quad (4)$$

Where: C_o is the initial concentration of the metal(mg/g)

C_f is the final concentration of the metal(mg/g)

3.11 Dosage Experiments

A 100ml of each metal mixture in a beaker had crab char added at four separate loading rates of 1g/l, 5g/l, 10g/l, and 20g/l for 24 hours and then were gravity filtered with Whatman No. 40 ashless filter paper and analyzed for final metal concentrations by the AA.

3.12 pH Experiments

Iron as a single metal had a concentration of 100mg/L, and the metal mixture contained 100mg/l of copper and 150mg/L of iron. The solution's initial pH was adjusted to a pH of 2, 4, 5, or 7 using either 0.01 M HCl or 0.01 M NaOH, and 0.5g of char was added to 100ml of solution and stirred for 24 hours. The final pH was recorded, and the samples were gravity filtered with Whatman No. 40 ashless filter paper and analyzed for final metal concentrations by Flame Atomic Adsorption (AA).

3.13 Temperature Experiments

For temperatures of 4, 13, 21, and 40°C +/- 0.3°C, 100ml of the metal solution was stirred in a temperature-controlled refrigerator for 24 hours, and then gravity filtered with Whatman No. 40 ashless filter paper and analyzed for final metal concentrations by the AA. The 40°C experiments used 100ml of metal solution, stirred in a round bottom flask and set up with a condenser to minimize evaporation heated to the required temperature. After 24 hours, the sample was gravity filtered with Whatman No. 40 ashless filter paper and analyzed for final metal concentrations by the AA.

3.14 The Effect of Initial Concentration

Iron and copper, as single metals, had 100ml of increasing initial concentrations (25, 50, 75, and 150mg/l) mixed with 0.5g of crab for 24 hours. As metal mixtures, copper had an initial concentration of 100mg/l and an increasing iron concentration (25, 50, 75, and 150mg/l) mixed with 0.5g of crab for 24 hours. All samples were gravity filtered with Whatman No. 40 ashless filter paper and were analyzed for final metal concentrations by the AA. The concentrations of the metal mixtures.

3.15 Adsorption Kinetics

The kinetic modelling of iron and copper as single metals and copper in the metal mixtures was conducted to compare adsorption rates and surface features of the crab char. Adsorption kinetics was conducted on copper as part of a mixture with iron, where 100ml of the solution was mixed with 0.5g of crab char in a beaker for 10, 30, 60, 120, and 1440 minutes. Samples were gravity filtered with Whatman No. 40 ashless filter paper and were analyzed for final metal concentrations by the AA. The adsorption capacities were calculated for each time frame and used to produce a pseudo-first-order (PFO), a pseudo-second-order (PSO), and an Elovich kinetic model ⁷⁵. The goodness of fit for each model was assessed by calculating the correlation coefficient (R^2) and the residual mean sum of errors (RMSE).

The PFO model is below:

$$qt = q_{max}(1 - e^{-k_1t}) \quad (5)$$

The PSO model is below:

$$qt = \frac{q_{max}^2 k_2 t}{1 + q_{max} k_2 t} \quad (6)$$

The Elovich model is below:

$$qt = \frac{1}{\beta} \ln(\alpha\beta + 1) \quad (7)$$

Where:

qt is the adsorption capacity (mg/g) of the biochar at a given point of time (t)

q_{max} is the equilibrium adsorption capacity (mg/g)

t is the time elapsed in adsorption (h)

k_1 is the PFO adsorption rate constant (h^{-1})

k_2 is the PSO adsorption rate constant ($g/mg \cdot h$)

α is the Elovich initial rate of adsorption ($mg/kg \cdot h$)

β (kg/mg) is the desorption rate constant for the Elovich equation

3.16 Char Wash

The filtered char from the metal mixtures were placed in a beaker with 100ml of nanopore water and mixed for 1.5hr and gravity filtered with No.41

3.17 Percent (%) Difference

Analyzing the kinetic modelling data used the value of percent difference to compare data sets.

This equation is shown below:

$$\%Difference = \frac{(Before\ value - After\ value)}{Average\ of\ before\ and\ after} \times 100\% \quad (8)$$

3.18 X-ray Photoelectron Spectroscopy (XPS)

XPS was used to detect chemical changes on the outer surface of the char. XPS Spectra were recorded on a Kratos Axis Nova instrument with monochromatic Al K α radiation (1486.6 eV, 150 W). Wide scans were collected with 1 eV step size and 160 eV pass energy while high resolution scans were performed with 0.1 eV step size and 20 eV pass energy. Charge neutralization was performed during data acquisition using a co-axial charge neutralizer. Data analysis was performed with Casa XPS software. All Spectra have been corrected to have the aliphatic/aromatic carbon 1s peak at 285.00 eV.

3.19 Iron Precipitation

The post adsorption char from the single metal and mixtures were washed and the solution was analyzed for iron. An average iron concentration was taken from all the runs.

Chapter 4: Results and Discussion

4.1 Slow and Fast Pyrolysis Crab Char

4.1.1 Thermal Gravimetric Analysis (TGA)

The thermal stabilities of fast pyrolysis (FP) and slow pyrolysis (SP) crab char were analyzed by TGA, as seen in Figure 4.1, and the corresponding proximate analysis is in Table 4.1. For all three samples, the first weight loss occurs between 100 and 180°C through vaporizing water, resulting in moisture content of 7.99%, 2.21%, and 3.00% for raw crab, FP char, and SP char, respectively (see Table 4.1). For raw crab, this represents the water within the shell but for char it represents water adsorbed from air¹⁰. With raw crab, the second mass loss occurred between 140 to 380°C due to organics such as chitin, lipids, and proteins being degraded since chitin begins to thermally degrade at 140°C producing volatiles such as methane, carbon monoxide, ammonia, and formic acid⁷⁶. The mass loss in FP and SP char was lower than raw crab within 140 to 380°C as chitin and organics were already degraded during the pyrolysis to 500 °C. Between 290 to 650°C, the rate of mass loss for raw crab decreased while SP and FP char increased as heavier volatile organics were degraded at these temperatures. As a result, the raw crab had the highest volatile content, 37%, followed by SP char, 12.35%, and FP char, 6.69% (see Table 4.1). The lower volatile content in FP char is due to differences in the pyrolysis systems, including sample size and the quenching system. Fast pyrolysis requires approximately 5g of crab spread out in a sample boat. In comparison, slow pyrolysis requires approximately 250g of crab in a cylinder, heated from the surface to the center, so there is a temperature variation in SP char due to limitations by mass and heat transfer with the lower heat ramp. The second factor is the quenching system. FP char is physically separated from the heat source once the crab stops degassing during pyrolysis; with

slow pyrolysis, the char remains inside the pyrolysis unit and cools. The third mass loss for all samples started near 650 °C, which may indicate the beginning of amorphous calcium carbonate converting into calcium oxide through calcination ⁷⁷. At 750°C, the samples were oxidized, and this mass loss represents combustible materials, so all organics are removed, and the remaining mass is ash ⁵⁰.

FP char and SP char had similar ash contents, and both were higher than the raw crab with 58%wt, 57.32%wt, and 32.28%wt, respectively. Pyrolysis concentrates the ash by removing the organics and leaving the minerals behind. Dai et al., (2017) had similar results from slow pyrolysis of crab with a 58% yield and 55% ash (see Table 4.1) ¹⁰. Ash correlates to the mineral content, and in raw crab, the majority is amorphous calcium carbonate, and in crab char, this is calcite (Figures 4.4 and 4.7). A shrimp pyrolysis study comparing fast and slow heating rates with a final temperature of 600°C showed that the ash content did not change with heating rates ⁵¹. The decarboxylation content represents the amount of calcium carbonate, and in raw crab, FP, and SP char, this was 33.77%, 26.65%, and 22.73%, respectively. Decarboxylation occurs at approximately 650 °C when calcium carbonate converts to carbon dioxide. The decarboxylation value indicates calcium carbonate and ash content in a sample. FP crab had a slightly higher decarboxylation and ash content due to less volatile content. Table 4.1 compares various crustacean biochar proximate values.

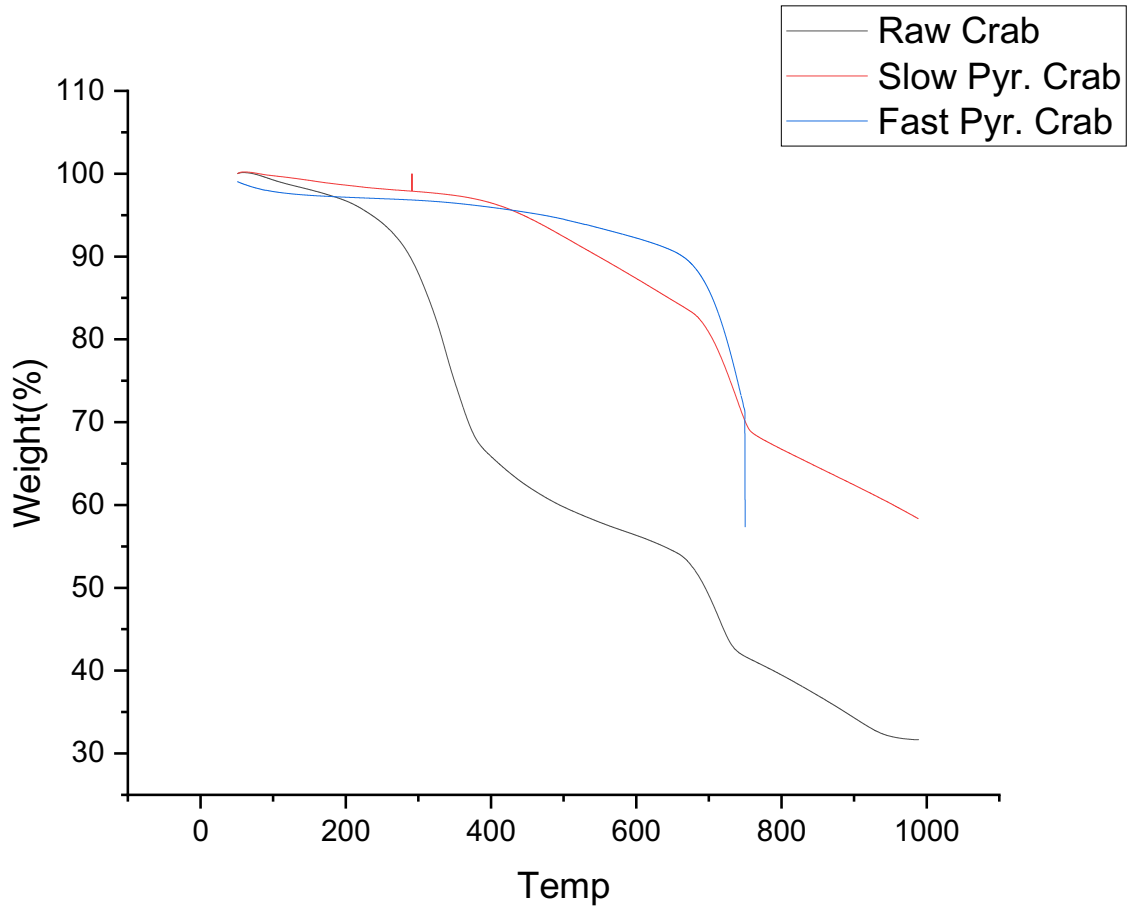


Figure 4.1 TGA data from fast and slow pyrolysis

Table 4.1. Proximate analysis

Sample	(%wt) Yield	(%wt) Moisture	(%wt) Volatiles	(%wt) Ash	(%wt) Decarboxylation
FP Crab	52.7	2.21	6.69	58.00	33.77
SP Crab	54.8	3.00	12.35	57.32	26.65
SP Crab ¹⁰	58	--	--	55	--
Raw Crab	--	7.99	37.00	32.28	22.73
Raw Crab ¹⁰	--	--	--	33.16	--
Raw Shrimp ⁵¹	--	--	--	37.29	--
Shrimp biochar ⁵¹ (No heat ramp)	62	--	--	73.54	--
Shrimp biochar (SP) ⁵¹ (15°C/min)	65	--	--	70.25	--

4.1.2 Surface Morphology

Figure 4.2 contain SEM images of slow pyrolysis (SP) crab char and fast pyrolysis (FP) crab char, both of which contains similar pore structure. The pores are caused by chitin tubes being volatilized when the pyrolysis temperature was above 140°C, as discussed in the results from the TGA. The calcium carbonate remains, as it is thermally stable at 500°C. The SEM images from a shrimp biochar study also showed many surface similarities between a no heat ramp and a low heat ramp pyrolysis shrimp char⁵¹. Surface similarities are also confirmed by the TEM images in Figure 4.3, with both FP and SP crab char containing layers of amorphous calcium carbonates and calcite crystals. In Image A, the FP crab char at 70,000 times magnification and contains a few vertical calcite crystals and amorphous layers of calcium carbonates. Image B shows the SP crab char at 70,000 times magnification containing a rectangular calcite crystal in the center of amorphous layers of calcium carbonates.

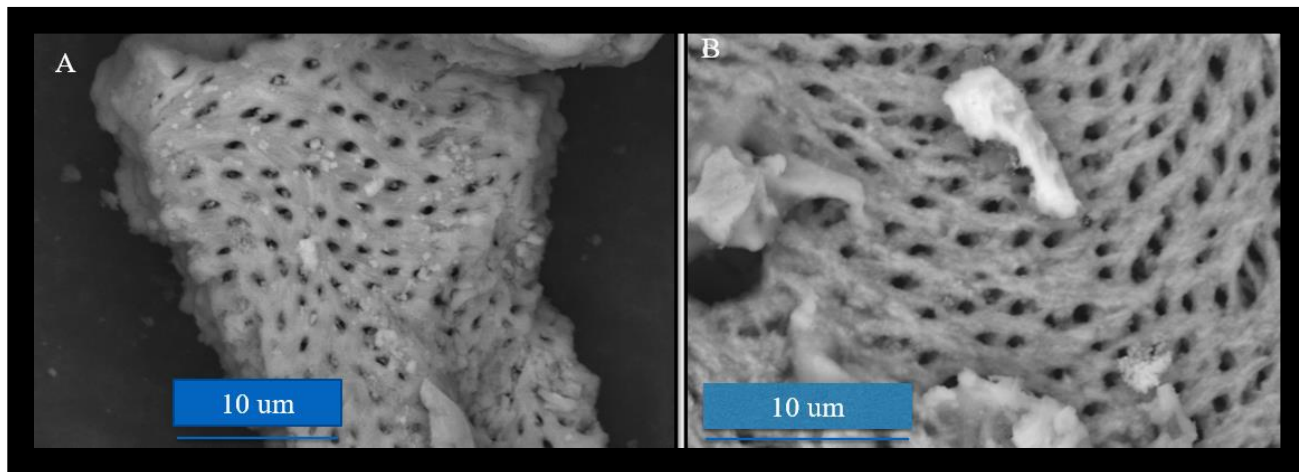


Figure 4.2 SEM Images of A-SP char and B-FP char

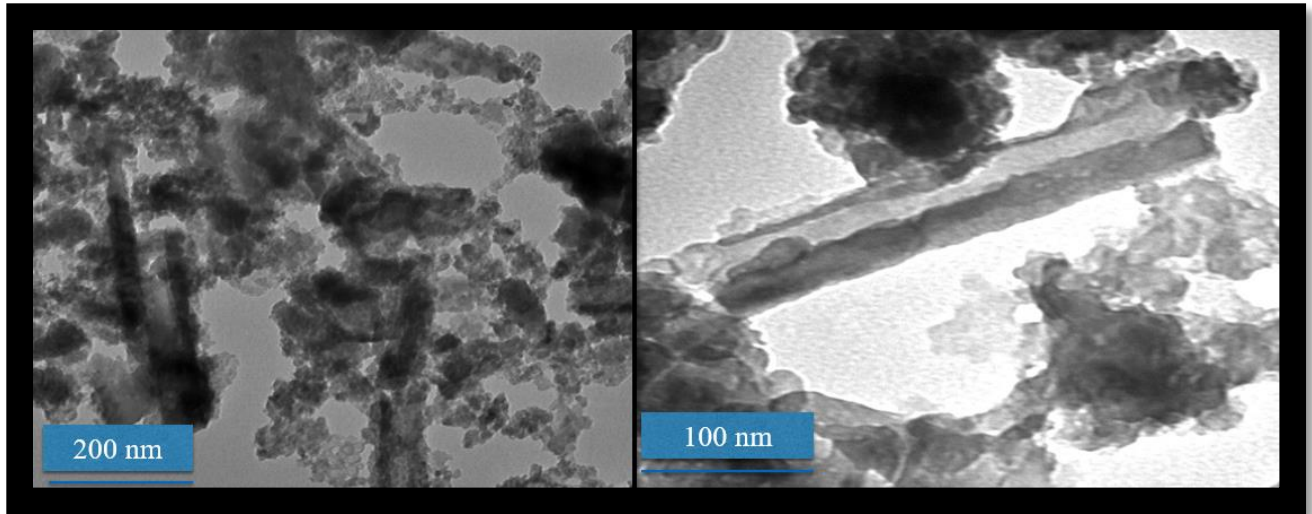


Figure 4.3. TEM images of A-fast pyrolysis char and B-slow pyrolysis char

4.1.3 Surface Area

The surface area for the raw crab biomass, fast pyrolysis (FP)crab, and slow pyrolysis (SP) crab are listed in Table 4.2. The surface area of the chars was higher than the raw crab as the organics were removed. The pore volume also increased with pyrolysis due to volatiles escaping from the material ⁷⁸. The SP char was comparable to another crab study with 14.90 m²/g from slow pyrolysis (500°C) ¹⁰. The surface area of crab char is low compared to other biochar due to the high calcium carbonate concentration of the resulting biochar and relatively low fixed carbon concentration (see Table 4.2). FP char had an average pore volume of 0.07 cm³/g and a pore size of 23.5 nm. SP char had an average pore volume of 0.09 cm³/g and pore size of 21.5 nm. The FP and SP char do not differ in surface area from the BET results, as the values are averages. Another study that compared fast and slow pyrolysis indicated that porosity may be increased with fast pyrolysis due to the very high heating rate ⁷⁸.

Table 4.2 Physical Properties

Sample	BET Surface Area (m ² /g)	Pore Volume (cm ³ /g)	Pore Size (nm)
Raw Crab Shell	9.63	1.7 x 10 ⁻⁵	--
FP Crab ⁵⁰	20.71	0.07	23.5
SP Crab	14.73	0.09	21.5
SP Crab ¹⁰	14.90	0.023	--

4.1.4 Elemental Analysis

The elemental analysis of raw crab, fast pyrolysis (FP) char, and slow pyrolysis (SP) char is provided in Table 4.3. There is little difference between FP and SP crab char elements, with C, H, and N being 3.76 %, 0.56 %, and 0.77% higher in SP char, respectively. The yield and carbon content are affected by the final temperature and the residence time for most biomass. However, crab is less heterogeneous than most other types of biomass, containing large amounts of calcium carbonate, as residence time is less of a factor. A slightly lower carbon content can be attributed to the loss of volatile organics, as illustrated in the weight loss between 200°C and 600°C in the TGA (see Figure 4.1). The difference in feedstock mass resulted in heat and mass transfer limitation for a higher volatile content in the SP char. The ash in the raw crab was composed mainly of amorphous calcium carbonate (CaCO_3) and thermally converted into less anhydrous calcite during pyrolysis, as discussed in the FTIR and XRD results (see sections 4.1.5 and 4.1.8).

Table 4.3. Elemental analysis

Sample	C (wt%)	H (wt%)	N(wt%)	pH
Raw Crab ¹⁰	26.97	3.6	5.15	10.1
FP Crab	18.93	0.68	1.95	11.75
SP Crab	22.69	1.24	2.72	11.0
SP Crab ¹⁰	20.68	0.97	2.38	12.0
Raw Shrimp ⁵¹	22.60	2.91	3.49	--
SP Shrimp	--	--	5.37	--
(15°C/min) ⁵¹				
FP Shrimp	--	--	4.81	--
(No heat ramp) ⁵¹				

4.1.5 Fourier-Transform Infrared Spectroscopy

The results of the FTIR on raw crab biomass, fast pyrolysis char (FP), and slow pyrolysis char (SP) are shown in Figure 4.4.

The effect of pyrolysis on the biomass can be determined by comparing the raw crab to the chars. All of the samples contained a broad peak near 3500 cm^{-1} due to the stretching of hydroxyl (-O-H) groups, representing alcohols and phenols⁵¹, and the intensity is increased in the chars versus the raw crab potentially due to the hygroscopic nature of calcium carbonate⁷⁹ which has an increased content in crustacean chars¹⁰. The results from raw crab show evidence of amide groups, N-H, from chitin that is reduced in both chars as chitin begins to degrade at 140°C ⁷⁶. In raw crab, the spectra show the presence of N- H stretching vibration near 3250 cm^{-1} from the amide group, and a peak near 1550 cm^{-1} are attributed to C=O stretching vibration in the amide I¹⁰. The FP and SP char also likely contain some of N- H as the peak at 3435 cm^{-1} is likely widened by the adjacent peak for N- H stretching near 3250 cm^{-1} . This was also found in SP crab char from 500°C in another study¹⁰. However, the FP and SP chars did not contain the second N-H peak related to C=O stretching vibration in amide I. There are bands near 2960 and 2880 cm^{-1} associated with -CH, -CH₂, and -CH₃ stretching vibrations that remained in all three samples, with higher intensities in the FP char¹⁰. The raw crab and both chars show evidence of containing aromatics, C=C, near 1625 cm^{-1} , and calcium carbonate with increased intensity near 1470 cm^{-1} attributed to carboxylate groups, C=O, and carbonates (CO_3^{2-}) by C-O stretching near 850 cm^{-1} and 760 cm^{-1} , and C-O-C near 1100 cm^{-1} ^{10 51 80}. Both chars have a sharp peak at 1250 cm^{-1} attributed to ester groups, O-R. The main difference between the raw crab and the chars is an increased intensity for the chars near 1490 cm^{-1} , 760 cm^{-1} , and 850 cm^{-1} , which is associated with calcite spectra¹⁰. The biochar peaks are sharper, with increased intensity as the pyrolysis process converts the less thermally

stable, amorphous calcium carbonate in the raw crab into calcite which has a rhombohedral morphology with a trigonal crystal system^{80 81}. FP char has a sharper peak at 1470 cm⁻¹ representing carbonyl, C=O. SP char has a slightly, higher intensity at 850 cm⁻¹, representing carbonates (CO₃²⁻) by C-O stretching. Several studies have identified calcite in crustacean biochar^{10 50 51}. The TEM images also show potential calcite crystals in both FP and SP chars and amorphous calcium carbonate. The raw crab contained more intensity from the amide groups, while these chars' contained calcite. FP and SP char have similar functionalities in this FTIR region including carbonyls and esters, and this similarity is also confirmed by the XRD results (See Figure 4.7).

Below 850 cm⁻¹, in the fingerprint region, FP char has three identifiable areas that differ from SP char, including a very narrow peak near 630 cm⁻¹ and between 500 to 625 cm⁻¹, there is one wide peak for SP char while FP char has two peaks, near 593.5 cm⁻¹ and a slightly higher intense peak near 531 cm⁻¹. FP char also has increased intensity near 510 cm⁻¹ with a very narrow band adjacent to an intense peak near 490 cm⁻¹.

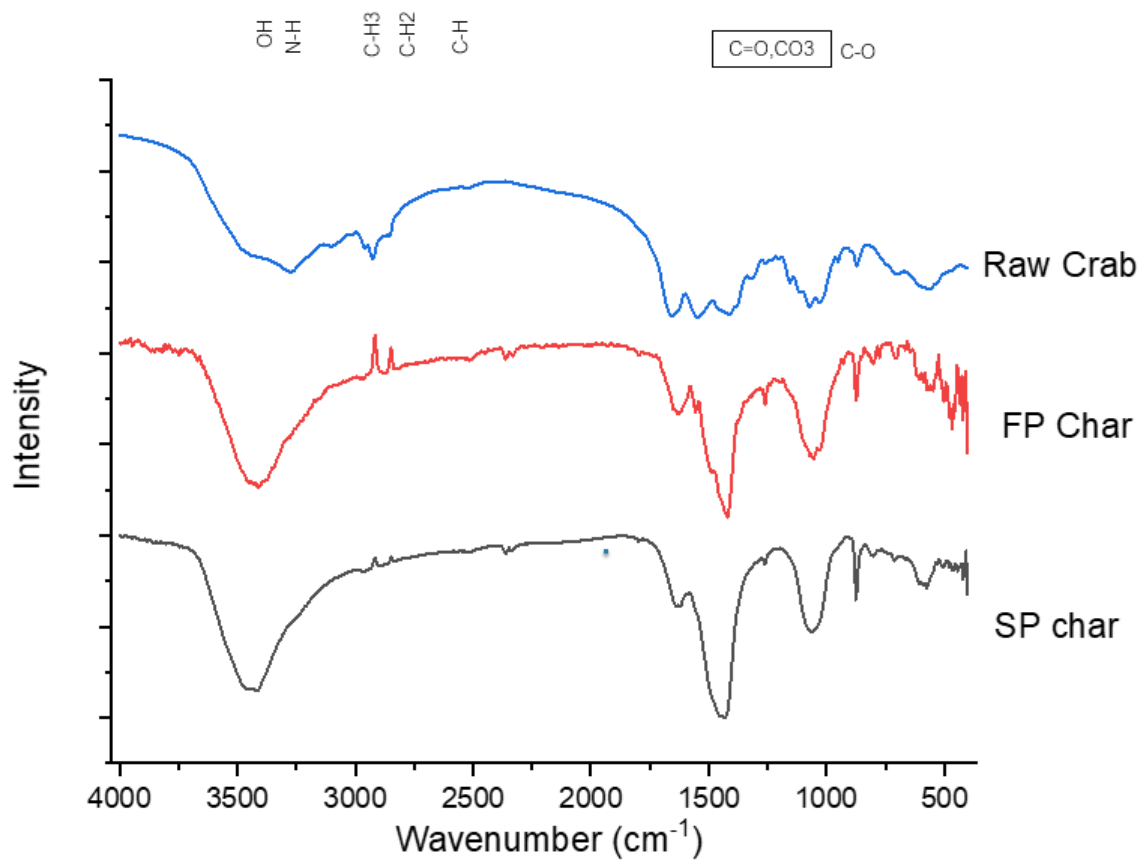


Figure 4.4. FTIR spectra comparing slow and fast pyrolysis crab char

4.1.6 Solid-State Nuclear Magnetic Resonance (NMR)

The solid-state NMR spectra for the fast (FP) and slow (SP) pyrolysis crab char are provided in Figure 4.5. The biochars are similar, containing aromatics (90-165ppm)⁷⁸, alkyl groups (6-90ppm)⁷⁸, and carbonyls (165-210nm)⁷⁸, and this is consistent with the FTIR results (see Figure 4.4), showing bands near 2960 and 2880 cm⁻¹, associated with -CH, -CH₂, and -CH₃ stretching vibrations with increased intensity from FP char and by C-O stretching near 1490 cm⁻¹, 850 cm⁻¹ and 760 cm⁻¹, associated with carbonates (CO₃²⁻)^{10 51 80}. The largest peaks at approximately 124-142ppm can be assigned to an aromatic C=C with SP char having a higher intensity^{25 82}. The second-largest peaks are assigned to alkyl groups with SP char at approximately 23ppm and FP char at 30ppm. The third-largest peaks are located at approximately 72 and 77ppm for SP char and at 77ppm for FP char, which are alkyls. There are likely different alkyl chains and alkyl functional groups present in the two chars. The peaks at 174ppm and 168ppm are consistent with a carbonyl carbon which is expected considering the composition of crab char, both fast and slow are largely calcium carbonate⁷⁸. In comparison to the slow and fast pyrolysis of switchgrass and corn stover, which also have high ash contents, the ¹³C NMR found that slow pyrolysis char contained a higher percentage of C-H, and fast pyrolysis had a higher percentage of C=O, COO, C-OH groups, and a higher percentage of alkyls including methyl (CH₃) groups⁸³.

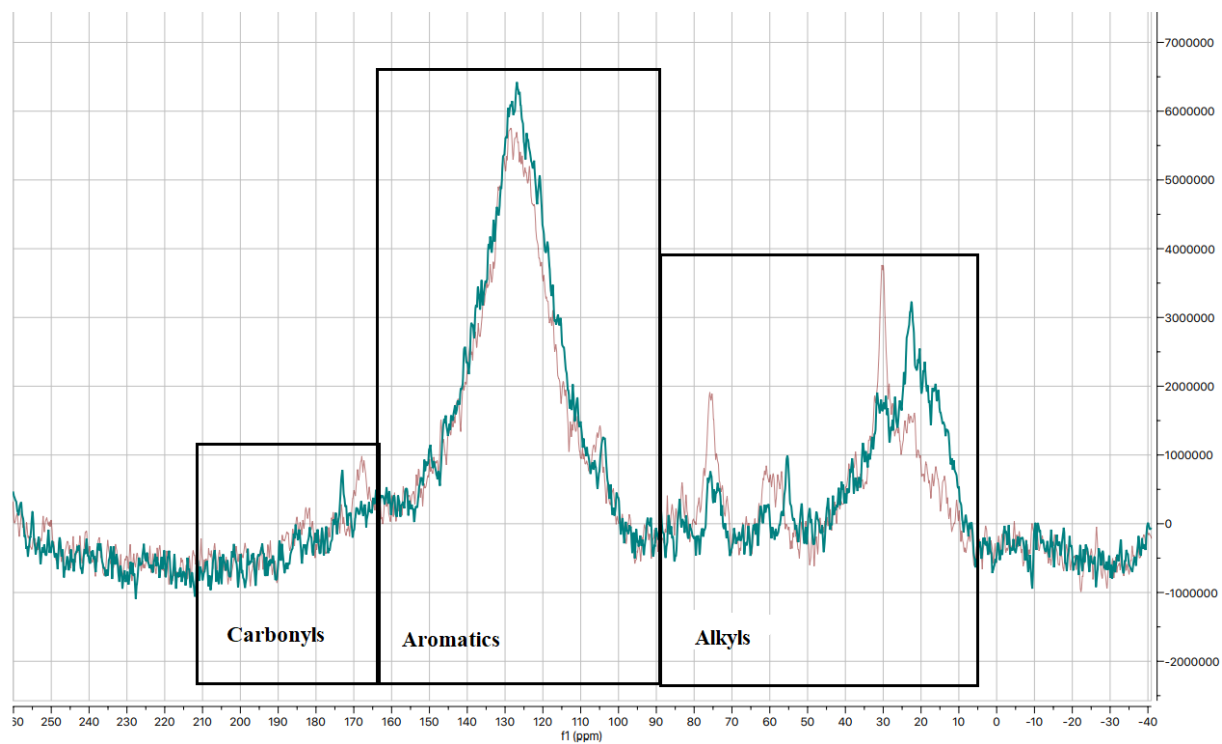


Figure 4.5. Solid-state NMR, $^{13}\text{C}(\text{H})$ spectra comparing fast(pink) and slow(blue) pyrolysis

4.1.7 Zeta Potential Analysis

Figure 4.6 below compares the zeta potential values of slow (SP) and fast (FP) pyrolysis crab biochar. Slow pyrolysis char resulted in zeta potentials from -16.3mV at the equilibrium pH (pHeq) of 8.6 to 17.6mV at a pHeq of 2.85. Comparing the chars at a neutral equilibrium pH (pHeq) for slow pyrolysis and fast pyrolysis, 7.47 and 7.2, the resulting zeta potentials are -14mV and -0.5mV, respectively, suggesting that the slow pyrolysis crab char's surface has a slightly higher, negatively charged surface than fast pyrolysis char. Given that the pH of slow and fast pyrolysis crab char was 11 and 11.75, respectively, the zeta potential would be close to -22mV and negatively charged. The surface charge of the char is important for adsorption since a negative charge would attract positively charged ions and repel negative ions, as demonstrated with cationic dye adsorption having an optimum pH of 7 and anionic dye adsorption having an optimum pH of 4¹⁶. Both SP and FP chars show a trend of increasingly negative zeta potential with increasing pHeq with a zeta potential of -16.3 mV at pHeq 8.6 with slow pyrolysis char and -22mV at pHeq 11.4 with fast pyrolysis char. This indicates a slightly negative surface charge which favors the attraction of positively charged metals. The results from the dye study were similar, with a zero zeta potential at pH 6.7 and zeta potentials of 20 mV at pH 4 and -4 mV above pH of 9¹⁶. One produced slow pyrolysis crayfish at 500°C, and a zero charge occurred at pHeq of 9.72¹³. In this comparison, slow pyrolysis increased the negative charge by -13.5mV as compared to the FP char, resulting in the surface of the SP char having a higher negative charge⁵⁰.

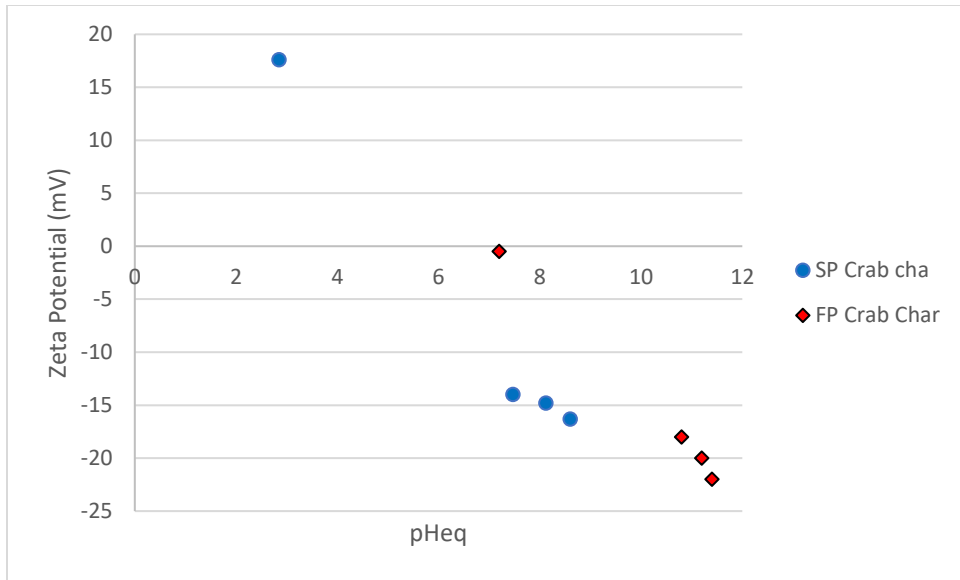


Figure 4.6. Zeta potential of SP and FP crab char

4.1.8 X-Ray powder Diffraction (XRD)

Figure 4.7 compares the diffractogram of raw crab, slow (SP), and fast (FP) pyrolysis crab char. Both SP and FP contained calcium carbonates with similar compositions and intensity. Zhang et al., (2019) also determine that the XRD results were similar between fast and slow pyrolysis of shrimp at 600°C. Only raw crab contained chitin at 20°, and this is because chitin is thermally degraded during pyrolysis. The most intense peak near 29.5 ° is calcite, and it is in the raw crab, as well as the FP and SP char¹⁰. Both FP and SP char have similar peaks at 23°, 36°, 40°, 43°, 46°, 47°, 57°, 62°, 65°, and 66°, which are all attributed to calcium carbonate, which are all attributed to calcium carbonate, labelled as cc CaCO₃, which is consistent with the results from the FTIR⁵¹. Three peaks differ slightly in intensity between the raw crab and the chars at 27-29°, 32-33°, and 45°, labelled as Cc CaCO₃. Based on the previous fast pyrolysis study, these peaks are associated with hydroxyapatite (Ca₅(PO₄)₃(OH))⁵⁰. Biogenic amorphous calcium carbonate can transform by a series of increasing, more stable polymorphs of calcium carbonate to vaterite, aragonite, and finally calcite and involves dehydration and crystallization⁸⁴.

There are several forms of carbonates from crustaceans⁸⁰. A study found little difference between powdered and pyrolyzed blue swimming crab at 550°C, as all the carbonates were magnesium calcite. At 700°C, the magnesium carbonates were converted to calcite and some calcium oxide. The temperature for calcination, converting calcium carbonate into calcium oxide, occurred at 700°C, with blue crab in that study⁸⁰. Since the pyrolysis temperature for this study did not reach 700°C, there is probably no calcium oxide in either the FP or SP crab char.

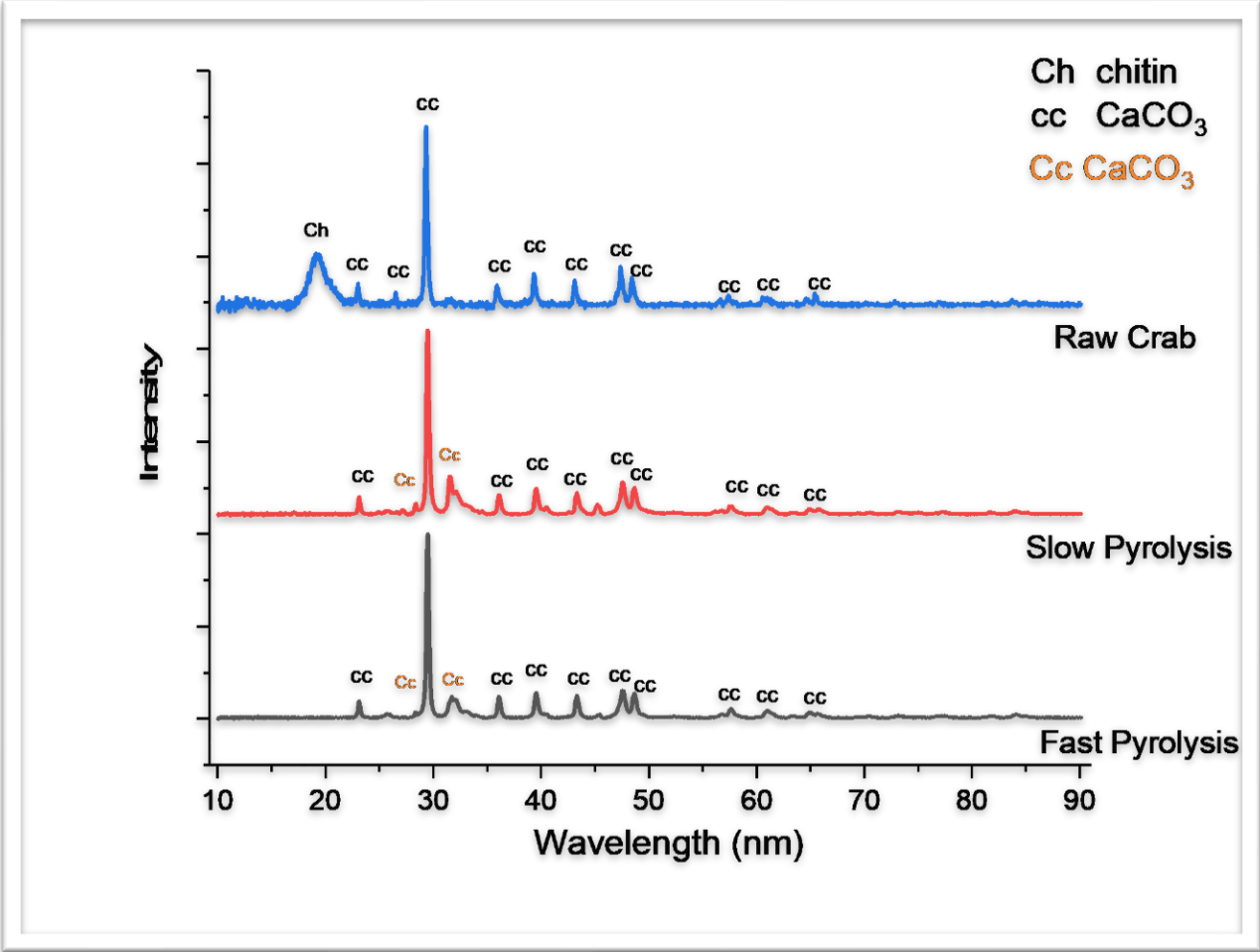


Figure 4.7 XRD comparing slow and fast pyrolysis crab char

4.2 Removal of Iron and Copper from Solution using Fast Pyrolysis Crab Biochar

To analyze the effects on adsorption with crab char, when iron (II) is added to a solution of copper (II), a series of batch adsorption experiments were conducted on iron as a single metal, copper (II) as a single metal, and a mixture of copper and iron. Varied parameters included initial metal concentration, adsorbent dose, initial pH, and temperature, which resulted in the determination of percent removal, and adsorption capacities. In addition, kinetic modelling of iron and copper as single metals and copper in the metal mixtures was conducted to compare adsorption rates and surface features of the crab char.

A previous copper adsorption study used fast pyrolysis on the same crab feedstock and final temperature. To compare this study's copper and iron mixtures to the previous study, parameters such as dosage, initial concentrations, length of time for adsorptions, and the number of experimental replicates were the same. The previous study used ICP analysis which was more accurate than the Flame Atomic Adsorption (AA), and the limitations with AA resulted in the initial concentrations remaining below 200mg/L.

Since iron has several forms based on oxidation and pH, including FeS_2 , an Iron Pourbaix (Eh-pH) diagram was plotted with the software HSC Chemistry 7.1 to determine the potential iron species from this study and to determine the method of iron removal in the batch experiment.

4.2.1 Iron Pourbaix (Eh-pH) Diagrams

Figure 4.8 is the Pourbaix (Eh-pH) diagram for the potential iron species from the batch adsorption completed in this study at 21°C, with 100mg/L $\text{FeSO}_4 \cdot 7\text{H}_2\text{O}$, an initial pH of 4 and a final pH of 8. This diagram helps identify the most probable species of iron present in specific pH and redox conditions during these adsorption experiments. The diagram reflects a solution of $\text{FeSO}_4 \cdot 7\text{H}_2\text{O}$ and does include biochar⁸⁵. Under low pH and slightly reducing conditions, we would expect to see Fe^{2+} as an ion; under a low pH and an oxidizing environment, we would expect to see Fe^{3+} as an ion. Increasing the pH to 8 in the same oxidizing environment would likely result in iron hydroxides based on this diagram.

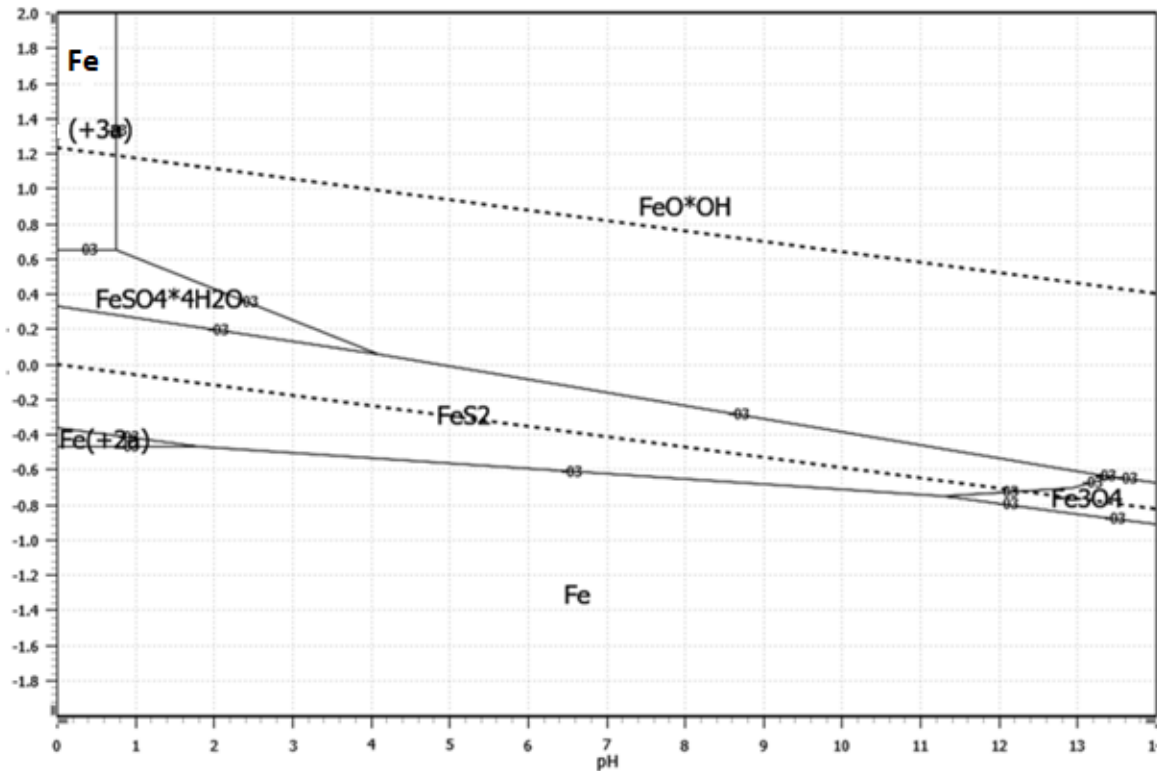


Figure 4.7 Iron pourbaix diagram for 100mg/L $\text{FeSO}_4 \cdot 7\text{H}_2\text{O}$

4.2.2 Initial Concentrations

No isotherm analysis was performed for the iron due to 100% removal regardless of the initial concentration, resulting from the low solubility of iron hydroxides. Figure 4.9 below was used to validate the Flame Atomic Adsorption (AA) analysis of initial copper concentrations from Hopkins et al., 2022 and due to interference between sulphate and the analysis of iron with air-acetylene mixtures, concentrations above 400mg/L were outside of the $\pm 2\text{mg/g}$ error⁸⁶. The burner head required frequent cleaning due to the higher sulphate concentrations during this AA analysis. Therefore, the concentrations for iron and copper were selected below 150mg/L to minimize errors in concentration results, iron precipitation and equipment shutdown.

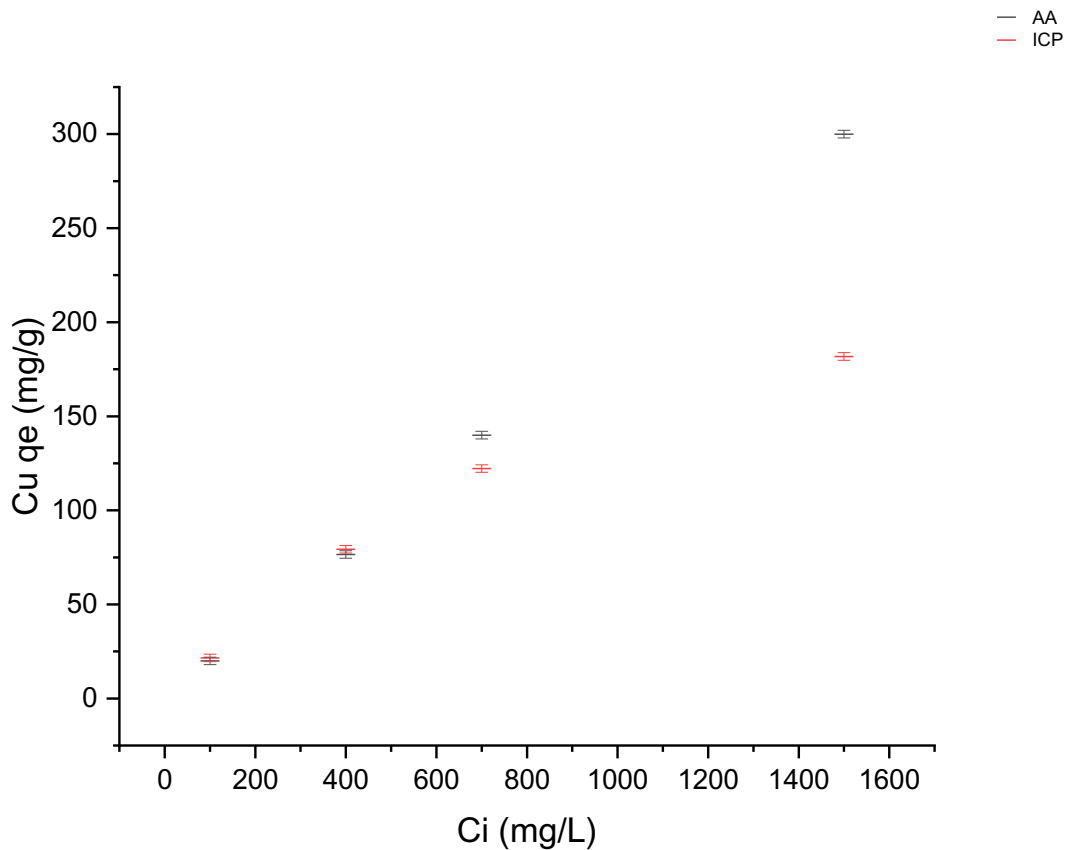


Figure 4.8 Validating AA results for comparison to a previous copper study

4.2.3 Iron as a Single Metal

The Effect of Dosage

In the study by Hopkins et al. (2020), the optimum dosage of biochar was 5g/L for 100mg/L of copper. To verify this dosage for iron, 24-hour batch adsorption experiments using iron sulphate were conducted and plotted in Figure 4.10 below.

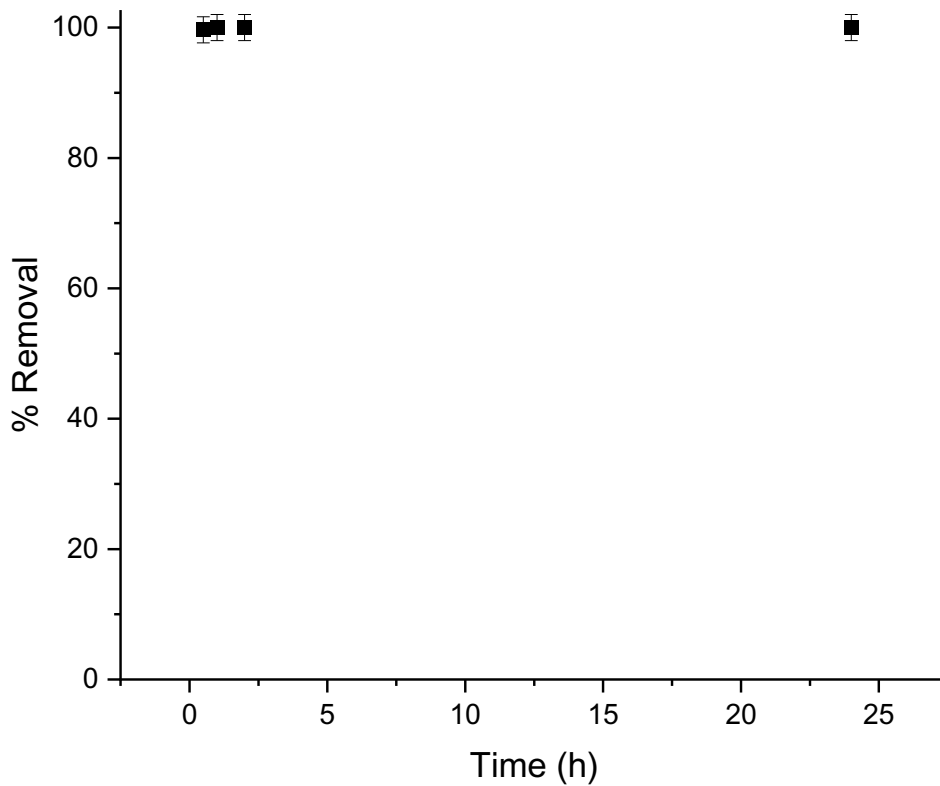


Figure 4.9 Removal of iron with a dosage of 5g/L

It took approximately 30 minutes to remove 91.6% of the iron; however, iron visibly precipitated out of the solution as orange-brown iron hydroxides with a final pH of 8.3. This indicated that 5g/L was a useable dosage for the iron adsorption studies, but an estimate of iron precipitation was needed to calculate the adsorption capacity.

After iron was observed precipitating out of the solution during the first set of experiments, the filtered char was mixed in 100ml of nanopore water for one and half hours, gravity filtered, treated with 1% trace nitric acid, and analyzed for iron through AA. The average estimation of iron precipitate was 8% of the initial iron concentration. However, another study using residual carbon from the gasification of wood chips, with an initial iron concentration of 75mg/L and a final pH of 8, found that approximately 90% of the iron precipitated out of the solution, suggesting iron adsorption on the biochar reduces precipitation ⁶⁷.

The Effect of Initial Fe (II) Concentration

To evaluate the adsorption potential of crab biochar, 24-hour batch experiments were conducted in a single-metal system with initial metal concentrations, Co, ranging from 25mg/L to 150 mg/L and plotted in Figure 4.11 below.

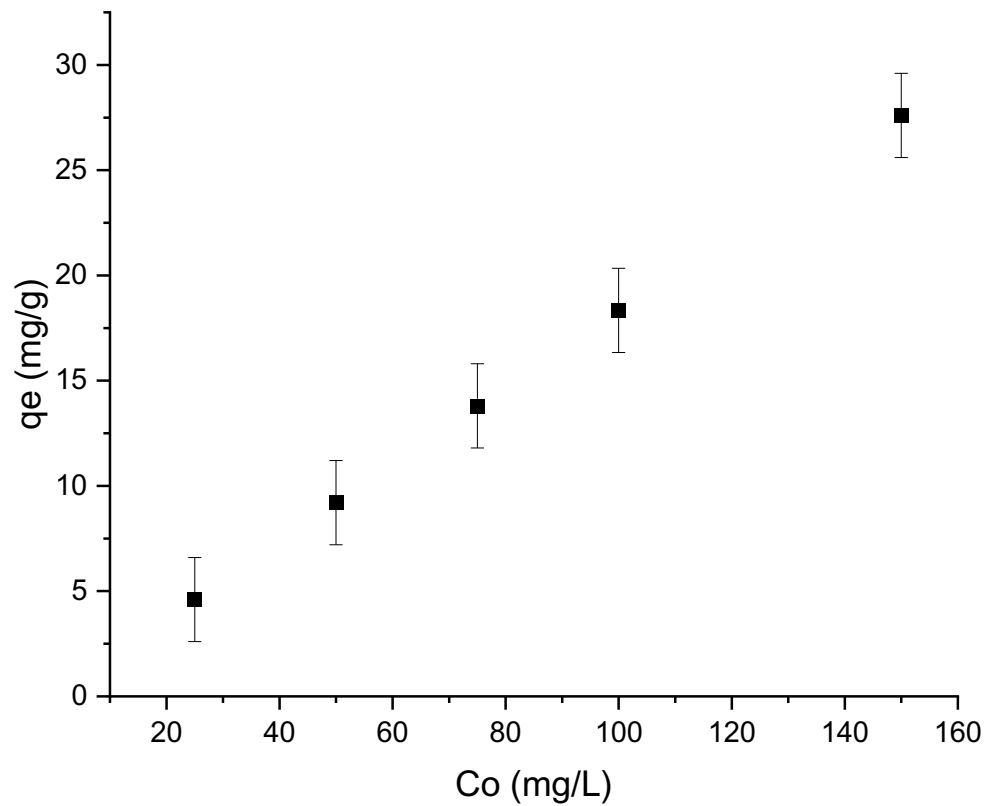


Figure 4.10 Effect of initial concentration on adsorption capacity of iron

The adsorption capacity, q_e , for iron (II) linearly increased with the initial metal concentration, ranging from 4.6mg/g to 27.6mg/g. The adsorption curve does not reach a maximum and flatten, indicating the maximum adsorption capacity was not reached, even after accounting for 8% iron precipitation. As such, no isotherm analysis was done for this system.

The Effect of Initial pH

For this set of experiments, the initial conditions were 100mg/L of iron (II) mixed in 100ml of nanopore water with an initial pH of 3.47, 5 g/L of biochar, and an adsorption time of 24 hours. The results for iron (II) adsorption from water as a function of initial pH were plotted in Figure 4.12.

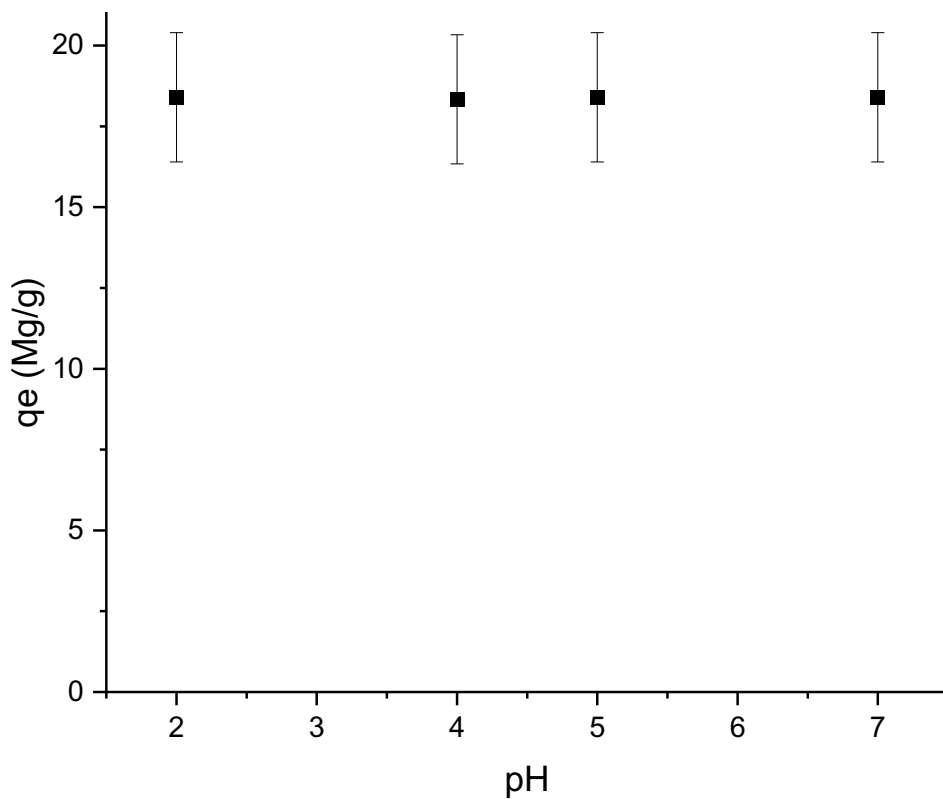


Figure 4.11 Effect of initial pH on iron adsorption

The adsorption capacity ranged from 18.34 to 18.4mg/g, indicating that initial pH had little effect. Iron precipitation was observed at an initial pH of 4 before adding the biochar. The reported pH range for removal of iron by precipitation as sulphides or hydroxides was 5-7, indicating that the adsorption capacity was affected by the increasing pH and the formation of iron hydroxides with low solubilities ⁸⁷. Another iron adsorption study used carbon residue from the gasification of wood chips, and an initial concentration of 75mg/L of iron, determined an optimum adsorption pH of 4 and obtained an adsorption capacity of 16.6mg/g ⁶⁷.

The Effect of Temperature

The experiments were run at four different temperatures (4, 13, 20, and 40°C) for 24 hours, and the results were plotted in Figure 4.13.

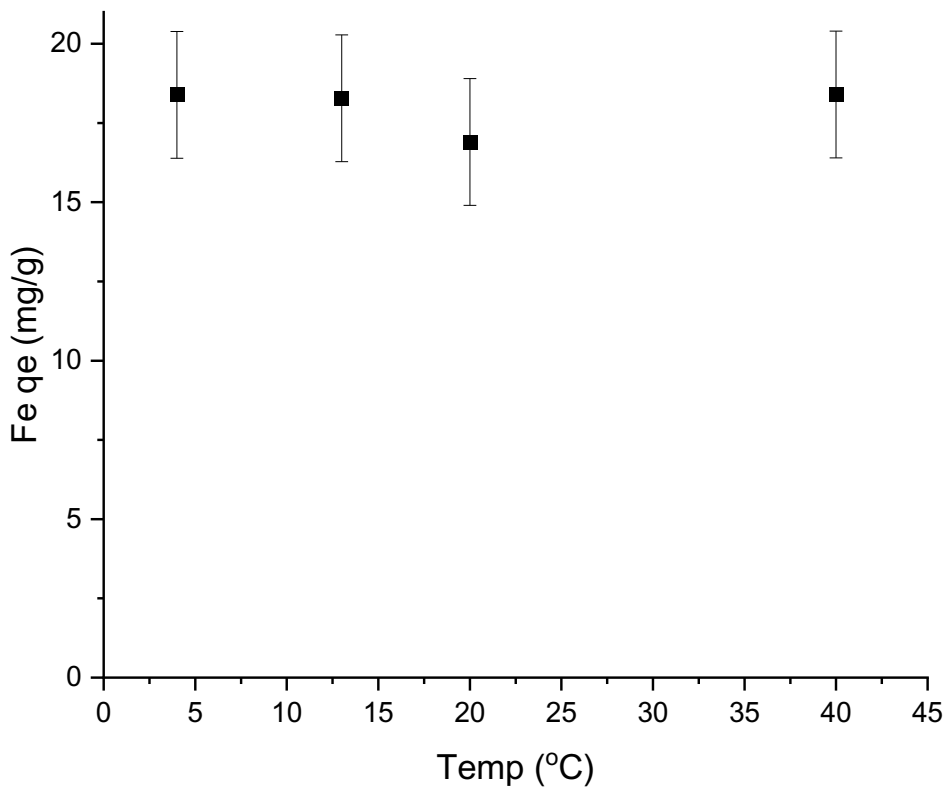


Figure 4.12 Effect of temperature on iron adsorption

The effect of temperature on adsorption was negligible. The adsorption capacity ranged from 16.90 mg/g at 20 °C to 18.4 mg/g at 40°C with an error in the capacity of +/-2mg/g; this indicates temperature impact on adsorption is negligible due to the formation of iron hydroxides with low solubility, given that the final pH was 7.72 and 7.83, for temperatures of 4°C and 40°C, respectively⁵⁰. This suggests that precipitation overrides the effect of temperature change. In comparison, another study used various precipitating agents, including CaO, CaCO₃, and Ca(OH)₂, to remove iron from a zinc concentrate pressure leaching system and found that temperature had little impact on iron removal⁸⁸.

4.2.4 Copper as a Single Metal

The adsorption of copper (II) and iron (II) as single metal solutions were plotted in Figure 4.14 for comparison. Initial concentrations of copper as a single metal ranged from 25mg/L to 150mg/L. In the metal mixtures, copper's concentration remained at 100mg/L; therefore, the values for adsorption capacity are higher in the single metal results because of higher initial concentrations. The adsorption capacity for copper ranged from 4.94 to 29.95mg/g, while iron ranged from 4.6 to 27.6mg/g. Iron and copper show a straight-line increase in adsorption capacity with concentration, indicating the maximum adsorption capacity is not reached within the experimental ranges of this system. It should be noted these initial concentrations were selected at levels high enough to impact receiving water bodies and below solubility limits for the initial pH. The adsorption capacity uncertainty of +/- 2mg/g overlaps the results from the two metals, indicating little difference between iron and copper. In all experiments, 100% of iron was removed with 8% through precipitation due to low solubility with increased pH, while copper removal ranged from 97.96 to 99.84%. As single metals, iron had a higher removal percentage, and copper had a higher adsorption capacity.

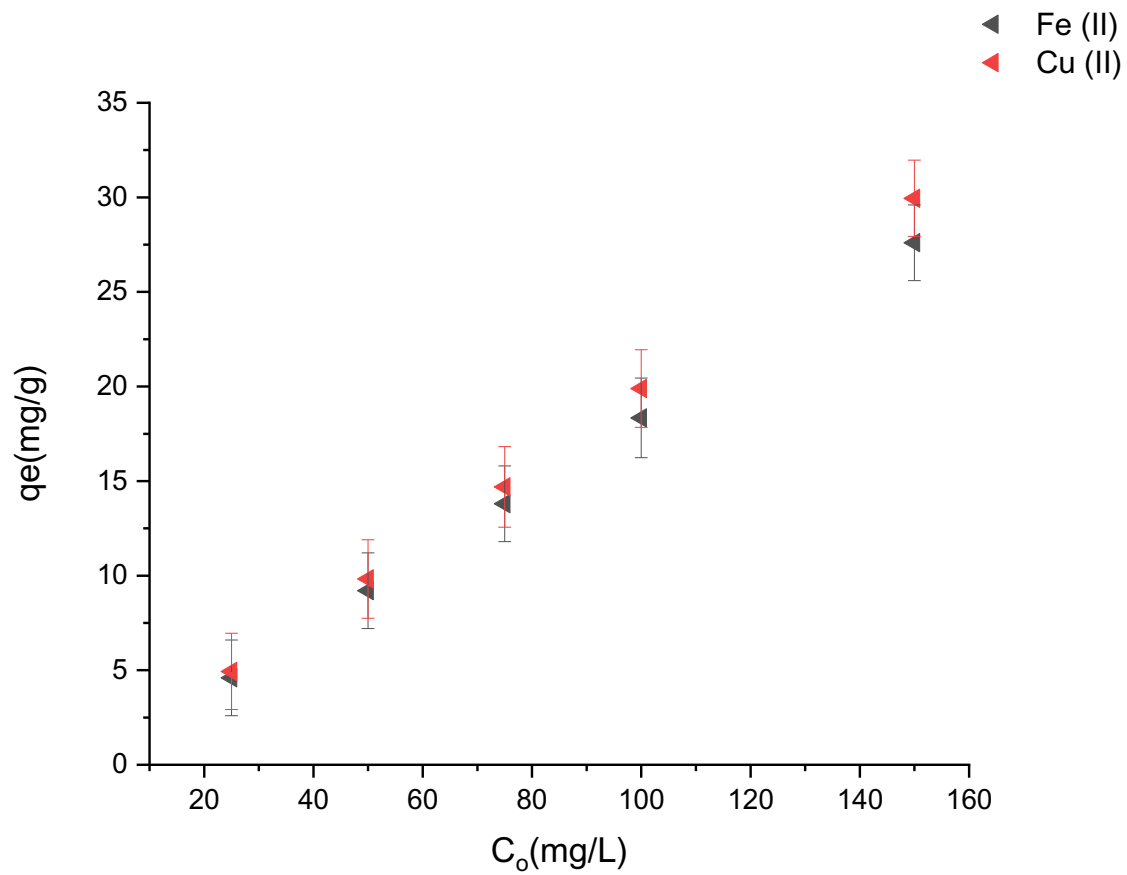


Figure 4.13 Comparing the effect of initial concentration on copper and iron as single metals

4.2.5 Adsorption Kinetics

Iron as a Single Metal

The adsorption capacity for iron over time was plotted in Figure 4.15. An initial concentration of 100mg/L of iron (II) resulted in an adsorption capacity of 18.4mg/g, based on 8% precipitation. Within 10 minutes, 55% of the iron was adsorbed, indicating a very high adsorption rate, and after 1hr, the iron was 100% removed. The previous copper study had 85% of the initial copper concentration adsorbed within two hours, indicating a faster rate of iron removal from the solution due to adsorption and precipitation ⁵⁰.

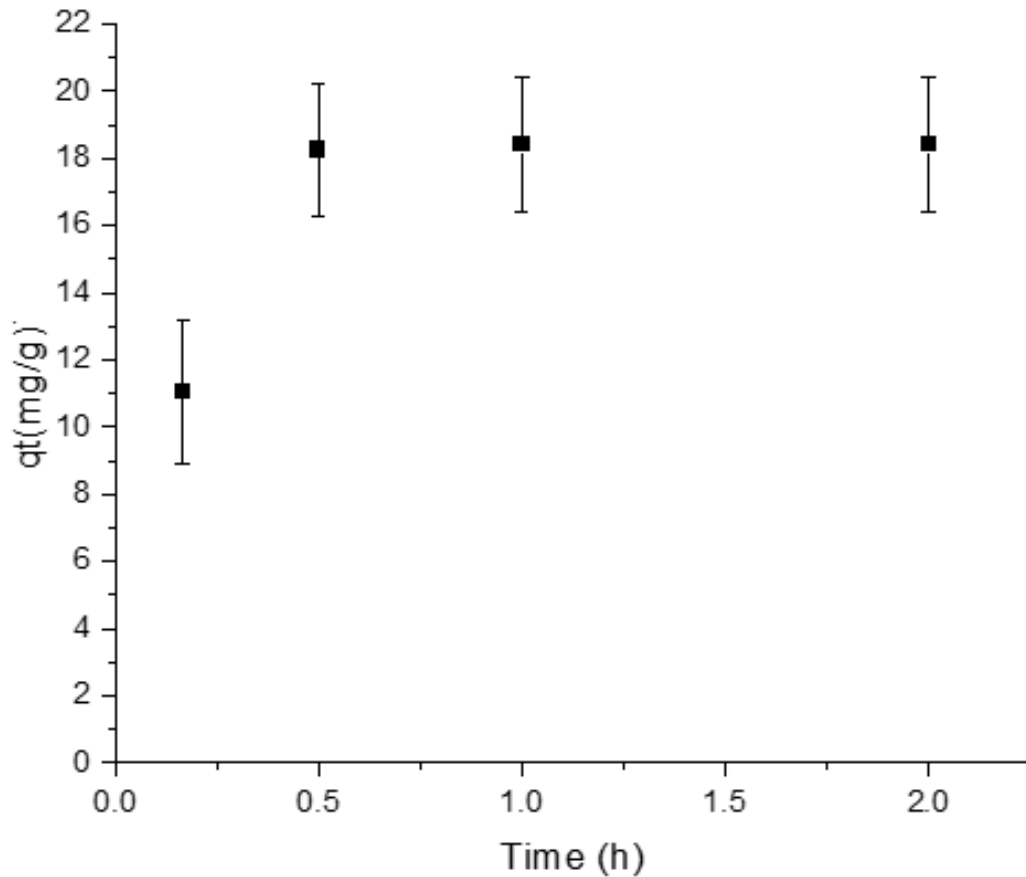


Figure 4.14 Adsorption of iron over time as a single metal

Kinetic modelling was completed with an initial iron(II) concentration of 100mg/L, the same initial copper concentration used for adsorption kinetic calculation in the previous copper study ⁵⁰. The results from the kinetic modelling of iron adsorption with crab char are provided in Figure 4.16, and the corresponding parameters and model fit statistics are in Table 4.4. Further kinetic studies should include a range of initial concentrations.

Table 4.4 Adsorption Kinetic Model Parameters for 100mg/L of iron

Kinetic Model	qmax(mg/g)	k(h ⁻¹)	R ²	RMSE
Pseudo First Order	18.67	5.63	1.00	0.17
Pseudo Second Order	20.51	0.41	0.99	1.14
	A	B	R ²	RMSE
Elovich	1.28x10 ³	0.34	0.93	2.17

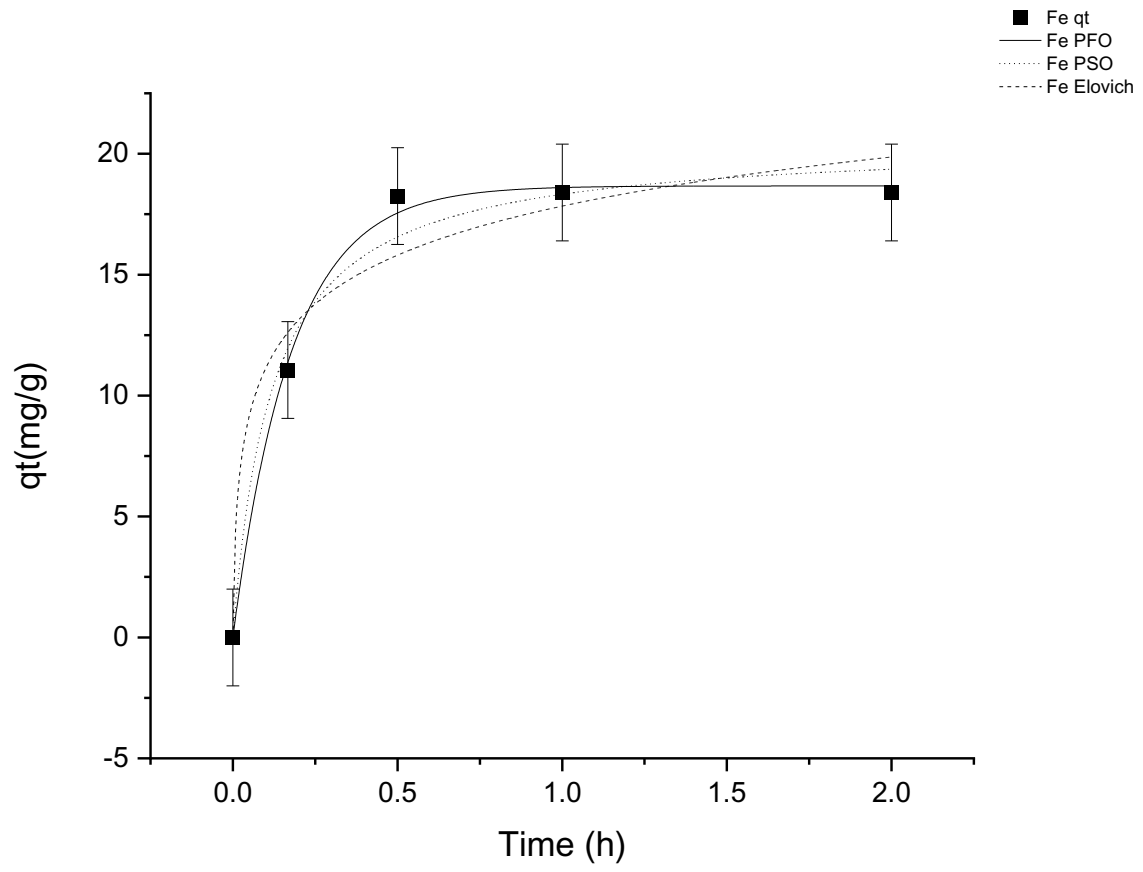


Figure 4.15 Kinetic models for iron adsorption with crab char

The order of the best fit with kinetic models was Pseudo First Order, Pseudo Second Order, and the Elovich Model. The Pseudo First Order model resulted in a maximum adsorption capacity of 18.67mg/g, the lowest value for the Residual Mean Sum of Squares (RMSE), 0.17, and the highest value for the coefficient of determination (R^2), 0.98, indicating the best fit for iron as a single metal. The differences between the adsorption capacities from the Pseudo First Order Model and the experimental data were minor, ranging from 0.2 to 0.7 mg/g with an average difference of -0.019 mg/g. This model's maximum adsorption capacity was only 0.26mg/g higher than the experimental maximum adsorption capacity of 18.40mg/g, supporting the assignment of best fit. The model's adsorption rate was 5.63hr^{-1} . This high initial adsorption rate may have been affected by the increasing solution pH and the formation of iron hydroxides with low solubility.

Single Metal Comparison

Adsorption over time for copper and iron, as single metals, with initial concentrations of 100mg/L and initial pH of 4.0 and 3.4, respectively, were compared in terms of highest adsorption capacity and time to equilibrium. The adsorption of copper and iron over time as single metals was plotted in Figure 4.17. Iron has a faster initial rate of adsorption and a lower maximum adsorption capacity than copper due to increased pH and the formation of iron hydroxides with low solubility. The adsorption capacity for copper at 0.5hr was less than iron's adsorption capacity at 10 minutes, and copper reached equilibrium at two hours, while iron reached equilibrium at 30 minutes. The maximum adsorption for copper was higher than iron, with 20mg/g and 18.4mg/g, respectively.

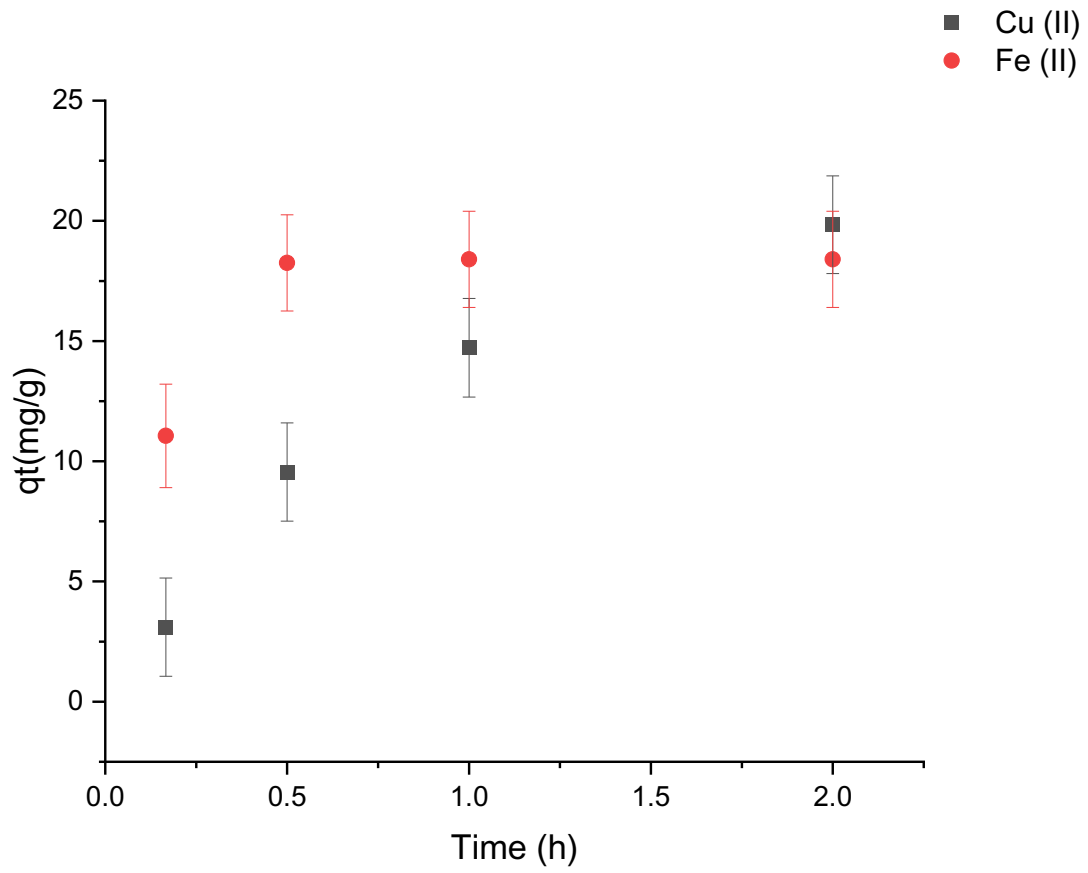


Figure 4.16 Comparing the adsorption of copper and iron as single metals over time

4.2.6 Copper and Iron Mixtures

Initial concentrations of copper as a single metal ranged from 25mg/L to 150mg/L. In the metal mixtures, copper's concentration remained at 100mg/L, so the maximum potential adsorption capacity from the single metal was higher than the metal mixtures for numerical comparison. The four metal mixtures include 100mg/L of copper (II) with 25mg/L of iron (II) (Cu+Fe25), and 100mg/L of copper (II) with 50mg/L of iron (II), (Cu+Fe50), and 100mg/L of copper (II) with 75mg/L of iron (II), (Cu+Fe75), and 100mg/L of copper (II) with 150mg/L of iron (II) (Cu+Fe150). The metal mixtures have an approximate initial and final pH of 4 and 8. The effect of char dosage, initial pH, and temperature on the adsorption capacity of copper and iron in the mixtures are presented below. Kinetic adsorption modelling was completed for the adsorption capacity of copper with the Pseudo First Order, Pseudo Second Order, and Elovich models.

The Effect of Dosage

The results of the dosage experiments for the metal mixtures of copper and iron are plotted in Figures 4.18 to 4.20. Copper had 100% removal with every dosage, and iron removal ranged from 79% with 1g/L to 96% with 5g/L, with no clear trend between iron removal and dosage value. The results from copper and iron as single metals (see Figure 4.17) also showed that copper had a higher adsorption capacity than iron due to increased pH and the formation of iron hydroxides with low solubility. The addition of iron to the copper solution did not affect the removal of copper with dosage. The optimal char dosage for the mixture of 100mg/L of copper with 25mg/L of iron was 5g/L since it had the highest removal for copper and iron. The dosage did not significantly affect the removal of copper, with approximately 100% removal from every dosage.

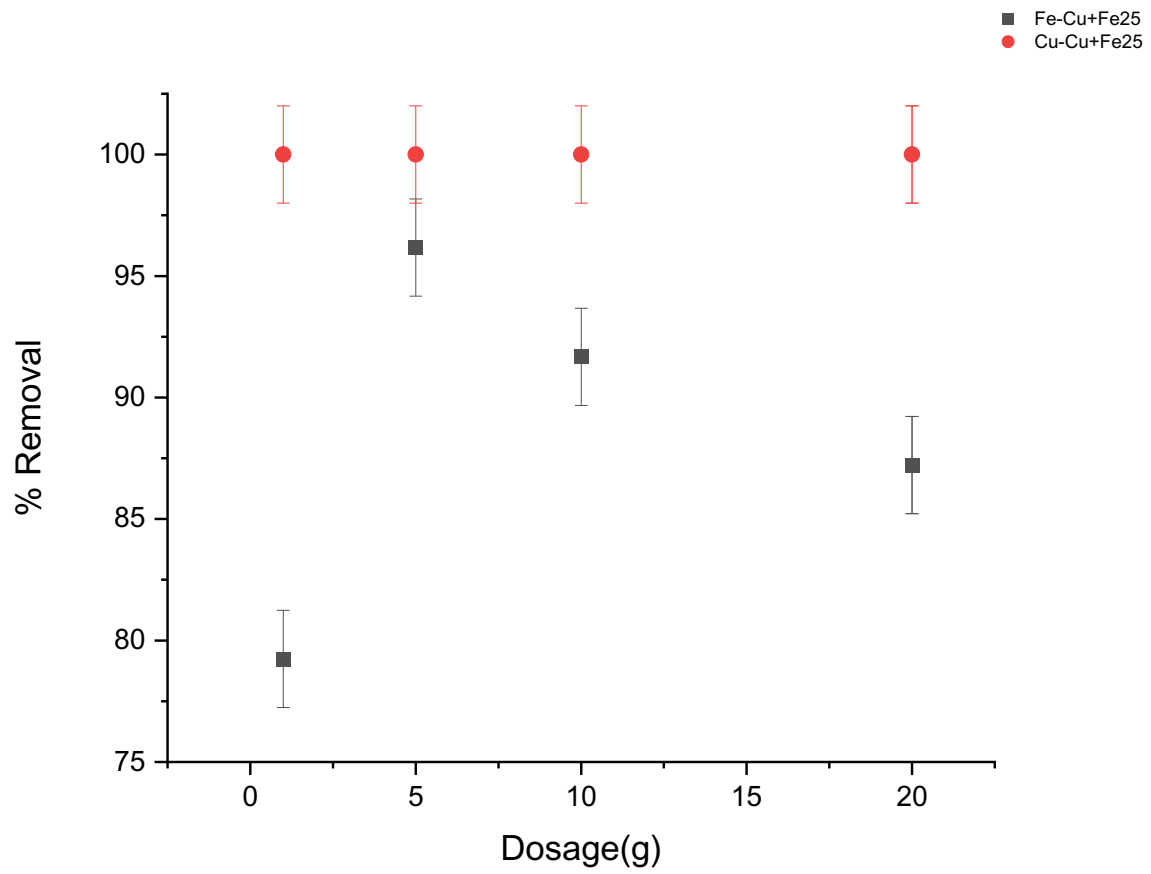


Figure 4.17 Removal of iron and copper from a mixture (25mg/L of iron + 100mg/L of copper) with increasing dosage

Dosage did not affect the removal of copper mixed with 50mg/L of iron, with approximately 100% removal for every dosage. The iron results likely varied due to the formation of hydroxides with low solubility, as different dosages caused variations in pH.

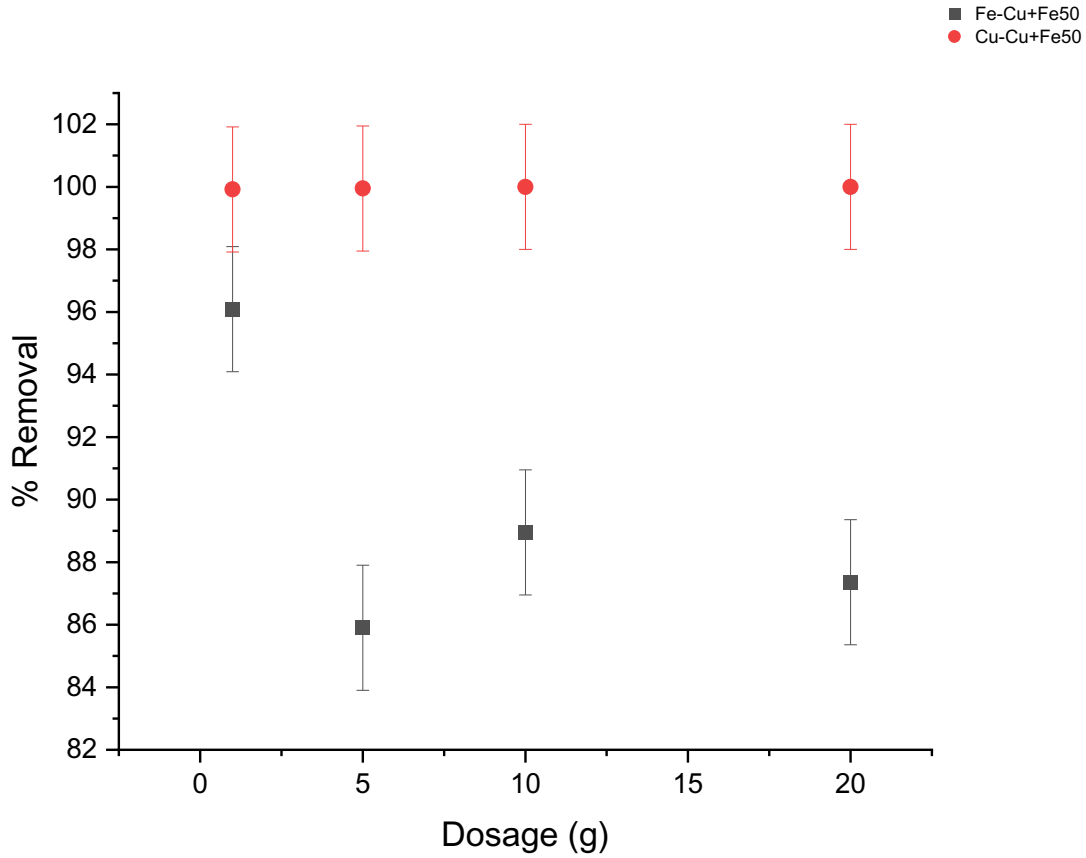


Figure 4.18 Removal of iron and copper from a mixture (50mg/L of iron + 100mg/L of copper) with increasing dosage

The highest iron removal out of all the metal mixtures was approximately 96%, with the combination of copper and 150mg/L of iron. Copper had 100% removal, and iron and copper were not significantly affected by the dosage, given that every data point was within the error bars. The consistently high removal was due to the solubility limit of $\text{Fe}(\text{OH})_2$ being surpassed at 150mg/L of iron ⁷⁴.

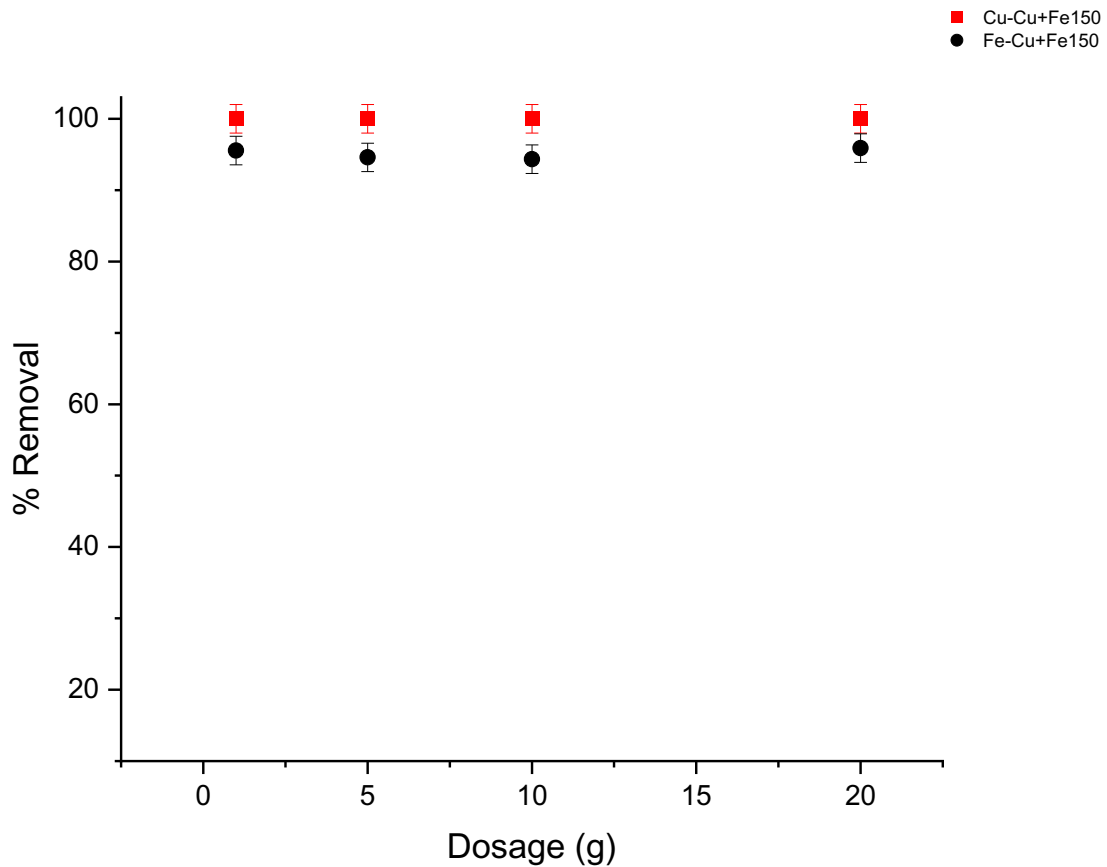


Figure 4.19 Removal of iron and copper from a mixture (150mg/L of iron + 100mg/L of copper) with increasing dosage

The Effect of Initial pH

The effect of initial pH on copper and iron removal from the metal mixture of 100mg/L of copper and 150mg/L of iron was plotted in Figure 4.21. The initial pH did not affect the removal of copper or iron, and there was approximately 100% removal for both metals with every pH. The single metal results of copper and iron also showed no effect from varying initial pH⁵⁰. The crab biochar increased the solution pH to approximately 8 after every batch experiment. The initial pH also had no effect on the adsorption of copper or iron as single metals.

The increasing pH resulted in the formation of iron hydroxides with low solubility. In addition, the formation of iron hydroxides caused the metal mixture to have a lower final pH of 8 than the previous copper adsorption study, which was 10⁵⁰.

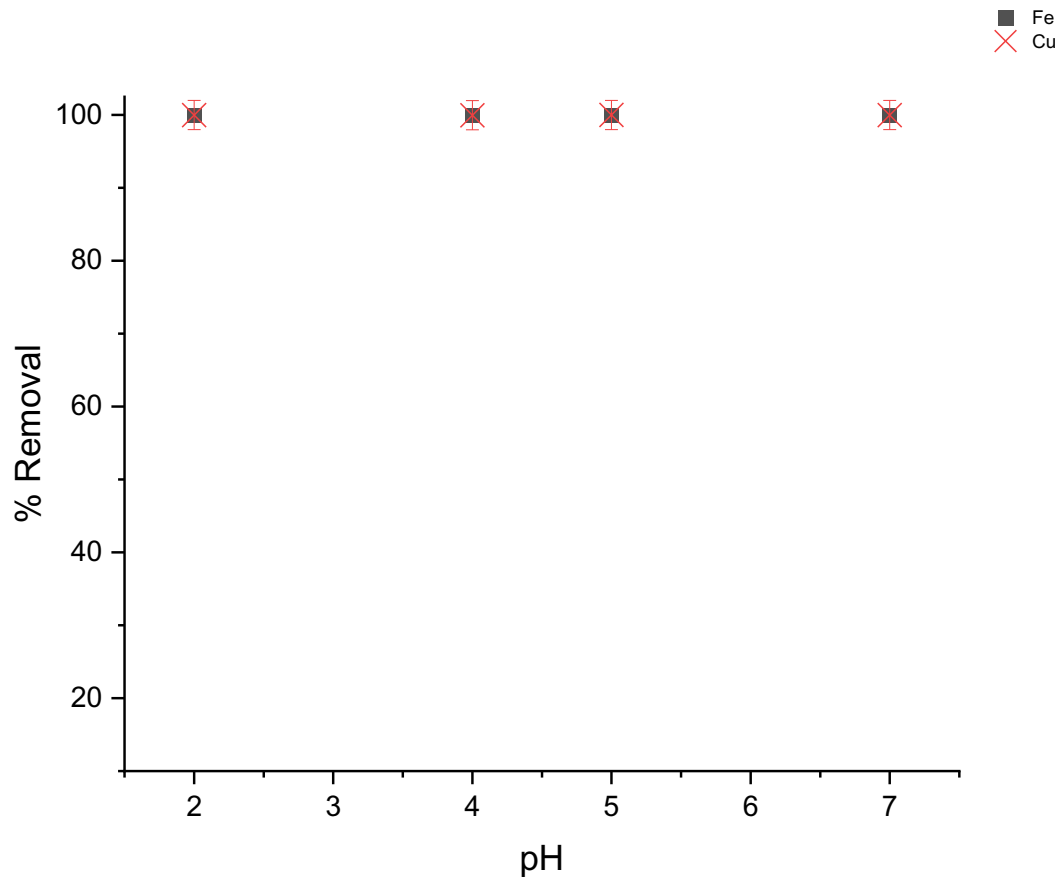


Figure 4.20 Effect of initial pH on the removal of iron and copper from a mixture (150mg/L of iron + 100mg/L of copper)

The Effect of Temperature

The effect of temperature on removing iron and copper from a mixture of 75mg/L of iron and 100mg/L of copper was plotted in Figure 4.22. Copper and iron have approximately 100% removal with every temperature, indicating temperature has little effect on the adsorption of crab biochar. Iron, as a single metal, also showed minimal change from temperature variation (see Figure 4.13).

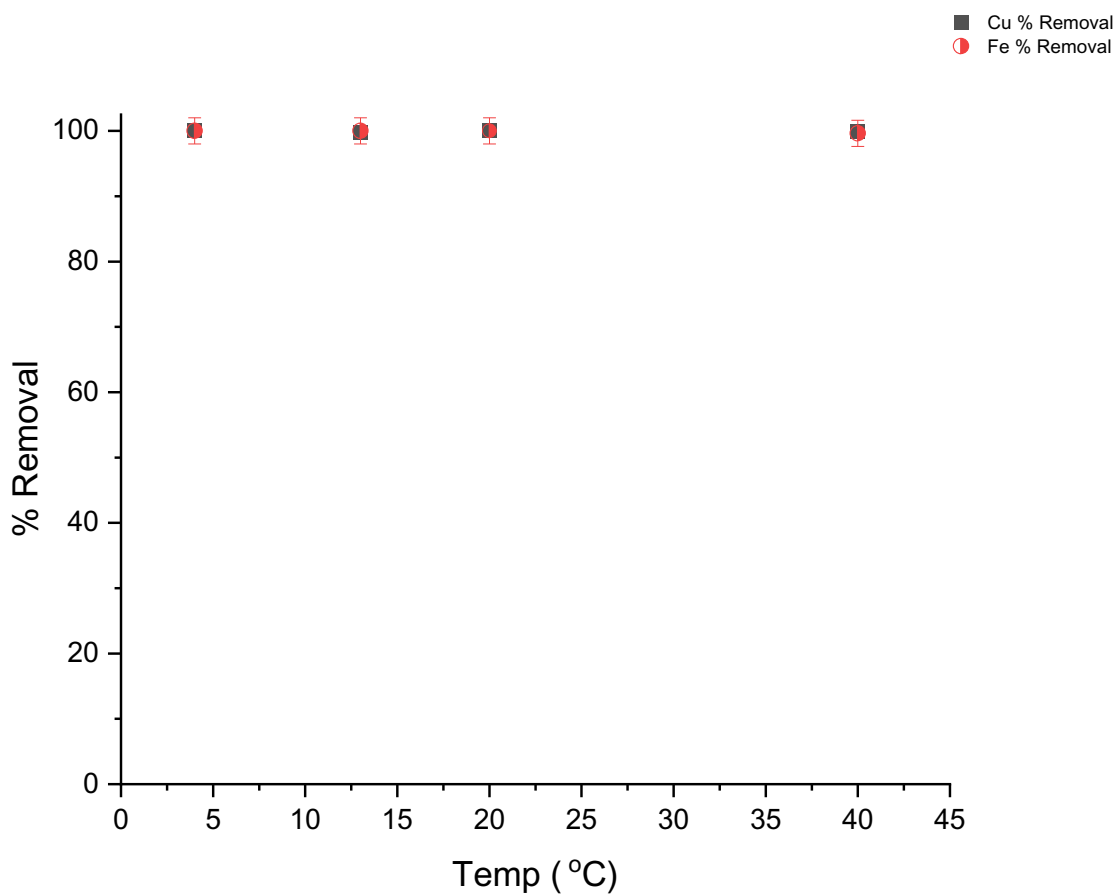


Figure 4.21 Effect of temperature on the removal of iron and copper from a mixture (75mg/L of iron + 100mg/L of copper)

Adsorption Kinetics

The adsorption capacity of copper over time is plotted in Figure 4.23. Copper as a single metal solution is compared to the copper adsorption capacity from the four metal mixtures to determine if iron affects the adsorption of copper.

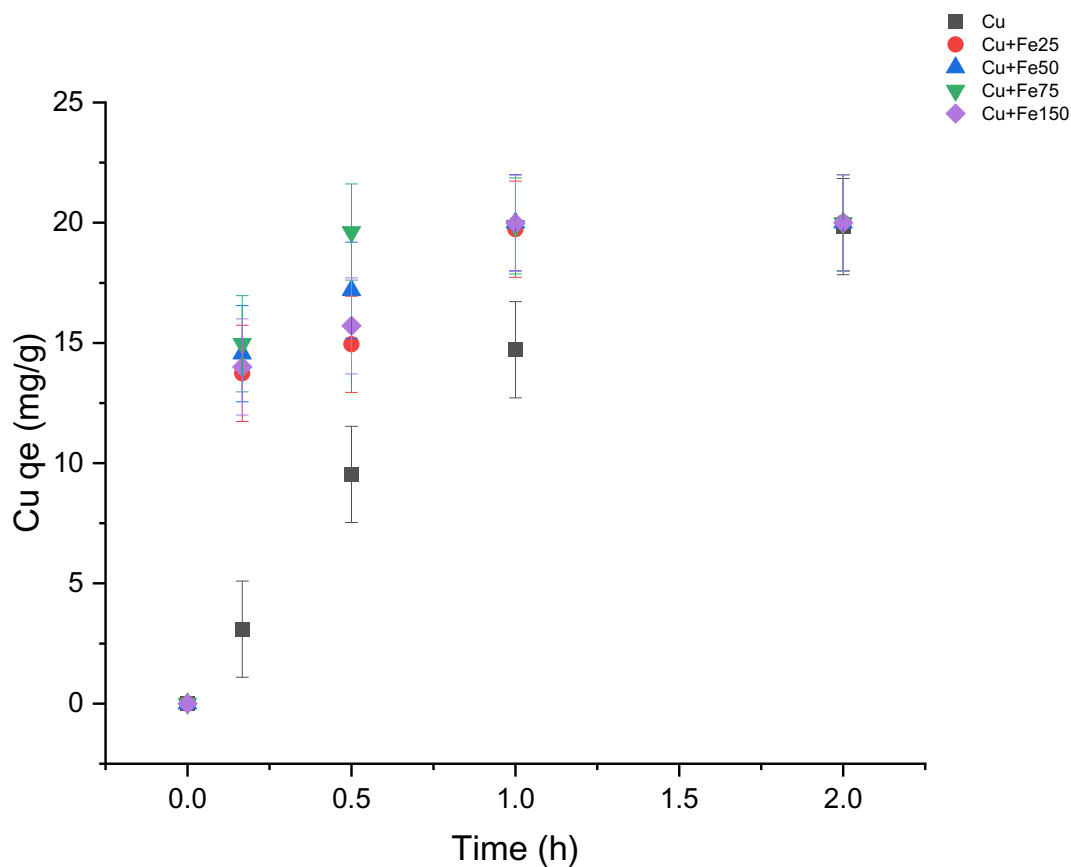


Figure 4.22 Adsorption capacity for copper as iron concentration increases

Changes in the adsorption rate occurred within the first 10 minutes, with an average increase of 11% to the adsorption capacity for copper, from the addition of iron. After 30 minutes, variation increased between the mixtures, with an average increase of 7% in the adsorption capacity for copper. The order of adsorption capacity from lowest to highest at 10 and 30 minutes was Cu+Fe 25, Cu+ Fe 150, Cu+Fe 50, and Cu+Fe 75. Within 1 hour, the copper reached equilibrium with an adsorption capacity of 20mg/g compared to single copper with 19.84mg/g after 2 hours. The increased adsorption rate in the mixture is similar to the trend for individual iron adsorption (see Figure 4.15), except the adsorption rate decreased with Fe150+Cu100. The increased copper adsorption rate with iron concentration from 25mg/L to 75mg/L is likely related to increased copper solubility, as $\text{Fe}(\text{OH})_3$ produces hydrogen ions, lowering the rate of pH increase ⁷¹. Previous adsorption studies found an optimum pH of 5 for copper, and the final pH for single metal copper was 10 versus 8 after adding iron. In comparison, an alkaline residue carbon from the gasification of tree chips, a dosage of 5g/L, with similar initial concentrations of 25 – 125mg/L, to adsorb iron (II) and copper (II), resulted in adsorption capacities of 21, and 23mg/g, respectively ⁶⁷. A cow bone charcoal study had adsorption capacities of 32.54 and 35.44 mg/g for copper and iron, respectively, and the time to equilibrium was also within 2 hours ⁶⁵.

Iron reached a maximum adsorption capacity for each initial concentration within the first 10 minutes. There was some variation for iron at 150mg/L, likely due to exceeding the solubility concentration for $\text{Fe}(\text{OH})_2$ (see Table 2.7). There was 100% removal of iron, with 92% representing adsorption. The presence of copper appeared to have little effect on the iron adsorption rate.

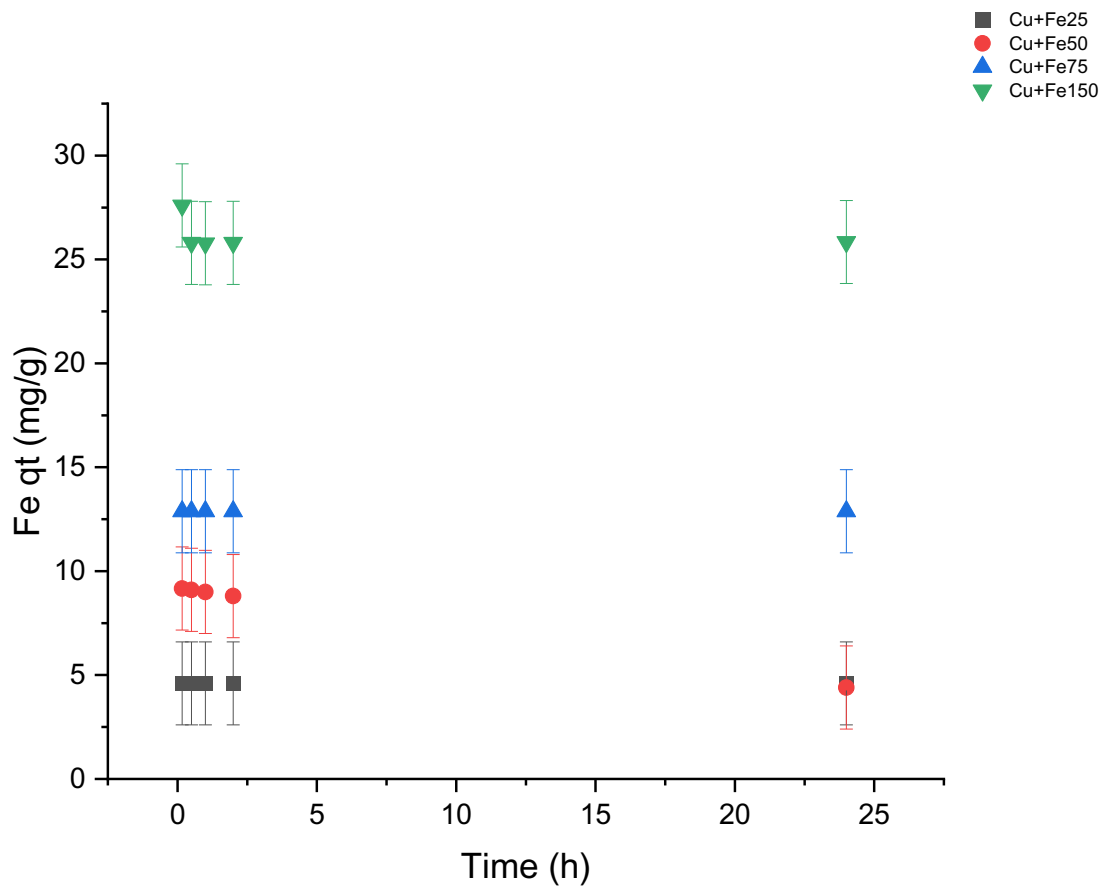


Figure 4.23 Adsorption capacity of iron in metal mixtures over time

4.2.7 Adsorption Kinetic Models for Copper

Four metal mixtures were fitted by the Pseudo First Order (PFO), the Pseudo Second Order (PSO), and the Elovich model, and the results were plotted in Figures 4.25 to 4.28. The corresponding kinetic parameters are listed in Table 4.5.

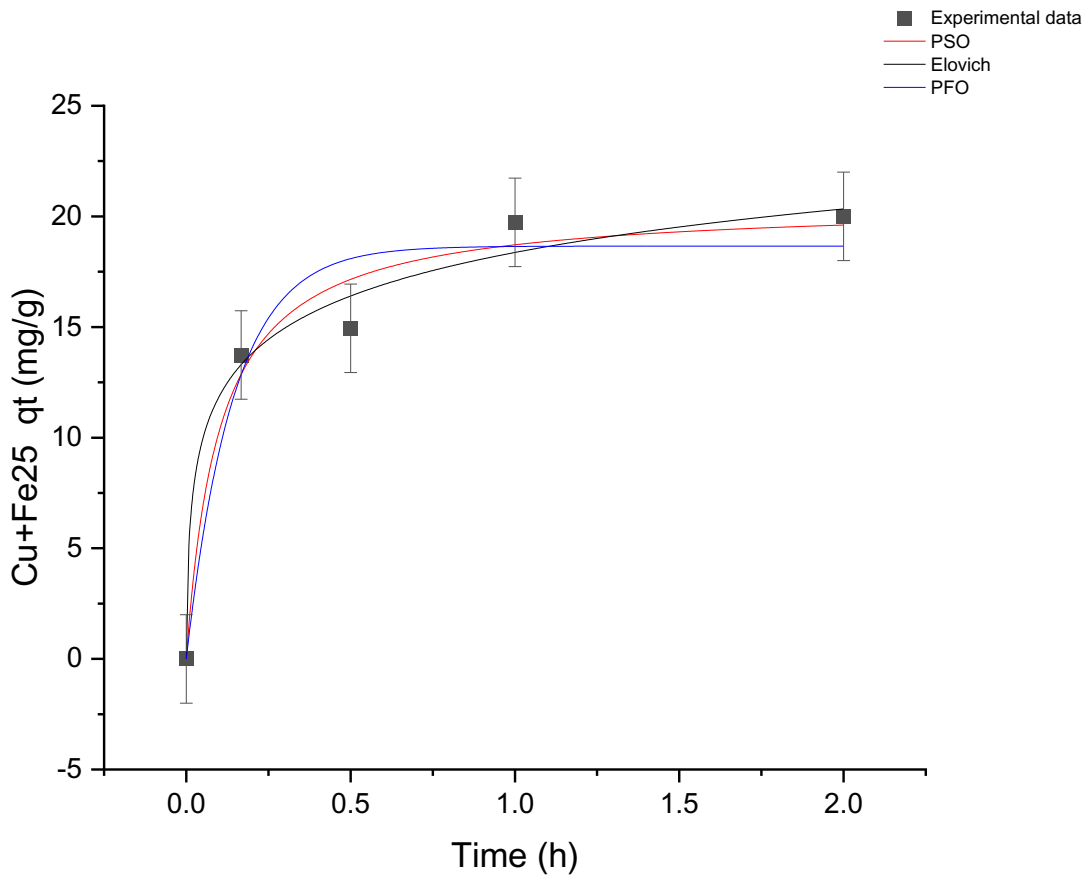


Figure 4.24 Kinetic models for copper adsorption from a mixture (25mg/L of iron + 100mg/L of copper)

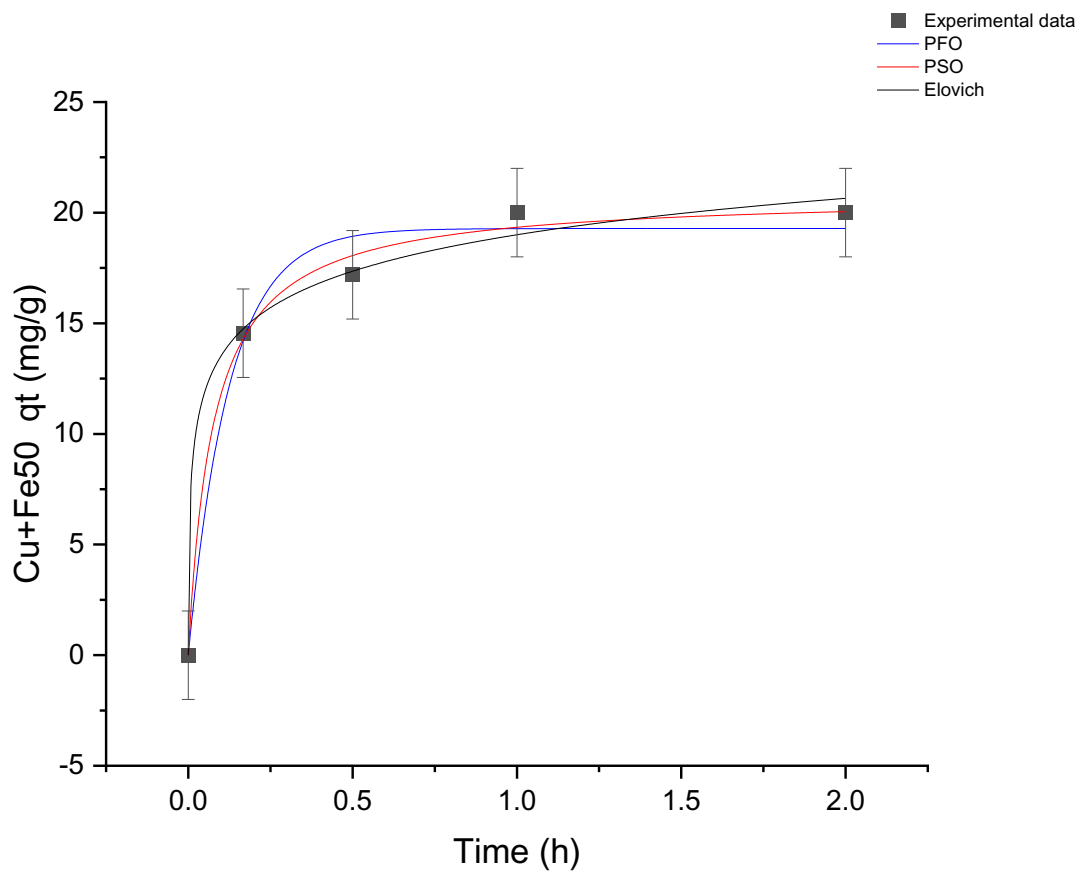


Figure 4.25 Kinetic models for copper adsorption from a mixture (50mg/L of iron + 100mg/L of copper)

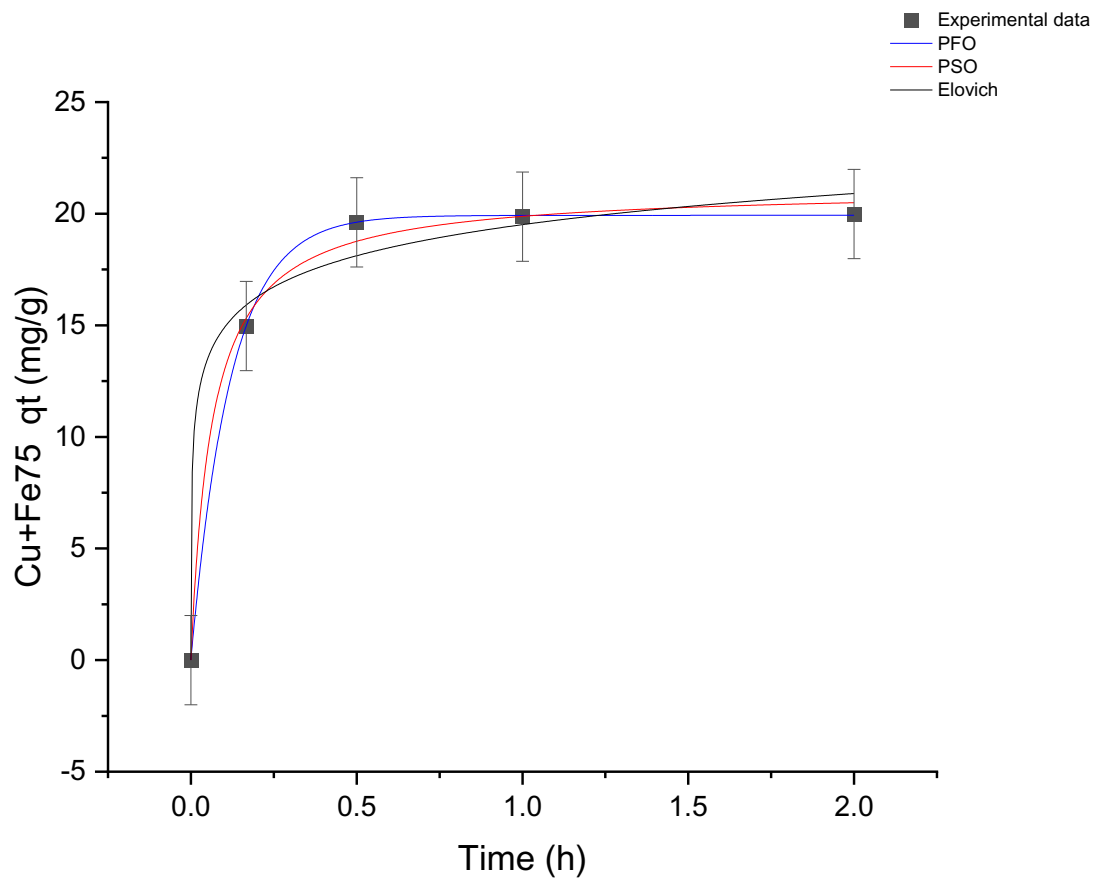


Figure 4.26 Kinetic models for copper adsorption from a mixture (75mg/L of iron + 100mg/L of copper)

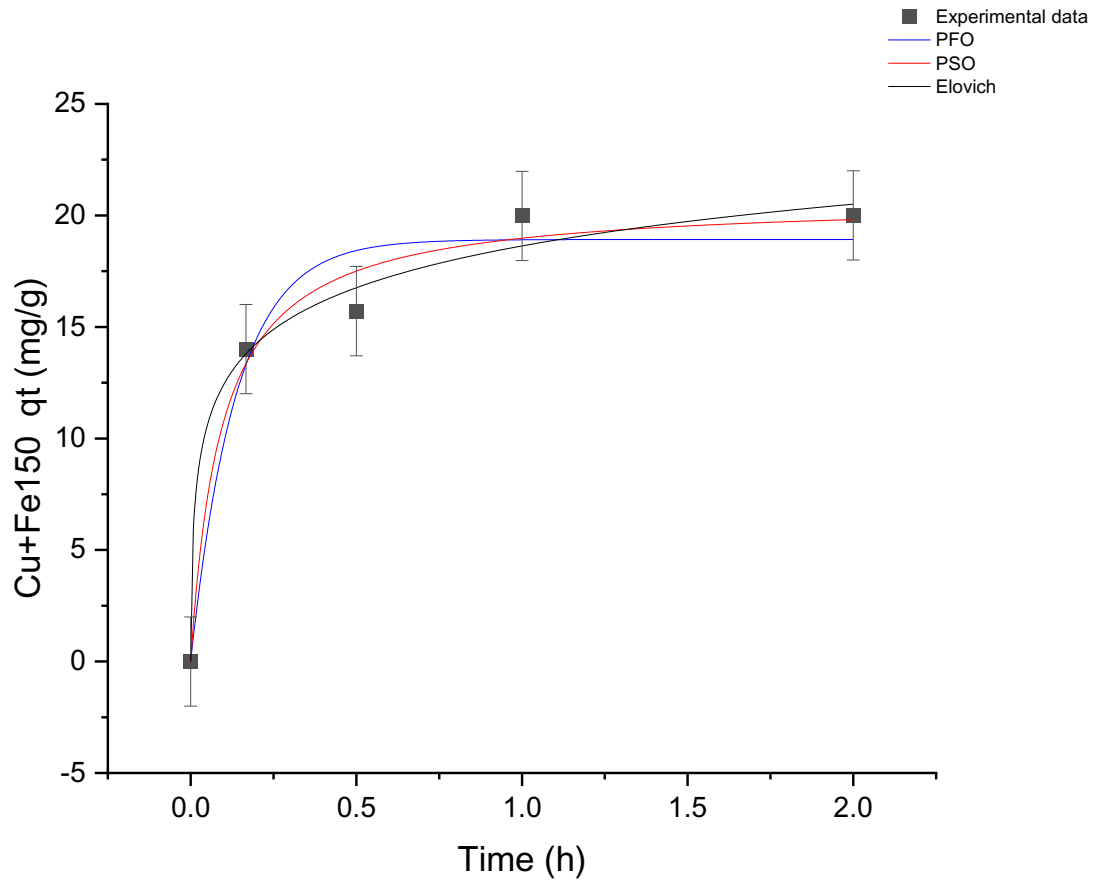


Figure 4.27 Kinetic models for copper adsorption from a mixture (150mg/L of iron + 100mg/L of copper)

The kinetic modelling parameters for copper adsorption from the mixtures are outlined in Table 4.5. A comparison of the kinetic parameters provides some insight into the factors that affected the reaction as the concentration of iron increased. There is little difference between the R^2 values; for example, Cu+ Fe 25 is fit by the Elovich model, Cu+ Fe 50 and Cu+ Fe 75 fit by the pseudo-second-order model, and then Cu+Fe 150 switches back to the Elovich Model based on R^2 and RMSE values. However, all model plots are within the data error bars to some extent. Reviewing the models' assumptions, trends in adsorption rates, and post-adsorption analysis of char offers a clearer understanding of which model best reflects the data.

The Pseudo First-Order Model is the least likely because of its requirement for a high initial concentration. This study's concentration was relatively low for copper at 100mg/L due to solubility issues from the mixture ⁷⁵. The Pseudo Second-Order Model assumes the adsorption rate is proportional to the number of available sites, resulting in rapid initial adsorption and reaching a maximum adsorption capacity as the metal ions enter the pores of the char. The maximum adsorption capacity for copper occurred at 700mg/L in the previous copper study, so the decrease in adsorption rate at Fe150+Cu 100 was unexpected ⁵⁰. The Elovich model assumes chemisorption occurs on a heterogeneous surface and relates to the diffusion of particles to the adsorption sites. Since this study used tiny particles and small-scale, well mixed, batch experiments, the internal mass transfer is negligible, and the Elovich model is less applicable. The Pseudo Second-Order Model is associated with chemisorption. In these experiments, washing the char did not remove any adsorbed copper. This indicates that the copper-char interaction is via chemical versus physical adsorption. The sum of assumptions inherent in the models and the adsorption behaviour supports the application of the Pseudo Second-Order Model. However, this

requires further study due to the complexity of solubility with precipitation and adsorption co-occurring.

Table 4.5 Adsorption kinetic parameters for copper from metal mixtures

Sample and Model	q _{max} (mg/g)	k(hr ⁻¹)	R ²	RMSE	Experimental q _{max} (mg/g)	Et(h)
Fe25+Cu100					20	2
PFO	18.66	6.98	0.955	39.80	--	--
PSO	20.59	0.48	0.974	1.71	--	--
Elovich	A	β				
	1.81 x 10 ³	0.35	0.984	1.076	--	--
Fe50+Cu100					20	1
PFO	19.28	7.99	0.985	1.04	--	--
PSO	20.81	0.63	0.995	0.31	--	--
Elovich	A	β				
	7.0 x 10 ³	0.42	0.995	0.370	--	--
Fe75+Cu100					19.87	1
PFO	19.93	8.34	1.000	1.510	--	--
PSO	21.14	0.75	0.996	0.823	--	--
Elovich	A	β				
	3.3 x 10 ⁴	0.50	0.986	0.934	--	--
Fe150+Cu100					20	2
PFO	18.92	7.28	0.962	2.54	--	--
PSO	20.73	0.52	0.983	1.17	--	--
Elovich	A	β				
	2.63 x 10 ³	0.37	0.989	0.80	--	--

The rate constant, k, for the Pseudo Second Order Models increased with iron concentration up to 75 mg/L; however, at an initial concentration of 150 mg/of iron, the rate constant decreased due to the concentration exceeding the solubility limit of Fe (OH)₂ (see Table 2.7), resulting in additional iron precipitation, limiting the mass transfer of copper ions to the char's surface. The maximum predicted adsorption (q_{max}) is approximately constant between the various concentrations. The precipitation of iron hydroxides is evident from comparing TEM images of the pre-adsorption and post-adsorption char, indicating that metals are likely adsorbed on the char (see Figure 4.37).

The XPS results showed no direct evidence of copper bonding to oxygen (see Figure 4.29); however, due to the difficulty with curve fitting for iron, this evidence may be lost in overlapping spectrums. The change in copper's adsorption rate with 150mg/L of iron may also be affected by the common ion effect, where a shift occurs in the equilibrium between a solid and the corresponding ionic form because of the addition of an ion already involved in the equilibrium reaction. Reactions with common ions lower the molar solubility of copper⁹⁰. The common ion in the mixture is sulphate, as copper was introduced as copper sulphate and iron as iron sulphate. The sulphate concentration increased from 175mg/L in Fe75+Cu100 to 250mg/L in Fe150+Cu100, promoting a lower molar solubility and decreased copper adsorption.

To assess the solubility of the metal hydroxides produced in the mixtures, the published values referenced for product solubility (K_{sp}) of $\text{Cu}(\text{OH})_2$ and $\text{Fe}(\text{OH})_2$ were 2.2×10^{-20} and 8×10^{-16} , respectively⁷⁴. These values were compared to the calculated molar solubilities based on the metal concentrations used in this study. The copper concentration in all mixtures was 100mg/L, and the corresponding calculated molar solubility of $\text{Cu}(\text{OH})_2$ was 7.87×10^{-16} , higher than the K_{sp} of 2.2×10^{-20} , indicating the precipitation of $\text{Cu}(\text{OH})_2$. However, copper was not detected in the char washes, indicating a reduction in copper hydrolysis and precipitation with a decreased pH of 8 for the mixture versus a pH of 11 as a single metal solution. Due to iron's rapid adsorption, the kinetic modelling of iron in the mixture was not completed and recommended for future research.

A multi-metal adsorption study using alkaline carbon residue also had a very high initial iron adsorption rate and was fitted with the PSO model. However, it was the only model that reported

The adsorption of 100mg/L of copper as a single metal had a lower adsorption rate than the metal mixture, reaching the maximum adsorption capacity after two hours rather than one hour with the addition of iron since the addition of iron made the solution more acidic. The copper solution had a pH of 11, while the mixture was 8. The lower pH decreases the ability of copper to form hydroxides, making the copper ions available for adsorption. The copper adsorption rate increases with initial iron concentrations of 25mg/L to 75mg/L as more hydrogen ions are produced until the solubility of Fe (OH)₂ is reached and solid iron hydroxides are formed, interfering with copper's ability to adsorb to the char.

The previous copper study with crab char reported an equilibrium time of two hours for the adsorption of 100mg/L of copper⁵⁰. The maximum adsorption capacity of 20mg/g for copper did not change significantly in the mixture or the model data.

4.2.8 Post-Adsorption Analysis

X-ray Photoelectron Spectroscopy (XPS)

The XPS spectrum was used to investigate chemical composition changes in the surface of the char after batch adsorption. The changes in the elemental composition are listed in Table 4.6, and the results are unitless as they were determined by dividing the intensity of the elements by the intensity of the carbon C1 group. The crab char before any adsorption experiment is represented as 'Before adsorption.' The char after adsorption with single metal copper or single metal iron is represented as 'After Cu' and 'After Fe', and the char after adsorption with the mixture of copper and iron is represented as 'After Fe + Cu.' The detection limit for a significant change is 0.1 atomic % for this analysis. The elemental content of the char after adsorption indicates that iron and copper are detected only after adsorption. The nitrogen as amine functionalities and calcium remained relatively the same.

After the adsorption experiments with 100mg/L of copper, copper was detected on the char as Cu^{2+} and Cu^+ as shown in Figure 2.28. The ratio of Cu^{2+} and Cu^+ was 64.7 to 35.3, Cu^{2+} being the prominent ion. After the adsorption experiments with 100mg/L of iron, iron was detected on the char in two forms, Fe^{2+} and Fe^{3+} , as shown in Figure 4.30. The ratio of Fe^{2+} to Fe^{3+} was 60.02 to 39.99, making Fe^{2+} the prominent ion on the char's surface.

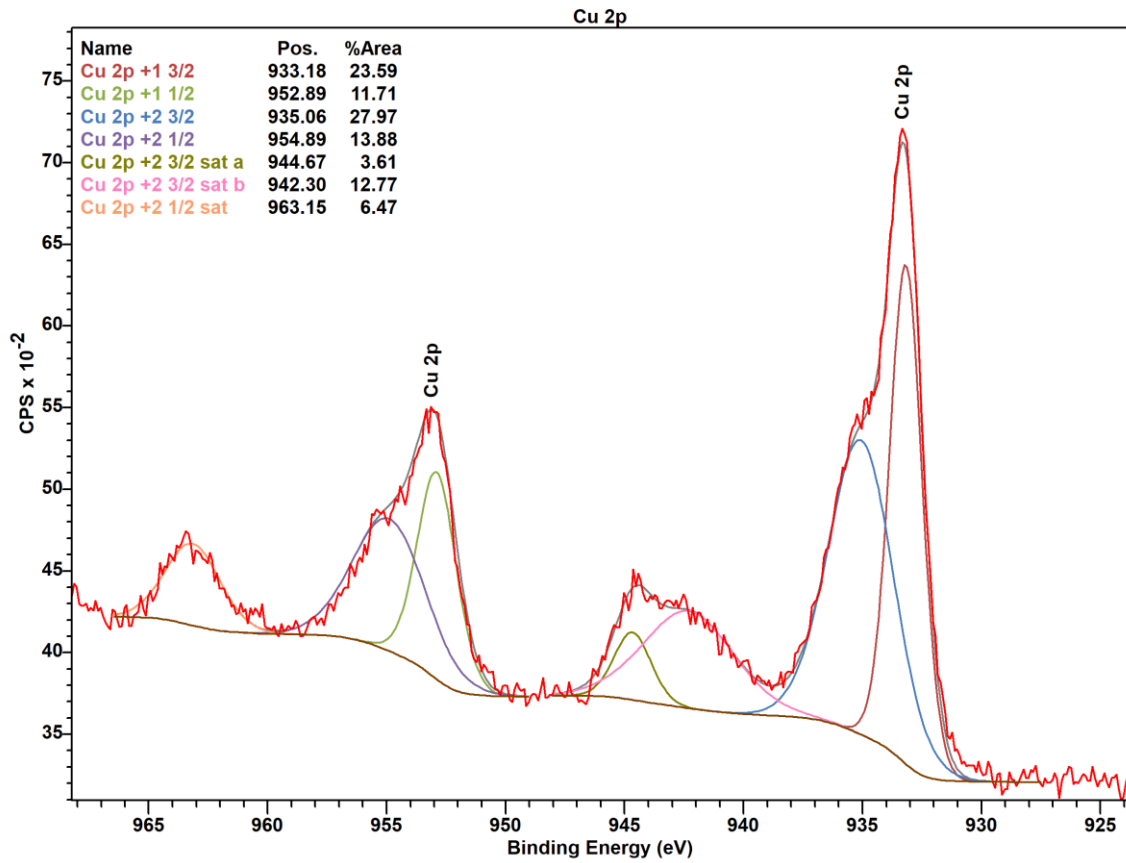
The mixture of 100mg/L of copper and 75mg/L of iron resulted in a ratio of Fe^{2+} to Fe^{3+} of 56.78 to 43.20, a slight decrease in Fe^{2+} and a slight increase in Fe^{3+} compared to the single iron char. The adsorption experiments with iron and the metal mixture resulted in a new oxygen component on the lower binding energy side of the main oxygen peak, indicating the presence of metal oxides/metal-oxygen bonded complexes, as shown in Figures 4.31 and 4.32. The orange

precipitate observed during the batch reactions was likely the source of Fe³⁺ as Fe(OH)₃. This was not shown in the copper analysis; potentially, the copper bonded to oxygen occurred at higher binding energy and was lost in overlapping peaks. The XPS results from the previous copper adsorption study also resulted in the third peak for hydroxides indicating a direct bond between copper and oxygen⁵⁰. XPS detected both iron and copper on the char after the batch reaction with a mixture of 100mg/L of copper and 75mg/L of iron, indicating that iron and possibly copper are adsorbed onto the surface of crab char through binding directly with oxygen or as hydroxides. An adsorption study using crayfish char with a pyrolysis temperature of 500°C was also determined through XPS that lead bound with oxygen forming complexes on the surface¹³.

Table 4.6 Element content analysis from XPS wide scan

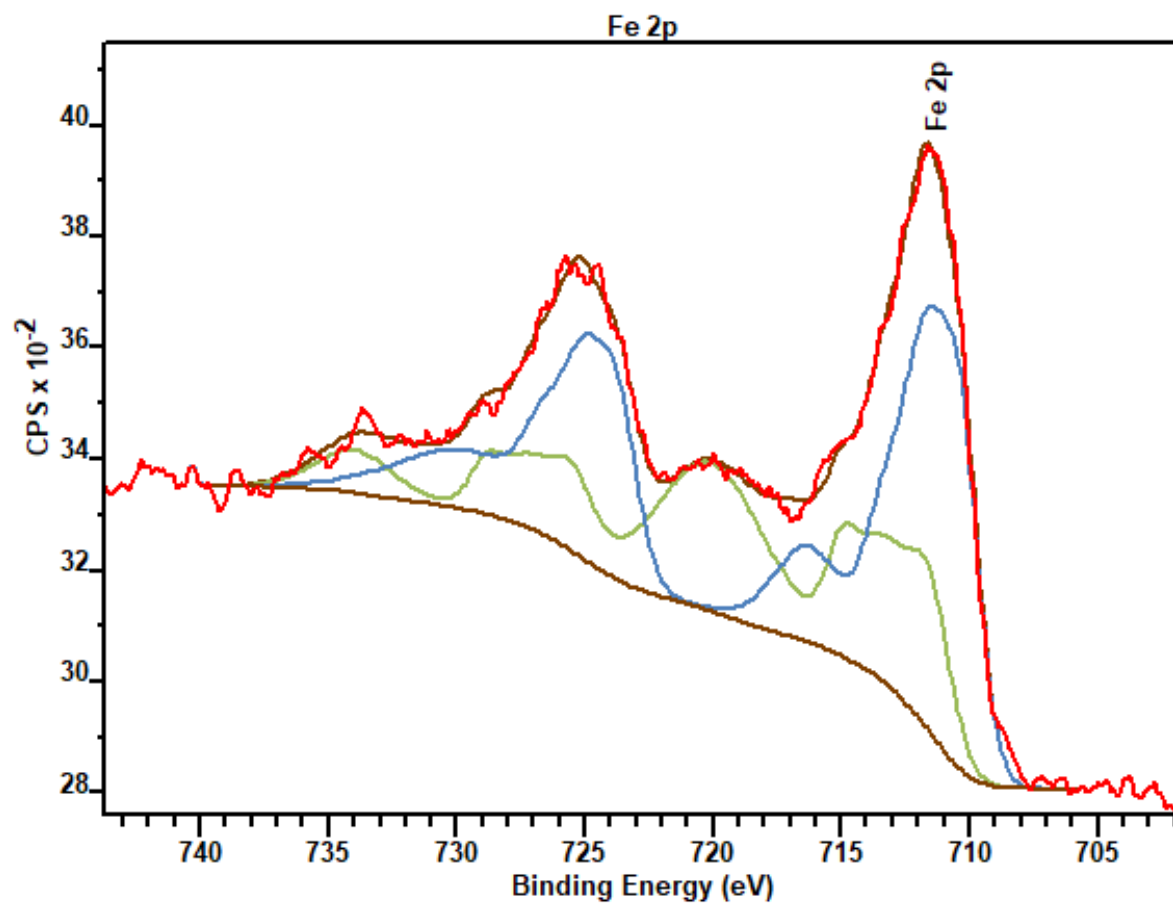
Element/C1s	Intensity Before Adsorption	Intensity After Cu Adsorption	Intensity After Fe Adsorption	Intensity After Fe+Cu Adsorption
Na 1s	0.0071	0.0105	0.0022	0.0070
Cu 2p	*	0.1093	0.0000	0.0174
Fe 2p	*	*	0.0586	0.0414
O 1s	0.4535	0.6773	0.4011	0.3378
N 1s	0.0772	0.0715	0.0347	0.0270
K 2s	*	*	0.0000	0.0015
Ca 2p	0.1039	0.1225	0.0595	0.0291
C 1s	1.0000	1.0000	1.0000	1.0000
Cl 2p	*	*	0.0011	0.0021
S 2p	0.0035	0.0116	0.0019	0.0018
P 2p	0.0410	0.0634	0.0294	0.0169
Mg 2s	*	*	0.0033	0.0036

Element is below detection limit *



Queen's University Kratos Axis Nova

Figure 4.28 XPS spectra of crab char after adsorption of copper



Queen's University Kratos Axis Nova

Figure 4.29 XPS spectra of crab char after adsorption of iron

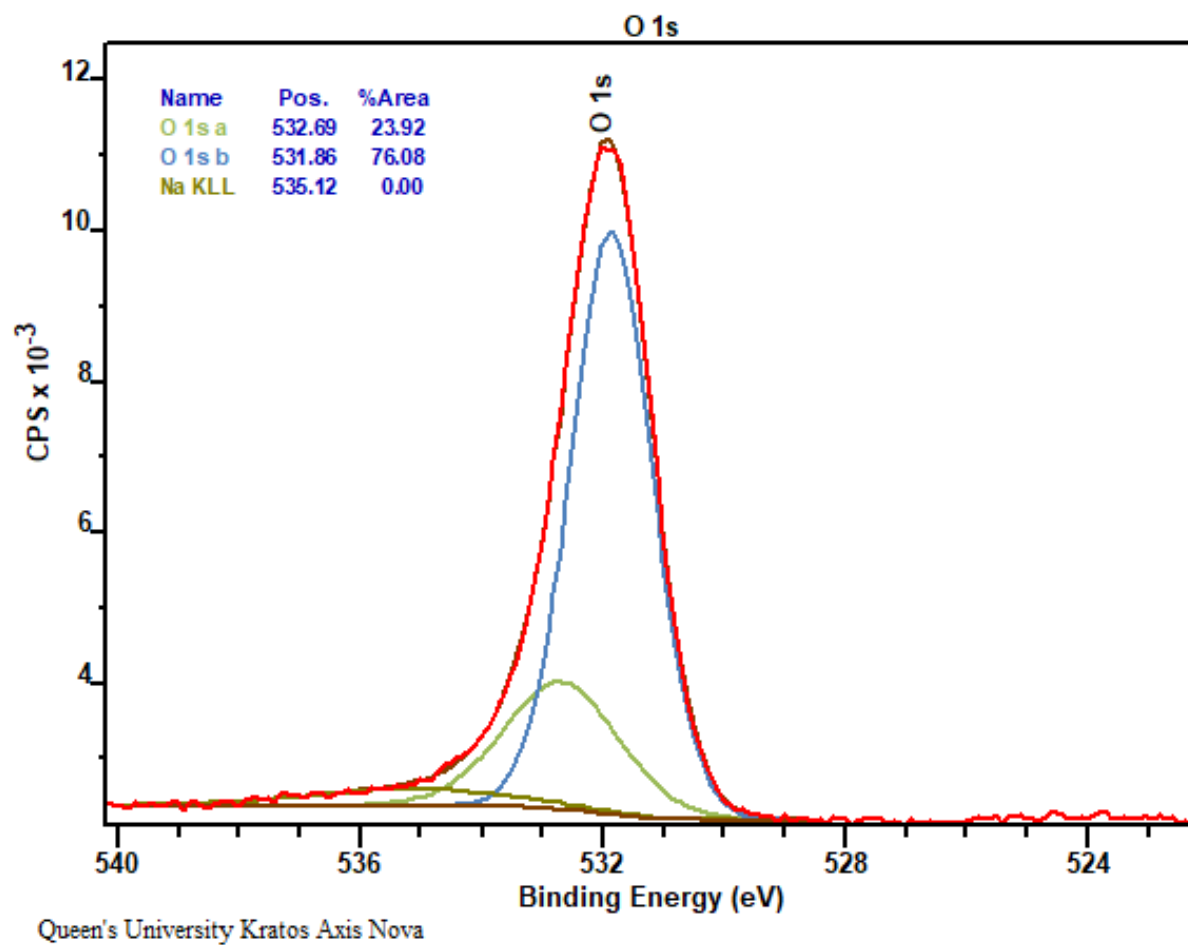
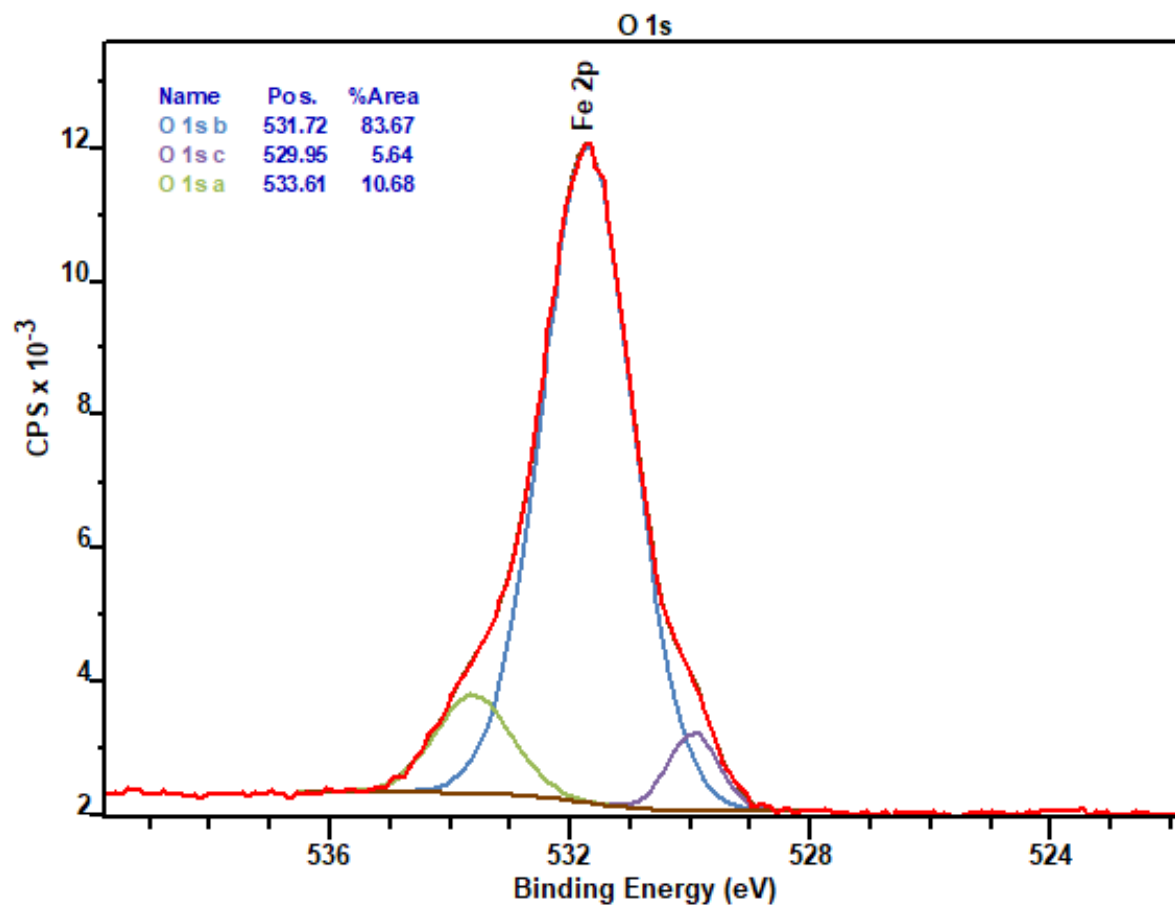
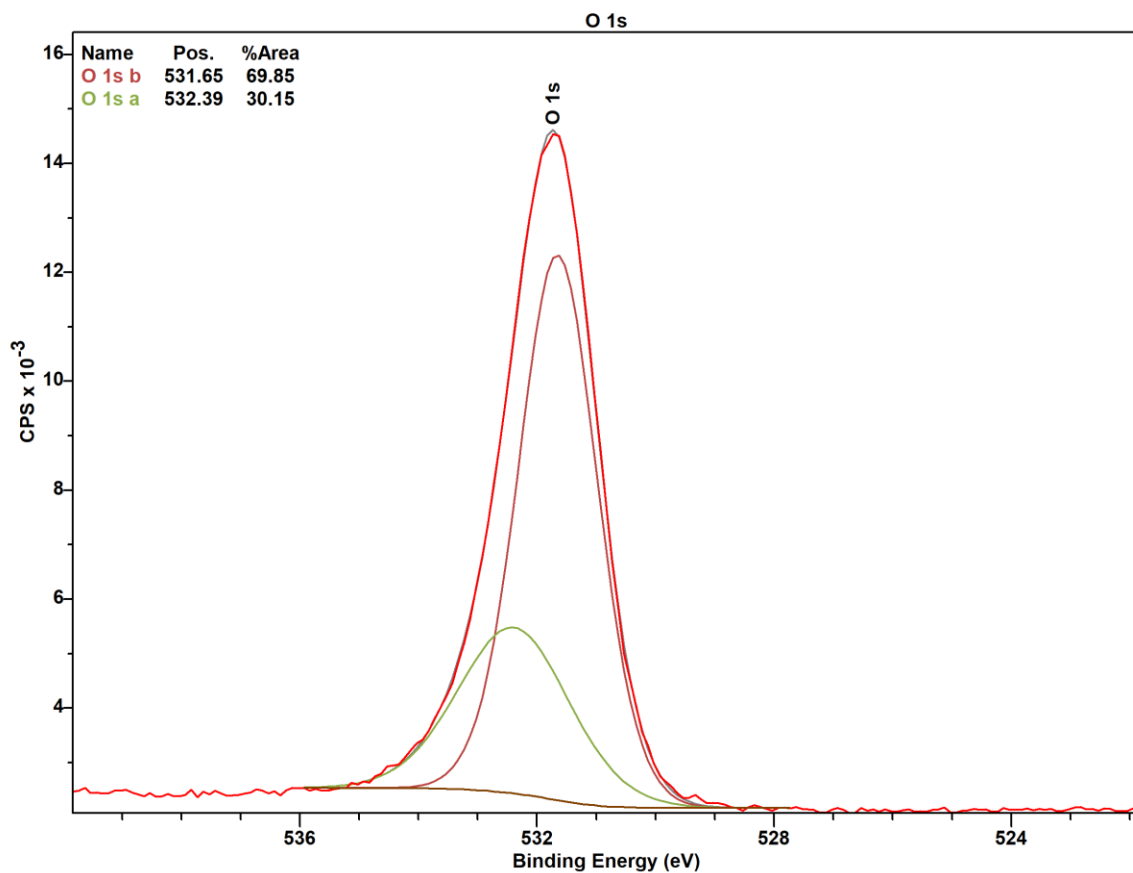


Figure 4.30 XPS high-resolution spectra of crab char before adsorption



Queen's University Kratos Axis Nova

Figure 4.31 XPS high-resolution spectra of crab chat after iron adsorption



Queen's University Kratos Axis Nova

Figure 4.32 XPS high-resolution spectra of crab after copper adsorption

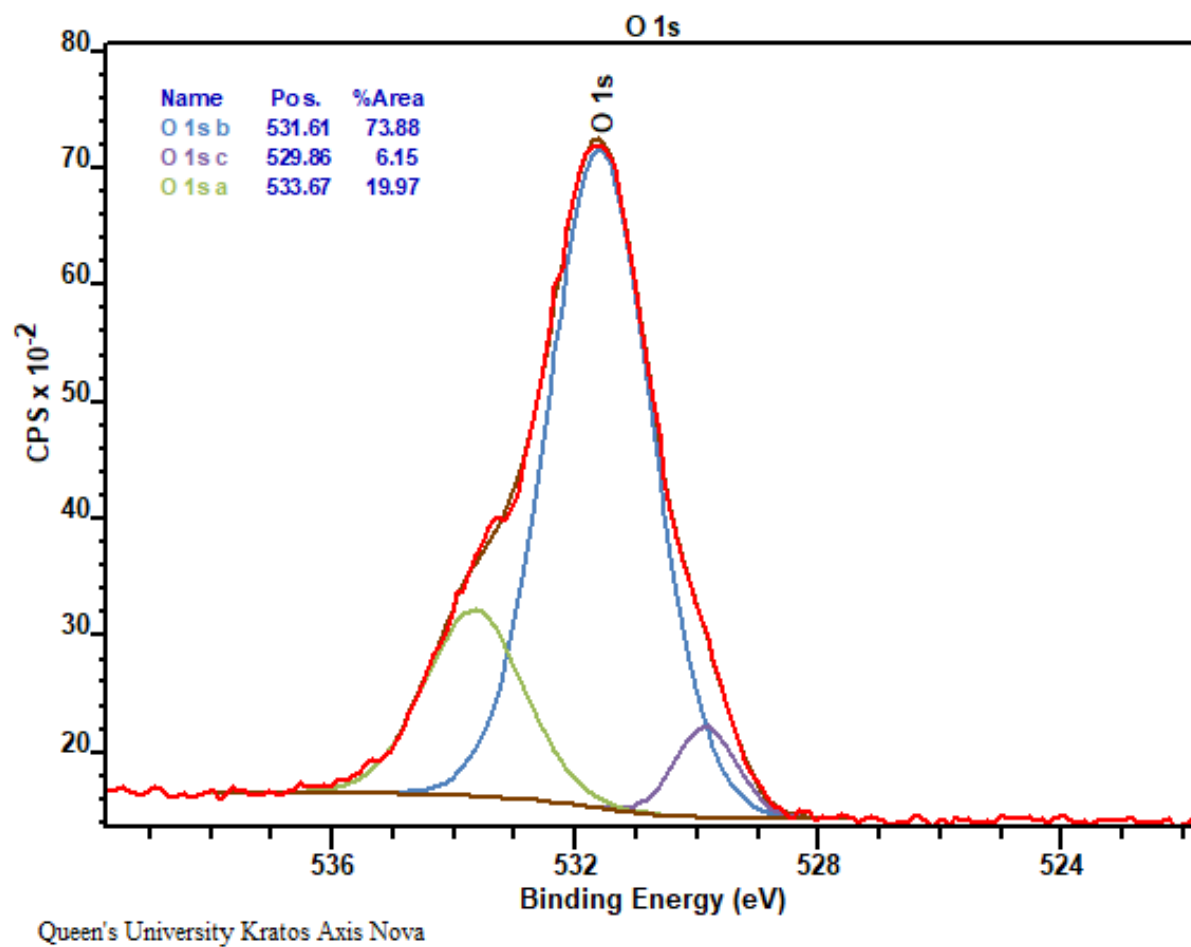


Figure 4.33 XPS high-resolution spectra of crab char after mixture (75mg/L of iron + 100mg/L of copper)

X-ray Diffraction (XRD)

Figure 4.35 shows XRD results comparing the original crab char to the post-absorption char from the metal mixture of 100mg/L of copper and 75mg/L of iron.

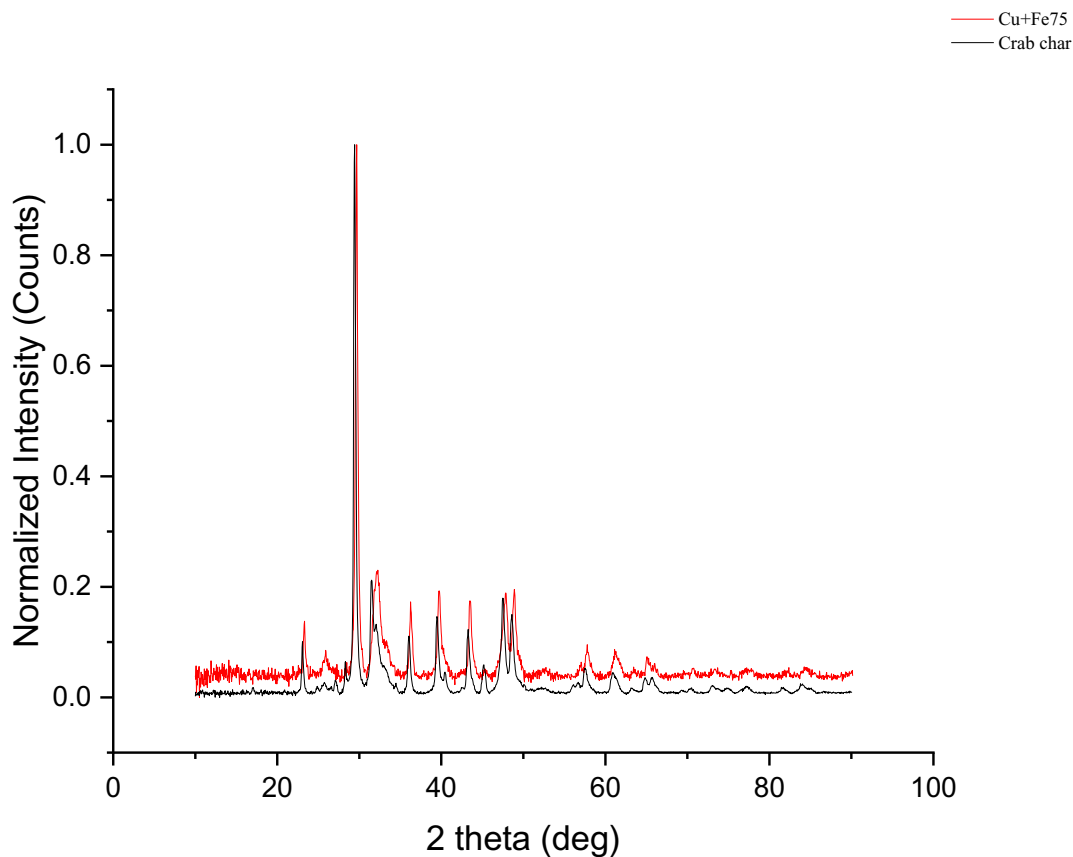


Figure 4.34 XRD spectra of pre and post adsorption crab char from a mixture (75mg/L of iron + 100mg/L of copper)

The similarity in peak intensity and location indicates that the crystalline structure of the char did not significantly change. The peak for calcite at approximately 30° remained as well as smaller peaks for calcium carbonate. The intensity below 22° appeared to increase after adsorption of

the mixture, and in the previous copper adsorption study, this was attributed to the formation of posnjakite, $\text{Cu}_4(\text{SO}_4)(\text{OH})_4 \cdot 2\text{H}_2\text{O}$ ⁵⁰.

Fourier Transform Infrared Spectroscopy (FTIR)

Figure 4.36 compares the crab char before and after adsorption of the metal mixture, 100mg/L of copper and 75mg/L of iron. After adsorption, the intensity of the major peaks associated with the calcite spectra decreased at approximately 1400cm^{-1} and 1000 cm^{-1} , and a slight decrease in the intensity at approximately 875 cm^{-1} . This is potentially related to iron and possibly copper binding with oxygen on the char's surface, as discussed in the XPS results.

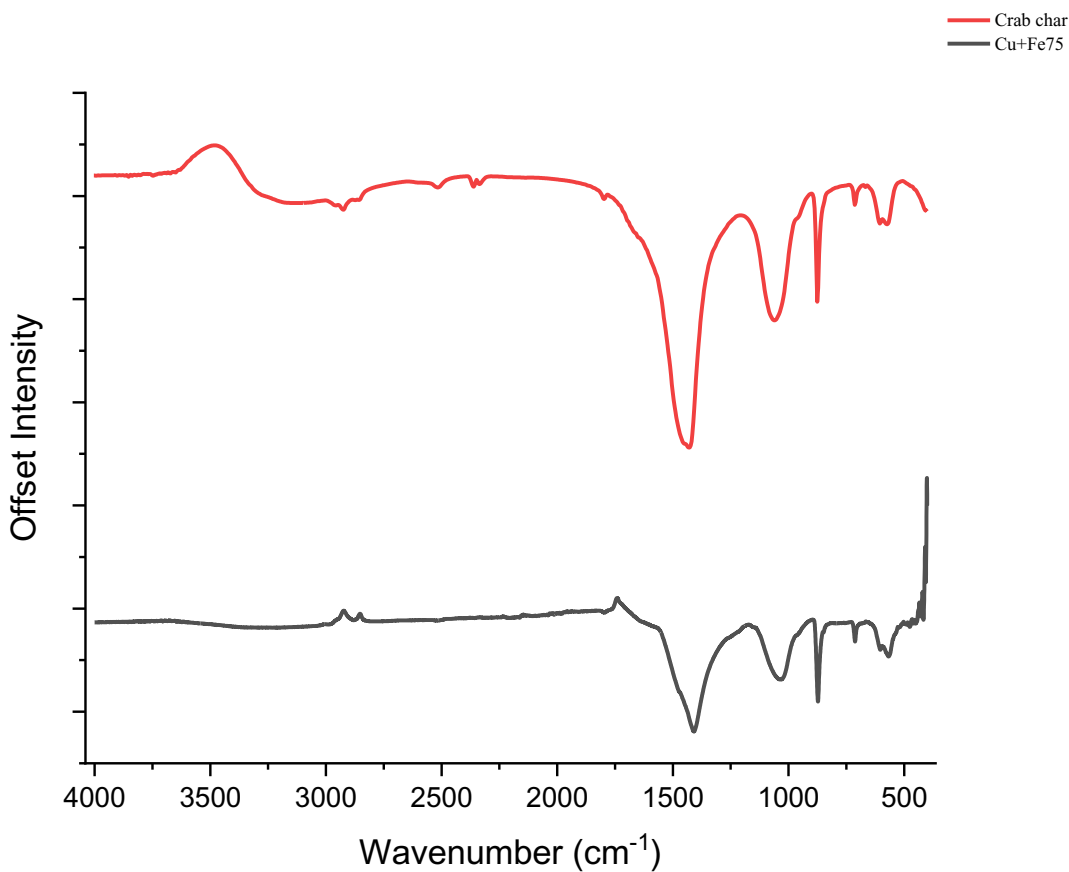


Figure 4.35 Comparison of pre and post adsorption crab char from a mixture (75mg/L of iron + 100mg/L of copper)

Surface Area

Table 4.7 provides crab chars' post adsorption surface area from single metals and mixtures. The surface area of the original crab char was 14.73 m²/g, and after adsorption of the metal mixture, 100mg/l of copper and 75mg/l of iron, the surface area increased by approximately 12%. After the adsorption of 25mg/l of iron, the surface area increased by approximately 32%. The final pH of the mixture is approximately 8 and promotes the formation of iron hydroxides with low solubility. The lower iron concentration of 25mg/L results in higher solubility, making more iron available for adsorption and increasing the surface area slightly.

Table 4.7 Surface area of pre and post adsorption crab char

Sample	BET Surface Area(m ² /g)
Crab char	14.73
100mg/l Cu + 75mg/l Fe	16.73
25mg/l Fe	20.25

Transmission Electron Microscope (TEM)

TEM images of crab char before and after adsorption are shown in Figure 4.37. A is crab char before adsorption and contains amorphous calcium carbonate and a rectangular calcite crystal near the center with relatively smooth sides. B contains crab char after iron adsorption, and near the bottom of the image, a rectangular shaped piece of char has lighter circular deposits on the surface of the char, with a darker line running through the center. C contains crab char after copper adsorption and a pattern of lighter dots over the char, with a darker line through the center of the char. Finally, D contains crab char after adsorption of a mixture of copper and iron, with the char surface appearing more heterogeneous with circular deposits and a darker line running through the center of the char. These images show a change in the surface and potentially the interior of the char after adsorption with copper and iron.

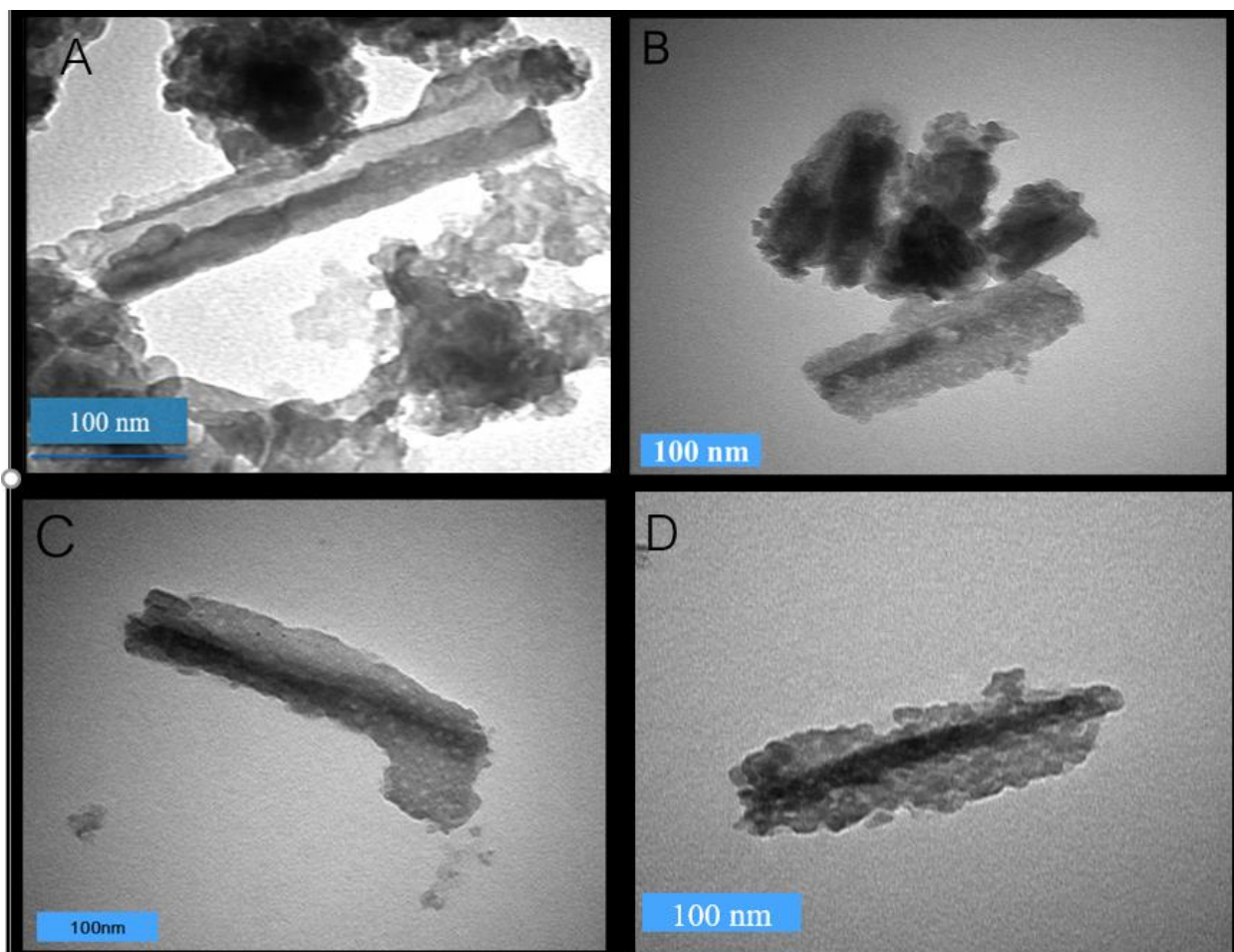


Figure 4.36 TEM images of crab char before adsorption (A), after iron adsorption (B), after copper adsorption (C), and after mixture adsorption (75mg/L of iron + 100mg/L of copper)

4.2.9 Adsorption Mechanism

The adsorption pathway for metals is often impacted by (1) the chemistry of the metal ion (speciation) or metal ion complex, (2) the solution pH and the point of zero charge of the surface, (3) the surface area and porosity, (4) the surface composition and (5) the size of adsorbing species⁶⁷. The rapid initial rate of adsorption strongly indicates crab char's affinity for copper and iron as single metals and as mixtures (see Figures 4.23 to 4.27). The formation of iron hydroxides with low solubility likely affected the adsorption of iron and copper. The metal mixture at Fe150+Cu100 surpassed the solubility of Fe (OH)₂, increasing the amount of solid iron hydroxides and reducing copper's transport and access to adsorption sites, decreasing the adsorption rate in contrast to iron concentrations from 25 to 75mg/L.

This study compared the char characteristics before and after adsorption through XPS, FTIR, XRD, and TEM and found that iron, as a single metal or mixture, was adsorbed through binding with oxygen on the surface. In the pre-adsorption crab char, the FTIR detected oxygen containing functional groups such as carbonyls, carboxylates, and esters (see Figure 4.35). Copper likely bonded with oxygen at the surface to form oxides or hydroxides, as identified by the XPS analysis from the previous copper study⁵⁰. No copper was detected after the char washes, indicating that copper did not precipitate out of the solution or was dissolved from the surface. The XPS analysis identified that both metals were in two different oxidation states, Fe (II) and Fe (III) for iron and Cu (I) and Cu (II) for copper, and with the heterogeneity of the crab char, there are several likely combinations for the adsorption mechanisms. In comparison, an arsenic adsorption study using crawfish char from a pyrolysis temperature of 450°C found that adsorption included physisorption and complexation with C=O, -OH, and -O-H⁶¹. A multi-metal adsorption study of lead, arsenic,

and copper with crayfish char from a pyrolysis temperature of 650°C found that physisorption, complexation, and ion exchange attributed to metal removal ⁵³.

Chapter 5: Conclusions and Recommendations

5.1 Conclusions

Pyrolyzing this global food waste into char can reduce the amount of dumping and its associated environmental and economic impacts. The literature review confirmed that crab biochar is a new area of research, with few adsorption studies using metal mixtures and crustacean biochar. Studies included lead and arsenic mixtures with high removal rates. No marine crustacean studies used iron or iron mixed with copper.

The objectives of this study included producing slow pyrolysis crab char and comparing the physical and chemical characteristics of fast and slow pyrolysis crab char. Approximately 250g of Snow Crab (*Chionoecetes Opilio*) underwent slow pyrolysis, with a heat ramp of 6°C/minute, and held at 500°C for 3.5 hr. Approximately 5g of Snow Crab underwent fast pyrolysis with no heat ramp and was held at 500°C for 5 minutes. Slow pyrolysis produced a porous char with a 55 wt% yield, a surface area of 14.73m²/g, and a pore size of 21.5nm. Elemental analysis indicated 22.69wt% carbon, 1.24wt% hydrogen, and 2.72wt% nitrogen, while proximate analysis determined 12 wt% volatiles, 57 wt% ash and approximately 27 wt% calcium carbonate. XRD suggested the presence of calcite with amorphous calcium carbonate, and the IR found functional groups such as carboxyls and carbonyls. Carbonyls were also detected with solid state NMR along with aromatics and alkyl groups. The different pyrolysis conditions resulted in very similar chars, apart from volatile content. Slow pyrolysis char contained 1.8 times more volatiles than fast pyrolysis because of heat and mass transfer limitations.

The initial pH had little effect on iron removal due to the char's high alkalinity, and the low solubility of hydroxides, resulting in an adsorption capacity of 18.4mg/g. A slight variation in

adsorption capacity occurred between 20°C to 40°C with percent removals of 92% and 100%, respectively, with no significant difference between 4°C, 13°C, and 40°C. The presence of sulphate and the temperature effect on the co-occurring oxidation and hydrolysis reactions may have played a role in that variation ⁷¹. With a dosage of 5g/L, the adsorption capacity for iron was 18.4mg/g with 100% removal after 0.5hr. Iron precipitated at a rate of 8% of the initial iron concentration as iron hydroxide during the adsorption experiments, lowering the pH and the calculated adsorption capacity for iron ⁷⁸.

The adsorption experiments with copper as a single metal found 100% removal of copper and an adsorption capacity of 20mg/g within 2 hours. Comparing the results from iron and copper as single metals suggests that crab char adsorbs iron four times faster than copper due to iron's higher affinity for oxygen and the presence of calcite and oxygen containing functional groups such as carbonyls.

The adsorption experiments with the iron and copper mixtures found that increasing iron concentration increased the adsorption rate of copper until the iron concentration surpassed the solubility limit of $\text{Fe}(\text{OH})_2$ with 150mg/L of iron. Copper's adsorption capacity reached 20mg/g in 0.5hr with Fe75+Cu100 and was fit by the Pseudo Second Order Model with an R^2 of 0.996 and an RMSE of 0.823. Copper's adsorption rate as a mixture was four times higher than copper as a single metal and may be attributed to the production of hydrogen ions from $\text{Fe}(\text{OH})_3$, as the pH was 8 versus a pH of 10 as a single metal ⁷¹. The mechanism of adsorption for iron (II) and (III) was likely binding directly with oxygen from functional groups on the char's surface. Copper also likely bonded with oxygen since it was not detected in the char wash.

Crab biochar, either through fast or slow pyrolysis, is a potential treatment for AMD and other wastewater containing metal mixtures such as iron and copper. The combination of oxygen containing functional groups and a high calcium carbonate content causes iron to be removed through adsorption and precipitation, which makes more adsorption sites available for copper and other metals.

5.2 Future Research

Adsorption research involving crustacean based biochar is relatively new, with few studies involving heavy metals. Future recommendations include:

1. Producing fast pyrolysis crayfish char with no heat ramp at 500°C for approximately 5 minutes and comparing these char characteristics and copper adsorption results to the previously published fast pyrolysis crab char⁵⁰. Comparing feedstock efficiency is important for scaling up, especially since aquaculture makes crayfish more accessible than wild crabs,
2. Analyzing the crustacean char for oxygen and organic carbon content with slow and fast pyrolysis would provide O/C and H/C ratios for comparison since the relative number of functional groups on the char would be related to the O/C ratio, which is very important for metal adsorption. The H/C ratio is related to the stability of the biochar and is a critical factor if the char is applied to soils. This char analysis would help decide between slow or fast pyrolysis based on the intended application.
3. An adsorption study where the particle size of the crab biochar is increased for the same initial concentrations to determine if the adsorption rate varies, suggesting internal mass transfer limitations for the metals.
4. Conduct isotherm analysis using ICP with initial concentrations of 200 to 1500mg/L to determine the maximum adsorption capacity for iron as a single metal and a copper and iron mixture.
5. An adsorption study mixing copper and iron in a one-to-one ratio may highlight patterns of metal competition with crab biochar.
6. For thermodynamic and kinetic analysis involving iron, dosage experiments with low loading rates, such as 0.1 to 0.5g/L, would decrease the rapid initial adsorption rate.

7. Based on the rapid adsorption of iron with crab biochar, the solution should be sampled every five minutes or less.
8. Previous studies have modified biochar with iron sulphate for mercury and arsenic adsorption. Since there is evidence that iron is bound to oxygen in the crab char, a study using post-adsorption char for arsenic or mercury removal may also be of interest ⁹¹.

References

- (1) Erasmus, V. N.; Kadhila, T.; Gabriel, N. N.; Thyberg, K. L.; Ilungu, S.; Machado, T. Assessment and Quantification of Namibian Seafood Waste Production. *Ocean Coast. Manag.* **2021**, *199*, 105402. <https://doi.org/10.1016/j.ocecoaman.2020.105402>.
- (2) Park, I.; Tabelin, C. B.; Jeon, S.; Li, X.; Seno, K.; Ito, M.; Hiroyoshi, N. A Review of Recent Strategies for Acid Mine Drainage Prevention and Mine Tailings Recycling. *Chemosphere* **2019**, *219*, 588–606. <https://doi.org/10.1016/j.chemosphere.2018.11.053>.
- (3) Skousen, J.; Zipper, C. E.; Rose, A.; Ziemkiewicz, P. F.; Nairn, R.; McDonald, L. M.; Kleinmann, R. L. Review of Passive Systems for Acid Mine Drainage Treatment. *Mine Water Environ.* **2017**, *36* (1), 133–153. <https://doi.org/10.1007/s10230-016-0417-1>.
- (4) Rambabu, K.; Banat, F.; Pham, Q. M.; Ho, S.-H.; Ren, N.-Q.; Show, P. L. Biological Remediation of Acid Mine Drainage: Review of Past Trends and Current Outlook. *Environ. Sci. Ecotechnology* **2020**, *2*, 100024. <https://doi.org/10.1016/j.ese.2020.100024>.
- (5) *Mend / Default*. <http://mend-nedem.org/default/> (accessed 2021-04-09).
- (6) Canada, E. and C. C. *Metal and Diamond Mining Effluent Regulations (SOR/2002-222)*. aem. <https://www.canada.ca/en/environment-climate-change/services/managing-pollution/sources-industry/mining/regulations.html> (accessed 2021-03-29).
- (7) Brăhăița, I.-D.; Pop, I.-C.; Baci, C.; Modoi, C.; Popița, G.; Truță, R.-M. THE EFFICIENCY OF LIMESTONE IN NEUTRALIZING ACID MINE DRAINAGE – A LABORATORY STUDY. *Carpathian Journal of Earth and Environmental Sciences*. **2017**
- (8) Aubé, B.; Eng, P. *The Science of Treating Acid Mine Drainage and Smelter Effluents*. **2004**.
- (9) Brown, T. R.; Wright, M. M.; Brown, R. C. Estimating Profitability of Two Biochar Production Scenarios: Slow Pyrolysis vs Fast Pyrolysis. *Biofuels Bioprod. Biorefining* **2011**, *5* (1), 54–68. <https://doi.org/10.1002/bbb.254>.

- (10) Dai, L.; Tan, F.; Li, H.; Zhu, N.; He, M.; Zhu, Q.; Hu, G.; Wang, L.; Zhao, J. Calcium-Rich Biochar from the Pyrolysis of Crab Shell for Phosphorus Removal. *J. Environ. Manage.* **2017**, *198*, 70–74. <https://doi.org/10.1016/j.jenvman.2017.04.057>.
- (11) Chen, T.; Quan, X.; Ji, Z.; Li, X.; Pei, Y. Synthesis and Characterization of a Novel Magnetic Calcium-Rich Nanocomposite and Its Remediation Behaviour for As(III) and Pb(II) Co-Contamination in Aqueous Systems. *Sci. Total Environ.* **2020**, *706*, 135122. <https://doi.org/10.1016/j.scitotenv.2019.135122>.
- (12) Xu, Q.; Zhou, Q.; Pan, M.; Dai, L. Interaction between Chlortetracycline and Calcium-Rich Biochar: Enhanced Removal by Adsorption Coupled with Flocculation. *Chem. Eng. J.* **2020**, *382*, 122705. <https://doi.org/10.1016/j.cej.2019.122705>.
- (13) Sun, T.; Xu, Y.; Sun, Y.; Wang, L.; Liang, X.; Jia, H. Crayfish Shell Biochar for the Mitigation of Pb Contaminated Water and Soil: Characteristics, Mechanisms, and Applications. *Environ. Pollut.* **2021**, *271*, 116308. <https://doi.org/10.1016/j.envpol.2020.116308>.
- (14) Huang, S.; Ding, Y.; Li, Y.; Han, X.; Xing, B.; Wang, S. Nitrogen and Sulphur Co-Doped Hierarchical Porous Biochar Derived from the Pyrolysis of Mantis Shrimp Shell for Supercapacitor Electrodes. *Energy Fuels* **2021**, *35* (2), 1557–1566. <https://doi.org/10.1021/acs.energyfuels.0c04042>.
- (15) Yu, J.; Tang, L.; Pang, Y.; Zeng, G.; Feng, H.; Zou, J.; Wang, J.; Feng, C.; Zhu, X.; Ouyang, X.; Tan, J. Hierarchical Porous Biochar from Shrimp Shell for Persulfate Activation: A Two-Electron Transfer Path and Key Impact Factors. *Appl. Catal. B Environ.* **2020**, *260*, 118160. <https://doi.org/10.1016/j.apcatb.2019.118160>.
- (16) Dai, L.; Zhu, W.; He, L.; Tan, F.; Zhu, N.; Zhou, Q.; He, M.; Hu, G. Calcium-Rich Biochar from Crab Shell: An Unexpected Super Adsorbent for Dye Removal. *Bioresour. Technol.* **2018**, *267*, 510–516. <https://doi.org/10.1016/j.biortech.2018.07.090>.
- (17) Yuan, T.; He, W.; Yin, G.; Xu, S. Comparison of Bio-Chars Formation Derived from Fast and Slow Pyrolysis of Walnut Shell. *Fuel* **2020**, *261*, 116450. <https://doi.org/10.1016/j.fuel.2019.116450>.
- (18) Yang, Z.; Kumar, A.; Huhnke, R. L.; Buser, M.; Capareda, S. Pyrolysis of Eastern Redcedar: Distribution and Characteristics of Fast and Slow Pyrolysis Products. *Fuel* **2016**, *166*, 157–165. <https://doi.org/10.1016/j.fuel.2015.10.101>.

- (19) Mortari, D. A.; Perondi, D.; Rossi, G. B.; Bonato, J. L.; Godinho, M.; Pereira, F. M. The Influence of Water-Soluble Inorganic Matter on Combustion of Grape Pomace and Its Chars Produced by Slow and Fast Pyrolysis. *Fuel* **2021**, *284*, 118880. <https://doi.org/10.1016/j.fuel.2020.118880>.
- (20) Duman, G.; Okutucu, C.; Ucar, S.; Stahl, R.; Yanik, J. The Slow and Fast Pyrolysis of Cherry Seed. *Bioresour. Technol.* **2011**, *102* (2), 1869–1878. <https://doi.org/10.1016/j.biortech.2010.07.051>.
- (21) Barik, D. Chapter 3 - Energy Extraction From Toxic Waste Originating From Food Processing Industries. In *Energy from Toxic Organic Waste for Heat and Power Generation*; Barik, D., Ed.; Woodhead Publishing Series in Energy; Woodhead Publishing, 2019; pp 17–42. <https://doi.org/10.1016/B978-0-08-102528-4.00003-1>.
- (22) Yuan, T.; He, W.; Yin, G.; Xu, S. Comparison of Bio-Chars Formation Derived from Fast and Slow Pyrolysis of Walnut Shell. *Fuel* **2020**, *261*, 116450. <https://doi.org/10.1016/j.fuel.2019.116450>.
- (23) Yan, N.; Chen, X. Sustainability: Don't Waste Seafood Waste. *Nature* **2015**, *524* (7564), 155–157.
- (24) Hall, K. D.; Guo, J.; Dore, M.; Chow, C. C. The Progressive Increase of Food Waste in America and Its Environmental Impact. *PLoS ONE* **2009**, *4* (11), e7940. <https://doi.org/10.1371/journal.pone.0007940>.
- (25) Poore, J.; Nemecek, T. Reducing Food's Environmental Impacts through Producers and Consumers. *Science* **2018**, *360* (6392), 987–992. <https://doi.org/10.1126/science.aaq0216>.
- (26) Reid, A. J.; Carlson, A. K.; Creed, I. F.; Eliason, E. J.; Gell, P. A.; Johnson, P. T. J.; Kidd, K. A.; MacCormack, T. J.; Olden, J. D.; Ormerod, S. J.; Smol, J. P.; Taylor, W. W.; Tockner, K.; Vermaire, J. C.; Dudgeon, D.; Cooke, S. J. Emerging Threats and Persistent Conservation Challenges for Freshwater Biodiversity. *Biol. Rev.* **2019**, *94* (3), 849–873. <https://doi.org/10.1111/brv.12480>.
- (27) The Effects of Fish Processing Bio-Waste on the Ocean's Organisms and Nutrients. *ScienceBuzz*, 2019.
- (28) Causes, Effects & Solutions for Ocean Dumping. *E&C*, 2020.

- (29) Bhaskar, T.; Pandey, A. Advances in Thermochemical Conversion of Biomass—Introduction. In *Recent Advances in Thermo-Chemical Conversion of Biomass*; Elsevier, 2015; pp 3–30. <https://doi.org/10.1016/B978-0-444-63289-0.00001-6>.
- (30) Dhyani, V.; Bhaskar, T. A Comprehensive Review on the Pyrolysis of Lignocellulosic Biomass. *Renew. Energy* **2018**, *129*, 695–716. <https://doi.org/10.1016/j.renene.2017.04.035>.
- (31) Li, L.; Rowbotham, J. S.; Christopher Greenwell, H.; Dyer, P. W. Chapter 8 - An Introduction to Pyrolysis and Catalytic Pyrolysis: Versatile Techniques for Biomass Conversion. In *New and Future Developments in Catalysis*; Suib, S. L., Ed.; Elsevier: Amsterdam, 2013; pp 173–208. <https://doi.org/10.1016/B978-0-444-53878-9.00009-6>.
- (32) Yuvaraj, D.; Bharathiraja, B.; Rithika, J.; Dhanasree, S.; Ezhilarasi, V.; Lavanya, A.; Praveenkumar, R. Production of Biofuels from Fish Wastes: An Overview. *Biofuels* **2019**, *10* (3), 301–307. <https://doi.org/10.1080/17597269.2016.1231951>.
- (33) Xu, Y.; Ye, J.; Zhou, D.; Su, L. Research Progress on Applications of Calcium Derived from Marine Organisms. *Sci. Rep.* **2020**, *10* (1), 18425. <https://doi.org/10.1038/s41598-020-75575-8>.
- (34) Balzano, M.; Pacetti, D.; Lucci, P.; Fiorini, D.; Frega, N. G. Bioactive Fatty Acids in Mantis Shrimp, Crab and Caramote Prawn: Their Content and Distribution among the Main Lipid Classes. *J. Food Compos. Anal.* **2017**, *59*, 88–94. <https://doi.org/10.1016/j.jfca.2017.01.013>.
- (35) Figueroa-Muñoz, G.; Ríos-Escalante, P. D. los; Dantagnan, P.; Toledo, C.; Oyarzún, R.; Vargas-Chacoff, L.; Esse, C.; Vega-Aguayo, R. Proximal Composition and Fatty Acid Profile of *Hemigrapsus Crenulatus* (H. Milne Edwards, 1837) as One of the Main Foods of “Patagonian Blenny” *Eleginops Maclovinus* (Cuvier, 1830). *Braz. J. Biol.* **2021**, *81* (3), 797–805. <https://doi.org/10.1590/1519-6984.231834>.
- (36) *What is Calcium Carbonate? - Industrial Minerals Association - North America.* https://www.ima-na.org/page/what_is_calcium_carb (accessed 2021-11-21).
- (37) Yao, H.; Zheng, G.; Li, W.; McDowell, M. T.; Seh, Z.; Liu, N.; Lu, Z.; Cui, Y. Crab Shells as Sustainable Templates from Nature for Nanostructured Battery Electrodes. *Nano Lett.* **2013**, *13* (7), 3385–3390. <https://doi.org/10.1021/nl401729r>.
- (38) Sebestyén, Z.; Jakab, E.; Domán, A.; Bokrossy, P.; Bertóti, I.; Madarász, J.; László, K. Thermal Degradation of Crab Shell Biomass, a Nitrogen-Containing Carbon Precursor. *J.*

- Therm. Anal. Calorim.* **2020**, *142* (1), 301–308. <https://doi.org/10.1007/s10973-020-09438-9>.
- (39) -Asunción Lage-Yusty, M.; Vilasoa-Martínez, M.; Álvarez-Pérez, S.; López-Hernández, J. Chemical Composition of Snow Crab Shells (*Chionoecetes Opilio*) Composición Química Del Caparazón Del Cangrejo de Las Nieves (*Chionoecetes Opilio*). *CyTA - J. Food* **2011**, *9* (4), 265–270. <https://doi.org/10.1080/19476337.2011.596285>.
- (40) Beaulieu, L.; Thibodeau, J.; Bryl, P.; Carbonneau, M.-É. Characterization of Enzymatic Hydrolyzed Snow Crab (*Chionoecetes Opilio*) by-Product Fractions: A Source of High-Valued Biomolecules. *Bioresour. Technol.* **2009**, *100* (13), 3332–3342. <https://doi.org/10.1016/j.biortech.2009.01.073>.
- (41) Hamdi, M.; Nasri, R.; Dridi, N.; Li, S.; Nasri, M. Development of Novel High-Selective Extraction Approach of Carotenoproteins from Blue Crab (*Portunus Segnis*) Shells, Contribution to the Qualitative Analysis of Bioactive Compounds by HR-ESI-MS. *Food Chem.* **2020**, *302*, 125334. <https://doi.org/10.1016/j.foodchem.2019.125334>.
- (42) Park, J.-H.; Wang, J. J.; Xiao, R.; Zhou, B.; Delaune, R. D.; Seo, D.-C. Effect of Pyrolysis Temperature on Phosphate Adsorption Characteristics and Mechanisms of Crawfish Char. *J. Colloid Interface Sci.* **2018**, *525*, 143–151. <https://doi.org/10.1016/j.jcis.2018.04.078>.
- (43) Kazan State Power Engineering University; Kalayda, M. L.; Khamitova, M. F.; Kazan State Power Engineering University; Bogatyrev, I. A.; Kazan State Power Engineering University. Features of the Chemical Composition of Crayfish. *Butlerov Commun.* **2019**, *57* (1), 72–79. <https://doi.org/10.37952/ROI-jbc-01/19-57-1-72>.
- (44) Kazemi, R.; Ronaghi, A.; Yasrebi, J.; Ghasemi-Fasaei, R.; Zarei, M. Effect of Shrimp Waste-Derived Biochar and Arbuscular Mycorrhizal Fungus on Yield, Antioxidant Enzymes, and Chemical Composition of Corn Under Salinity Stress. *J. Soil Sci. Plant Nutr.* **2019**, *19* (4), 758–770. <https://doi.org/10.1007/s42729-019-00075-2>.
- (45) Shrimp Facts and Information | Characteristics, Diet, Survival. *Whale Facts*, 2021.
- (46) Kannan, S.; Garipey, Y.; Raghavan, G. S. V. Optimization and Characterization of Hydrochar Derived from Shrimp Waste. *Energy Fuels* **2017**, *31* (4), 4068–4077. <https://doi.org/10.1021/acs.energyfuels.7b00093>.
- (47) Huang, S.; Ding, Y.; Li, Y.; Han, X.; Xing, B.; Wang, S. *Energy Fuels* **2021**, *35* (2), 1557–1566. <https://doi.org/10.1021/acs.energyfuels.0c04042>.

- (48) Shahidi, F.; Synowiecki, J. Isolation and Characterization of Nutrients and Value-Added Products from Snow Crab (*Chionoecetes Opilio*) and Shrimp (*Pandalus Borealis*) Processing Discards. *J. Agric. Food Chem.* **1991**, *39* (8), 1527–1532. <https://doi.org/10.1021/jf00008a032>.
- (49) Naczka, M.; Williams, J. P.; Brennan, K.; Liyanapathirana, C.; Shahidi, F. Compositional Characteristics of Green Crab (*Carcinus Maenas*). **2004**. <https://doi.org/10.1016/J.FOODCHEM.2004.01.056>.
- (50) Hopkins, D. T.; MacQuarrie, S.; Hawboldt, K. A. Removal of Copper from Sulfate Solutions Using Biochar Derived from Crab Processing By-Product. *J. Environ. Manage.* **2022**, *303*, 114270. <https://doi.org/10.1016/j.jenvman.2021.114270>.
- (51) Zhang, P.; Hu, H.; Tang, H.; Yang, Y.; Liu, H.; Lu, Q.; Li, X.; Worasuwannarak, N.; Yao, H. In-Depth Experimental Study of Pyrolysis Characteristics of Raw and Cooking Treated Shrimp Shell Samples. *Renew. Energy* **2019**, *139*, 730–738. <https://doi.org/10.1016/j.renene.2019.02.119>.
- (52) Kannan, S.; Garipey, Y.; Raghavan, G. S. V. Conventional Hydrothermal Carbonization of Shrimp Waste. *Energy Fuels* **2018**, *32* (3), 3532–3542. <https://doi.org/10.1021/acs.energyfuels.7b03997>.
- (53) Xiao, Y.; Xue, Y.; Gao, F.; Mosa, A. Sorption of Heavy Metal Ions onto Crayfish Shell Biochar: Effect of Pyrolysis Temperature, PH and Ionic Strength. *J. Taiwan Inst. Chem. Eng.* **2017**, *80*, 114–121. <https://doi.org/10.1016/j.jtice.2017.08.035>.
- (54) Kazemi, R.; Ronaghi, A.; Yasrebi, J.; Ghasemi-Fasaei, R.; Zarei, M. Effect of Shrimp Waste-Derived Biochar and Arbuscular Mycorrhizal Fungus on Yield, Antioxidant Enzymes, and Chemical Composition of Corn Under Salinity Stress. *J. Soil Sci. Plant Nutr.* **2019**, *19* (4), 758–770. <https://doi.org/10.1007/s42729-019-00075-2>.
- (55) Han, X.; Wu, Z.; Yang, Y.; Guo, J.; Wang, Y.; Cai, L.; Song, W.; Ji, L. Facile Preparation of a Porous Biochar Derived from Waste Crab Shell with High Removal Performance for Diesel. *J. Renew. Mater.* **2021**, *9* (8), 1377–1391. <https://doi.org/10.32604/jrm.2021.015076>.
- (56) Chen, Y.; Zhang, H.; Guo, J.; Cai, L.; Wang, Y.; Yao, X.; Song, W.; Ji, L. Highly Efficient Adsorption of P-Xylene from Aqueous Solutions by Hierarchical Nanoporous Biochar Derived from Crab Shell. *J. Renew. Mater.* **2021**, *9* (10), 1741–1755. <http://dx.doi.org.qe2a-proxy.mun.ca/10.32604/jrm.2021.015924>.

- (57) Cai, L.; Zhang, Y.; Zhou, Y.; Zhang, X.; Ji, L.; Song, W.; Zhang, H.; Liu, J. Effective Adsorption of Diesel Oil by Crab-Shell-Derived Biochar Nanomaterials. *Materials* **2019**, *12* (2), 236. <https://doi.org/10.3390/ma12020236>.
- (58) Magnacca, G.; Guerretta, F.; Vizintin, A.; Benzi, P.; Valsania, M. C.; Nisticò, R. Preparation, Characterization and Environmental/Electrochemical Energy Storage Testing of Low-Cost Biochar from Natural Chitin Obtained via Pyrolysis at Mild Conditions. *Appl. Surf. Sci.* **2018**, *427*, 883–893. <https://doi.org/10.1016/j.apsusc.2017.07.277>.
- (59) Zhang, X.; Wang, Y.; Ju, N.; Ai, Y.; Liu, Y.; Liang, J.; Hu, Z.-N.; Guo, R.; Xu, W.; Zhang, W.; Qi, Y.; Niu, D.; Liang, Q.; Sun, H.; Yang, Y. Ultimate Resourcization of Waste: Crab Shell-Derived Biochar for Antimony Removal and Sequential Utilization as an Anode for a Li-Ion Battery. *ACS Sustain. Chem. Eng.* **2021**, *9* (26), 8813–8823. <https://doi.org/10.1021/acssuschemeng.1c01851>.
- (60) Long, L.; Xue, Y.; Zeng, Y.; Yang, K.; Lin, C. Synthesis, Characterization and Mechanism Analysis of Modified Crayfish Shell Biochar Possessed ZnO Nanoparticles to Remove Trichloroacetic Acid. *J. Clean. Prod.* **2017**, *166*, 1244–1252. <https://doi.org/10.1016/j.jclepro.2017.08.122>.
- (61) Yan, J.; Xue, Y.; Long, L.; Zeng, Y.; Hu, X. Adsorptive Removal of As(V) by Crawfish Shell Biochar: Batch and Column Tests. *Environ. Sci. Pollut. Res.* **2018**, *25*. <https://doi.org/10.1007/s11356-018-3384-1>.
- (62) Zhang, D.; He, Q.; Hu, X.; Zhang, K.; Chen, C.; Xue, Y. Enhanced Adsorption for the Removal of Tetracycline Hydrochloride (TC) Using Ball-Milled Biochar Derived from Crayfish Shell. *Colloids Surf. Physicochem. Eng. Asp.* **2021**, *615*, 126254. <https://doi.org/10.1016/j.colsurfa.2021.126254>.
- (63) Zhang, J.; Hu, X.; Zhang, K.; Xue, Y. Desorption of Calcium-Rich Crayfish Shell Biochar for the Removal of Lead from Aqueous Solutions. *J. Colloid Interface Sci.* **2019**, *554*, 417–423. <https://doi.org/10.1016/j.jcis.2019.06.096>.
- (64) Yin, W.; Zhang, W.; Zhao, C.; Xu, J. Evaluation of Removal Efficiency of Ni(II) and 2,4-DCP Using in Situ Nitrogen-Doped Biochar Modified with Aquatic Animal Waste. *ACS Omega* **2019**, *4* (21), 19366–19374. <https://doi.org/10.1021/acsomega.9b02769>.
- (65) Moreno, J. C.; Gómez, R.; Giraldo, L. Removal of Mn, Fe, Ni and Cu Ions from Wastewater Using Cow Bone Charcoal. *Materials* **2010**, *3* (1), 452–466. <https://doi.org/10.3390/ma3010452>.

- (66) Rusova, N. V.; Astashkina, O. V.; Lysenko, A. A.; Morozova, M. A. Oscillating Character of Adsorption of Iron(III) Ion by Carbon Sorbents. *Fibre Chem.* **2018**, *50* (2), 100–103. <https://doi.org/10.1007/s10692-018-9940-0>.
- (67) Runtti, H.; Tuomikoski, S.; Kangas, T.; Lassi, U.; Kuokkanen, T.; Rämö, J. Chemically Activated Carbon Residue from Biomass Gasification as a Sorbent for Iron(II), Copper(II) and Nickel(II) Ions. *J. Water Process Eng.* **2014**, *4*, 12–24. <https://doi.org/10.1016/j.jwpe.2014.08.009>.
- (68) Ni, B.-J.; Huang, Q.-S.; Wang, C.; Ni, T.-Y.; Sun, J.; Wei, W. Competitive Adsorption of Heavy Metals in Aqueous Solution onto Biochar Derived from Anaerobically Digested Sludge. *Chemosphere* **2019**, *219*, 351–357. <https://doi.org/10.1016/j.chemosphere.2018.12.053>.
- (69) Akcil, A.; Koldas, S. Acid Mine Drainage (AMD): Causes, Treatment and Case Studies. *J. Clean. Prod.* **2006**, *14* (12–13), 1139–1145. <https://doi.org/10.1016/j.jclepro.2004.09.006>.
- (70) Wang, Y.; Wang, H.-S.; Tang, C.-S.; Gu, K.; Shi, B. Remediation of Heavy-Metal-Contaminated Soils by Biochar: A Review. *Environ. Geotech.* **2020**, 1–14. <https://doi.org/10.1680/jenge.18.00091>.
- (71) Hove, M.; van Hille, R. P.; Lewis, A. E. Iron solids formed from oxidation precipitation of ferrous sulfate solutions. *AIChE J.* **2007**, *53* (10), 2569–2577. <https://doi.org/10.1002/aic.11264>.
- (72) Vuceta, J.; Morgan, J. J. Hydrolysis of Cu(II)1. *Limnol. Oceanogr.* **1977**, *22* (4), 742–746. <https://doi.org/10.4319/lo.1977.22.4.0742>.
- (73) Guimarães, L.; de Abreu, H. A.; Duarte, H. A. Fe(II) Hydrolysis in Aqueous Solution: A DFT Study. *Chem. Phys.* **2007**, *333* (1), 10–17. <https://doi.org/10.1016/j.chemphys.2006.12.023>.
- (74) *Ksp Table*. <https://www.chm.uri.edu/weuler/chm112/refmater/KspTable.html> (accessed 2022-05-30).
- (75) Largitte, L.; Pasquier, R. A Review of the Kinetics Adsorption Models and Their Application to the Adsorption of Lead by an Activated Carbon. *Chem. Eng. Res. Des.* **2016**, *109*, 495–504. <https://doi.org/10.1016/j.cherd.2016.02.006>.

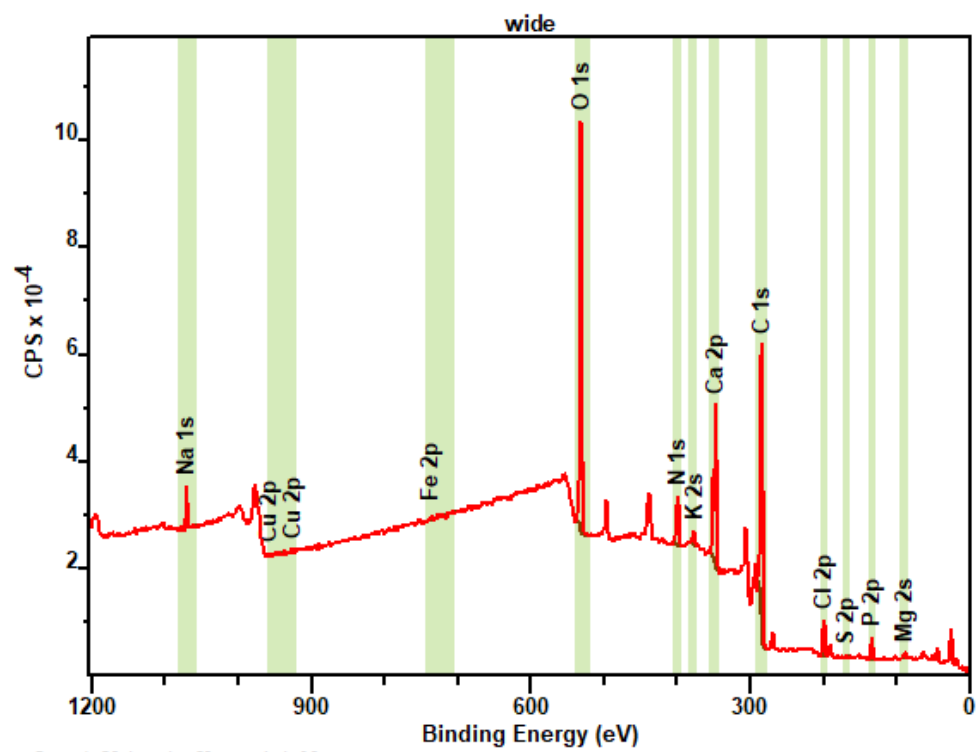
- (76) Qiao, Y.; Chen, S.; Liu, Y.; Sun, H.; Jia, S.; Shi, J.; Pedersen, C. M.; Wang, Y.; Hou, X. Pyrolysis of Chitin Biomass: TG–MS Analysis and Solid Char Residue Characterization. *Carbohydr. Polym.* **2015**, *133*, 163–170. <https://doi.org/10.1016/j.carbpol.2015.07.005>.
- (77) Nekvapil, F.; Aluas, M.; Barbu-Tudoran, L.; Suci, M.; Bortnic, R.-A.; Glamuzina, B.; Pinzaru, S. C. From Blue Bioeconomy toward Circular Economy through High-Sensitivity Analytical Research on Waste Blue Crab Shells. *ACS Sustain. Chem. Eng.* **2019**, *7* (19), 16820–16827. <https://doi.org/10.1021/acssuschemeng.9b04362>.
- (78) Brewer, C. E.; Schmidt-Rohr, K.; Satrio, J. A.; Brown, R. C. Characterization of Biochar from Fast Pyrolysis and Gasification Systems. *Environ. Prog. Sustain. Energy* **2009**, *28* (3), 386–396. <https://doi.org/10.1002/ep.10378>.
- (79) Al-Hosney, H. A.; Grassian, V. H. Water, Sulphur Dioxide and Nitric Acid Adsorption on Calcium Carbonate: A Transmission and ATR-FTIR Study. *Phys. Chem. Chem. Phys.* **2005**, *7* (6), 1266–1276. <https://doi.org/10.1039/B417872F>.
- (80) Suwannasingha, N.; Kantavong, A.; Tunkijjanukij, S.; Aenglong, C.; Liu, H.-B.; Klaypradit, W. Effect of Calcination Temperature on Structure and Characteristics of Calcium Oxide Powder Derived from Marine Shell Waste. *J. Saudi Chem. Soc.* **2022**, *26* (2), 101441. <https://doi.org/10.1016/j.jscs.2022.101441>.
- (81) Karunadasa, K. S. P.; Manoratne, C. H.; Pitawala, H. M. T. G. A.; Rajapakse, R. M. G. Thermal Decomposition of Calcium Carbonate (Calcite Polymorph) as Examined by in-Situ High-Temperature X-Ray Powder Diffraction. *J. Phys. Chem. Solids* **2019**, *134*, 21–28. <https://doi.org/10.1016/j.jpcs.2019.05.023>.
- (82) Cahill, L. S.; Yao, Z.; Adronov, A.; Penner, J.; Moonosawmy, K. R.; Kruse, P.; Goward, G. R. Polymer-Functionalized Carbon Nanotubes Investigated by Solid-State Nuclear Magnetic Resonance and Scanning Tunneling Microscopy. *J. Phys. Chem. B* **2004**, *108* (31), 11412–11418. <https://doi.org/10.1021/jp0491865>.
- (83) Novotny, E. H.; Auccaise, R.; Velloso, M. H. R.; Corrêa, J. C.; Higarashi, M. M.; Abreu, V. M. N.; Rocha, J. D.; Kwapinski, W. Characterization of Phosphate Structures in Biochar from Swine Bones. *Pesqui. Agropecuária Bras.* **2012**, *47* (5), 672–676. <https://doi.org/10.1590/S0100-204X2012000500006>.
- (84) Radha, A. V.; Forbes, T. Z.; Killian, C. E.; Gilbert, P. U. P. A.; Navrotsky, A. Transformation and Crystallization Energetics of Synthetic and Biogenic Amorphous Calcium Carbonate. *Proc. Natl. Acad. Sci.* **2010**, *107* (38), 16438–16443. <https://doi.org/10.1073/pnas.1009959107>.

- (85) McCafferty, E. Thermodynamics of Corrosion: Pourbaix Diagrams. In *Introduction to Corrosion Science*; McCafferty, E., Ed.; Springer: New York, NY, 2010; pp 95–117. https://doi.org/10.1007/978-1-4419-0455-3_6.
- (86) Szivós, K.; Juhai, É.; Kántor, T.; Pungor, E. Determination of Iron and Calcium Impurities in Magnesium Oxide by Atomic Absorption. *Microchim. Acta* **1981**, 75 (3), 259–264. <https://doi.org/10.1007/BF01196395>.
- (87) Tabak, H. H.; Scharp, R.; Burckle, J.; Kawahara, F. K.; Govind, R. Advances in Biotreatment of Acid Mine Drainage and Biorecovery of Metals: 1. Metal Precipitation for Recovery and Recycle. *Biodegradation* **2003**, 14 (6), 423–436. <https://doi.org/10.1023/A:1027332902740>.
- (88) Leiva, C. A.; Gálvez, M. E.; Fuentes, G. E.; Acuña, C. A.; Alcota, J. A. Effects of Various Precipitants on Iron Removal from a Zinc Concentrate Pressure Leaching Solution. *Minerals* **2022**, 12 (1), 84. <https://doi.org/10.3390/min12010084>.
- (89) Revellame, E. D.; Fortela, D. L.; Sharp, W.; Hernandez, R.; Zappi, M. E. Adsorption Kinetic Modeling Using Pseudo-First Order and Pseudo-Second Order Rate Laws: A Review. *Clean. Eng. Technol.* **2020**, 1, 100032. <https://doi.org/10.1016/j.clet.2020.100032>.
- (90) *Solubility Rules*. Chemistry LibreTexts. [https://chem.libretexts.org/Bookshelves/Physical_and_Theoretical_Chemistry_Textbook_Maps/Supplemental_Modules_\(Physical_and_Theoretical_Chemistry\)/Equilibria/Solubility/Solubility_Rules](https://chem.libretexts.org/Bookshelves/Physical_and_Theoretical_Chemistry_Textbook_Maps/Supplemental_Modules_(Physical_and_Theoretical_Chemistry)/Equilibria/Solubility/Solubility_Rules) (accessed 2022-05-29).
- (91) Yang, J.; Zhao, Y.; Ma, S.; Zhu, B.; Zhang, J.; Zheng, C. Mercury Removal by Magnetic Biochar Derived from Simultaneous Activation and Magnetization of Sawdust. *Environ. Sci. Technol.* **2016**, 50 (21), 12040–12047. <https://doi.org/10.1021/acs.est.6b03743>.

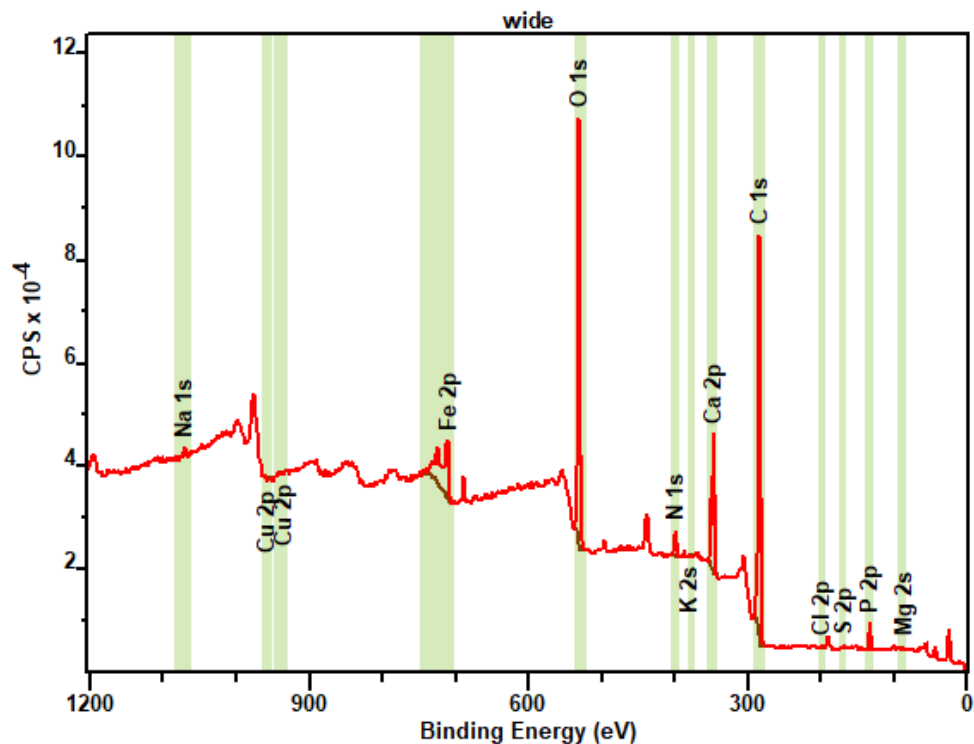
Appendix

X-ray Photoelectron Spectroscopy (XPS) Data

As-prepared crab char:

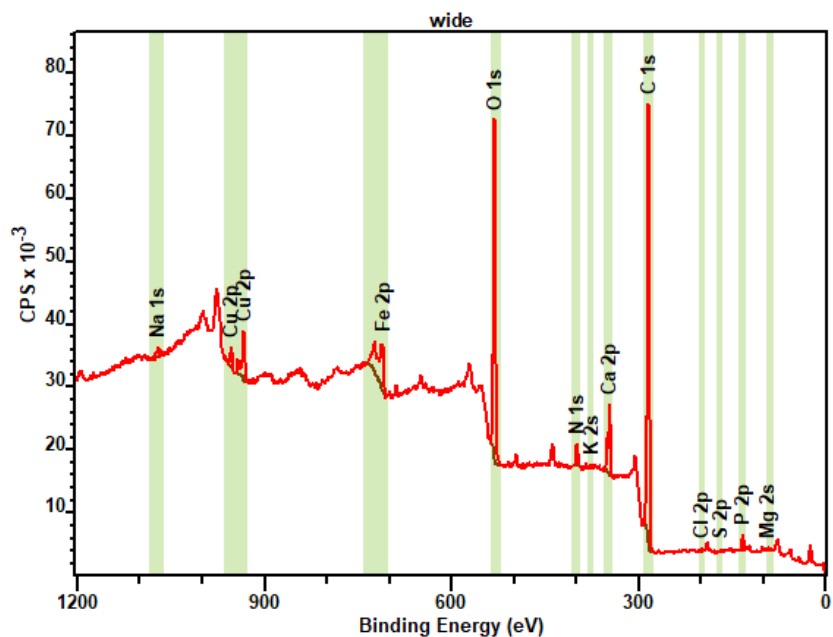


Fe-absorbed on crab char:



Queen's University Kratos Axis Nova

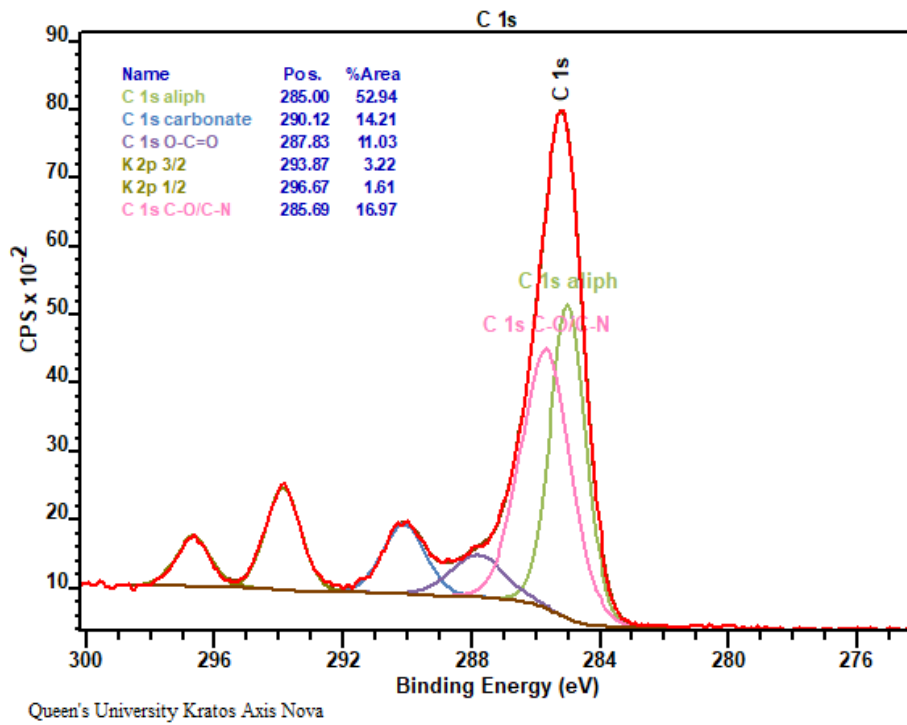
Cu and Fe-absorbed on crab char:



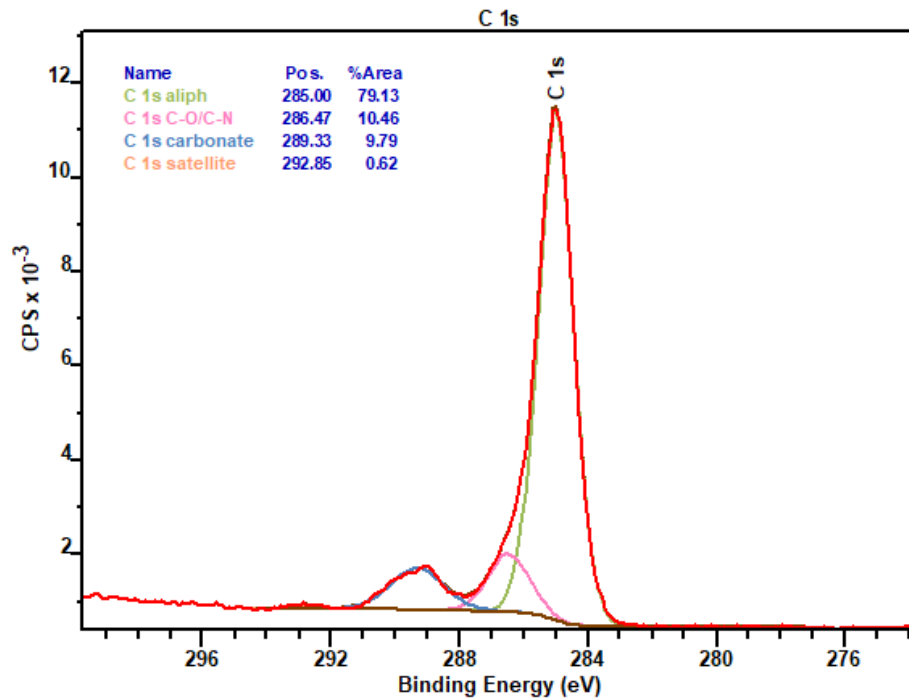
Queen's University Kratos Axis Nova

High Resolution Scans: Carbon 1s:

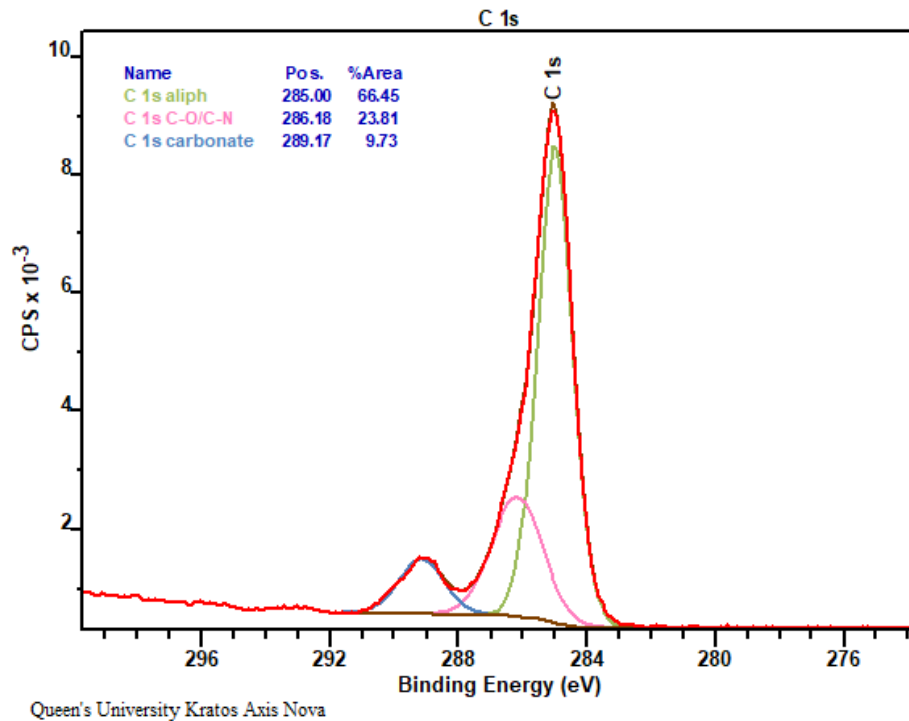
As-prepared crab char:



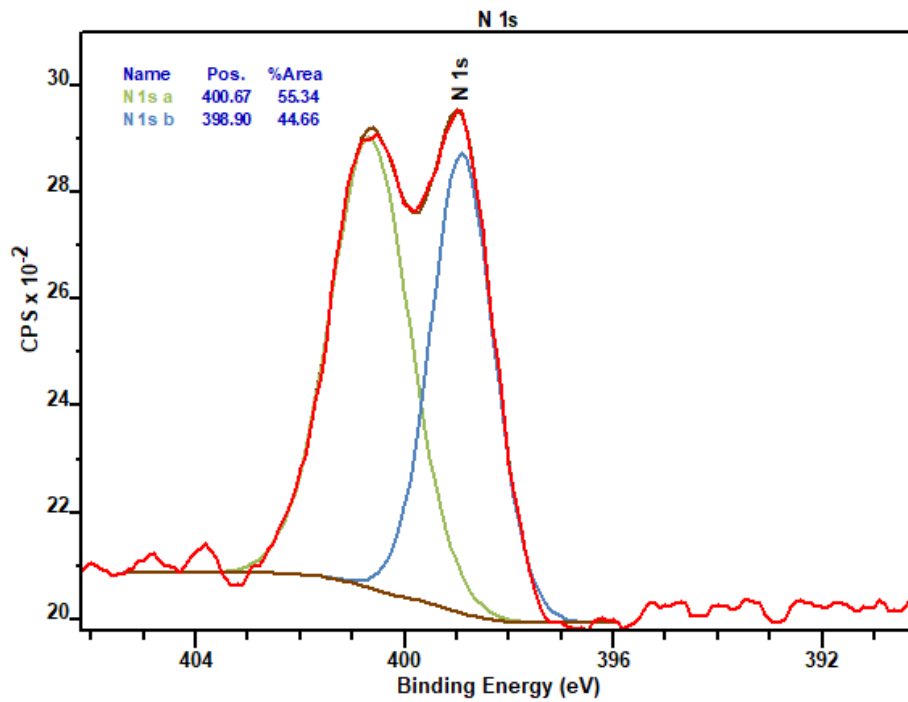
Fe-absorbed crab char:



Cu and Fe-absorbed crab char:

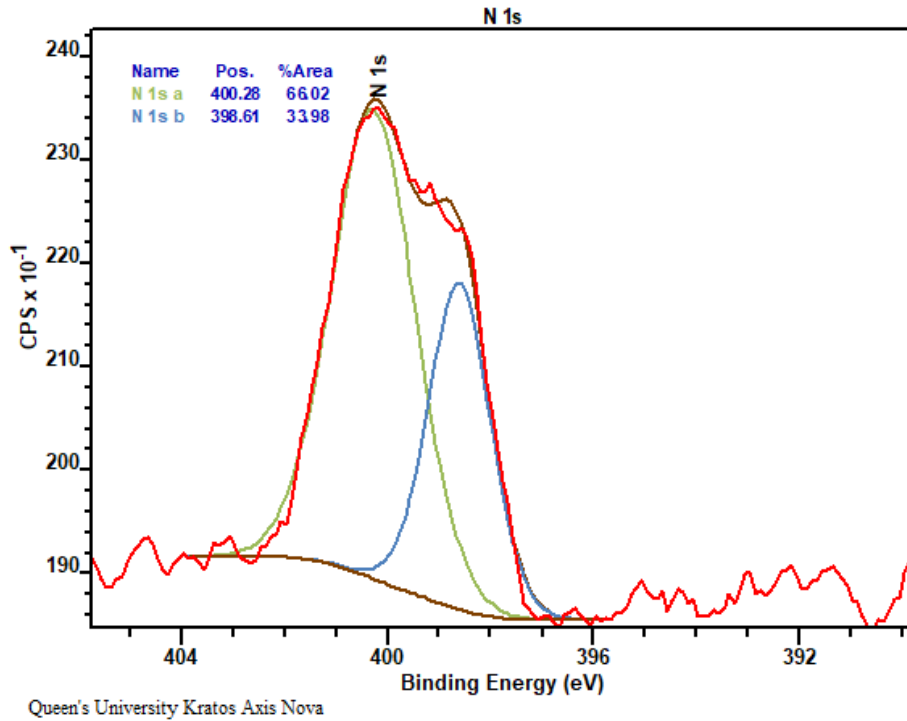


Nitrogen 1s:



As-prepared crab char: Queen's University Kratos Axis Nova

Fe-absorbed crab char:



Cu and Fe-absorbed crab char:

